Important Notice

UNIVERSITY OF CALGARY

Hydrocarbon indicators derived from AVO analysis

by

Hong Feng

A THESIS

SUBMITTED TO THE FACULTY OF GRADUATE STUDIES

IN PARTIAL FULFILMENT OF THE REQUIREMENTS FOR THE

DEGREE OF MASTER OF SCIENCE

DEPARTMENT OF GEOSCIENCE

CALGARY, ALBERTA

JULY, 2009

UNIVERSITY OF CALGARY

FACULTY OF GRADUATE STUDIES

The undersigned certify that they have read, and recommend to the Faculty of Graduate Studies for acceptance, a thesis entitled " Hydrocarbon indicators derived from AVO analysis " submitted by Hong Feng in partial fulfilment of the requirements of the degree of Master of Science.

Supervisor, Dr. John C. Bancroft
Department of Geoscience

Co-Supervisor, Dr. Brian H. Russell
Department of Geoscience

Dr. Larry R. Lines
Department of Geoscience

External Examiner, Dr. Rod Blais
Department of Geomatics Engineering

September 21, 2009

Abstract

Numerous approaches have been published which derive fluid indicators, often called direct hydrocarbon indicators (DHI), from AVO (amplitude versus offset) equations. The main idea behind these methods is to use linearized approximations to the Zoeppritz equations to extract petrophysical parameters, such as P-wave and S-wave impedance and velocity, elastic modulii, and then infer the fluid content from cross-plots of these parameters. Russell et al. (2003) used standard poroelasticity theory (Biot, 1941, and Gassmann, 1951) to generalize several of these methods using a scaling factor: $(V_p / V_s)^2_{dry}$, which is dependent on the properties of the dry rock. The purpose of this study is to study the generalized fluid method proposed by Russell et al. (2003) to find the optimal value for $(V_p / V_s)^2_{dry}$ used in this method.

The effect of clay content, porosity, and pressure on the P-wave and S-wave velocities and $(V_p / V_s)_{dry}$ ratio for sandstones will be investigated in this study. Also, previous fluid methods will be summarized and compared with the generalized fluid method to study which indicator can most easily discriminate a gas or oil sand from the background and which indicator is most sensitive to the pore-fluid content.

Acknowledgements

I would like to extend my sincere thanks and gratitude to my supervisors, Dr. John Bancroft and Dr. Brian H. Russell, for their invaluable caring mentoring and guidance throughout the course of this research. I would also like to thank the CREWES project sponsor companies for providing financial support for this research. For their efforts and assistance, a special thanks as well to the CREWES project directors, staffs, and students for their suggestions, assistance, and helpful insight into this research.

Dedication

Dedicated to my lovely wife, Mingming Ni

Table of Contents

APPROVAL PAGE..... ii
ABSTRACT..... iii
ACKNOWLEDGEMENTS.....iv
DEDICATION.....v
TABLE OF CONTENTS.....vi
LIST OF TABLES.....viii
LIST OF FIGURES.....ix
LIST OF SYMBOL DEFINITIONS.....xiv

CHAPTER 1. INTRODUCTION 1……..…1
1.1 Thesis objective ……1
1.2 Data used ……..4
1.3 Hardware and software used…….…….5
1.4 Thesis organization……..…….……..……..5
1.5 The contribution of this thesis…….……..…..6

CHAPTER 2. AVO THEORY AND FLUID EXTRACTION METHODS……8
2.1 Introduction……8
2.2 The linearized AVO equation……...…….8
2.2.1 The Zoeppritz's equation……..……9
2.2.2 Bortfeld approximation ……..……..…….10
2.2.3 Aki-Richards-Frasier approximation ……...……...……11
2.2.4 Shuey's approximation……..……12
2.2.5 Hilterman's approximation……....……...…13
2.2.6 Smith and Gidlow approximation…….……..14
2.2.7 Fatti et al.'s approximation……..……..14
2.2.8 Gray's approximation……..…….……..15
2.2.9 The general linearized equation……..…..…….16
2.3 Early fluid extraction methods……19
2.3.1 Interception and gradient……..…….19
2.3.2 The fluid factor……..……21
2.3.3 Elastic impedance……...……..22
2.3.4 LMR method……...……..24
2.3.5 Pore space modulus (*Kp*)……..……25

CHAPTER 3. BIOT-GASSMANN THEORY FOR POROUS ROCK…….….28
3.1 Introduction ……28
3.2 Biot-Gassmann theory…...……...…….28
3.2.1 Biot-Gassmann equation..……29
3.2.2 Some assumptions for Biot-Gassmann theory .....…...…….31
3.3 Generalized fluid method for impedances…...……32
3.4 Generalized fluid method for linearized AVO ……38

CHAPTER 4. EMPIRICAL STUDY USING HAN'S DATASET……41
4.1 Introduction……41
4.2 Sample description……42
4.3 Clean sandstones……43
4.4 Shaly sandstones……46
4.5 The effects of pressure on V_p, V_s and V_p/V_s ratio……50
4.6 Summary……54

CHAPTER 5. SENSITIVITY ANALYSIS FOR FLUID INDICATORS……58
5.1 Introduction……58
5.2 Analysis using class I, II, and III sand models……59
5.3 Analysis using Han's dataset……61
5.4 Crossplot analysis for the fluid indicators……64
5.5 Using different C values……69
5.6 Conclusion……72

CHAPTER 6. BLACKFOOT CASE STUDY……73
6.1 Introduction……73
6.2 Seismic and well data……73
6.3 Geological background……75
6.4 True amplitude processing of Blackfoot PP data……78
6.5 Pre-stack seismic inversion……79
6.6 The Generalized fluid terms extraction……85
6.6.1 C value extraction……85
6.6.2 Fluid term extraction……87
6.7 Conclusions……95

CHAPTER 7. CONCLUSION AND FUTURE WORK……96
7.1 Conclusion……96
7.2 Future work……97

REFERENCES……98

List of Tables

Table 2.1 R_i terms for the general linearized equation.

Table 2.2 Terms a, b, and c for the general linearized equation.

Table 4.1 Pressure dependence on V_p, V_s, and V_p/V_s ratio for shaly sandstones.

Table 4.2 Pressure dependence on V_p, V_s, and V_p/V_s ratio for clean sandstones.

Table 4.3 Effects of clay content (shale), porosity, and pressure on V_p, V_s, and V_p/V_s ratio.

Table 5.1 Mean and standard deviation values and fluid indicator coefficients for fluid indicators at 5 MPa.

Table 5.2 Mean and standard deviation values and fluid indicator coefficients for fluid indicators at 50 MPa.

List of Figures and Illustrations

Figure 2.1 The partition of energy among reflected and transmitted P-wave and S-wave at a layer boundary.

Figure 2.2 AVO intercept (A) versus gradient (B) crossplot showing four possible quadrants.

Figure 2.3 Crossplot of P-wave velocity versus S-wave velocity.

Figure 2.4 The acoustic impedance (AI) and Elastic Impedance (EI) curves at 30 degrees.

Figure 2.5 Crossplot of P-impedance versus S-impedance (left) and lambda-rho versus Mu-rho (right).

Figure 3.1 The schematic diagram for the porous saturated rock.

Figure 3.2 Plot of $I_p^2 - c * I_s^2$ versus I_p (P-wave impedance) using different c values.

Figure 4.1 The ranges of clay content and porosity for 75 shaly sandstones of this study. Porosity ranges from 2 to 30 percent, and clay content ranges from 0 to about 50 percent.

Figure 4.2 Measured P-wave velocity versus porosity for 10 clean sandstones at Pe = 5 MPa.

Figure 4.3 Measured S-wave velocity versus porosity for 10 clean sandstones at Pe = 5 MPa.

Figure 4.4 Plot of V_p / V_s ratio versus porosity for 10 clean sandstones at Pe = 5 MPa.

Figure 4.5 Measured P-wave velocity versus porosity color-coded with clay content for shaly sandstones at Pe = 5 MPa.

Figure 4.6 Measured S-wave velocity versus porosity color-coded with clay content for shaly sandstones at Pe = 5 MPa.

Figure 4.7 Plot of V_p / V_s versus porosity color-coded with clay content for shaly sandstones at Pe = 5 MPa.

Figure 4.8 Plot of V_p and V_s versus pressure for shaly sandstone samples using an empirical relation when porosity =0.2 and clay content =0.2.

Figure 4.9 Plot of V_p / V_s versus pressure for shaly sandstones using an empirical relation when porosity =0.2 and clay content =0.2.

Figure 4.10 Plot of V_p and V_s versus pressure for clean sandstones using an empirical relation when porosity =0.2.

Figure 4.11 Plot of V_p / V_s ratio versus pressure for clean sandstones using an empirical relation when porosity =0.2.

Figure 4.12 Correlation between V_p / V_s ratio and porosity for the whole dataset at Pe = 5 MPa and 50MPa (Han et al., 1986).

Figure 4.13 Correlation between V_p / V_s ratio and clay content for the whole dataset at Pe = 5 MPa and 50MPa (Han et al., 1986).

Figure 4.14 V_p / V_s ratio histograms for 5 MPa, 10 MPa, 20 MPa, 30 MPa, 40 MPa, and 50 MPa pressure. Note that V_p / V_s ratio increases with differential pressure (Han et al., 1986).

Figure 5.1 Calculated fluid indicators for Class III sand model (4000 ft depth). 1. V_p, 2. V_s, 3. (V_p / V_s), 4. ρ, 5. Ip, 6. Is, 7. $\mu\rho$, 8. $\lambda\rho$, 9. K, 10. μ, 11. λ, 12. λ / μ, 13. Poisson's ratio (σ), 14. $K - \mu$, 15. $Ip^2 - c * Is^2$, 16. Fluid factor (ΔF).

Figure 5.2 Calculated fluid indicators for Class II sand model (9000-ft depth). 1. V_p, 2. V_s, 3. (V_p / V_s), 4. ρ, 5. Ip, 6. Is, 7. $\mu\rho$, 8. $\lambda\rho$, 9. K, 10. μ, 11. λ, 12. λ / μ, 13. Poisson's ratio (σ), 14. $K - \mu$, 15. $Ip^2 - c * Is^2$, 16. Fluid factor (ΔF).

Figure 5.3 Calculated fluid indicators for Class I sand model (14000-ft depth). 1. V_p, 2. V_s, 3. (V_p / V_s), 4. ρ, 5. Ip, 6. Is, 7. $\mu\rho$, 8. $\lambda\rho$, 9. K, 10. μ, 11. λ, 12. λ / μ, 13. Poisson's ratio (σ), 14. $K - \mu$, 15. $Ip^2 - c * Is^2$, 16. Fluid factor (ΔF).

Figure 5.4 Fluid indicators coefficient versus pressure. Observe that the indicator: $Ip^2 - c * Is^2$ is the most effective indicator.

Figure 5.5 Crossplot of fluid term ($\rho f = Ip^2 - 2.2333 * Is^2$) versus P-wave impedance (Ip) color-coded with clay content for dry and wet sandstone samples at Pe=5 MPa.

Figure 5.6 Crossplot of fluid term ($K - \mu$) versus P-wave impedance (Ip) color-coded with clay content for dry and wet sandstone samples at Pe=5 MPa.

Figure 5.7 Crossplot of fluid term ($\lambda\rho$) versus P-wave impedance (Ip) color-coded with clay content for dry and wet sandstone samples at Pe=5 MPa.

Figure 5.8 Crossplot of fluid term ($\rho f = Ip^2 - 2.2333 * Is^2$) versus P-wave impedance (Ip) color-coded with porosity for dry and wet sandstone samples at Pe=5 MPa.

Figure 5.9 Crossplot of fluid term ($\rho f = Ip^2 - 2.2333 * Is^2$) versus P-wave impedance (Ip) color-coded with porosity for dry and wet sandstone samples at Pe=50MPa.

Figure 5.10 Crossplot of fluid term (ρf , $c = 2.8$) versus P-wave impedance (Ip) color-coded with clay content for dry and wet sandstone samples at Pe=5 MPa.

Figure 5.11 Crossplot of fluid term (ρf , $c = 2.333$) versus P-wave impedance (Ip) color-coded with clay content for dry and wet sandstone samples at Pe=5 MPa.

Figure 5.12 Crossplot of fluid term (ρf , $c = 2.233$) versus P-wave impedance (Ip) color-coded with clay content for dry and wet sandstone samples at Pe=5 MPa.

Figure 5.13 Crossplot of fluid term (ρf , $c = 2$) versus P-wave impedance (Ip) color-coded with clay content for dry and wet sandstone samples at Pe=5 MPa.

Figure 6.1 Paleogeography of Lower Cretaceous during the formation of the Glauconitic incised-valley system and location of Blackfoot area.

Figure 6.2 Schematic stratigraphy of the Glauconitic incised valley system.

Figure 6.3 The time structure for the Ostracod horizon (upper valley) and well locations.

Figure 6.4 Seismic section across the well 08-08 with Ostracod and Mississippian horizons and resistivity well log.

Figure 6.5 Time slices from P-wave stack which show the upper valley (left) and lower valley (right). The low amplitude maps the porous sandstone in the Glauconitic channel system.

Figure 6.6 The waveform and the spectrum for the extracted wavelet for the near offset at the location of well 08-08.

Figure 6.7 Well calibrations for well 08-08. Well logs were blocking processed. Synthetic is displayed in blue and extracted seismic trace is displayed in red.

Figure 6.8 Inverted P-wave and S-wave impedance, velocity and density logs (in red) and the original ones (in blue) using pre-stack seismic inversion for well 08-08.

Figure 6.9 In-line 85 cross section of the inverted P-wave impedance (Ip) with well tops and resistivity well log superimposed.

Figure 6.10 In-line 85 cross section of the inverted S-wave impedance (Is) with well tops and resistivity well log superimposed.

Figure 6.11 Time slices of P-wave impedance (left) and S-wave impedance (right) at upper valley level with well locations.

Figure 6.12 The estimated c value and gamma, density and lithology well logs for 08-08 well.

Figure 6.13 Crossplot of c value versus porosity for well 08-08, depth interval:1500 m-1750 m.

Figure 6.14 Comparison between P-wave velocity (V_p), Lambda*Rho ($\lambda\rho$), Poisson's ratio (σ), $K-\mu$, V_p/V_s and $Ip^2 - c*Is^2$ for well 08-08.

Figure 6.15 Crossplot of fluid term Rho*f (ρf) versus skeleton term Rho*s (ρs) for well 08-08.

Figure 6.16 Time slices of fluid term (ρf , c =2.333) for the upper valley (left) and lower valley (right) with well locations.

Figure 6.17 Time slices of skeleton term (ρs) for the upper valley (left) and lower valley (right) with well locations.

Figure 6.18 The crossplot (above) of the fluid term (ρf) versus the skeleton term (ρs) for the upper valley. Polygon in blue means the low fluid term. The blue color on the seismic cross section (bottom) is correspondent with the blue rectangle in the crossplot.

Figure 6.19 Time slices of fluid term (ρf , c =1.0) for the upper valley (left) and lower valley (right) with well locations.

Figure 6.20 Time slices of fluid term (ρf , c =2.0) for the upper valley (left) and lower valley (right) with well locations.

Figure 6.21 Time slices of fluid term (ρf , c =2.233) for the upper valley (left) and lower valley (right) with well locations.

Figure 6.22 Time slices of fluid term (ρf , c =3.0) for the upper valley (left) and lower valley (right) with well locations.

List of Symbols, Abbreviations and Nomenclature

Symbol	Definition
K_p	Bulk modulus of pore space
K_{sat}	Bulk modulus of saturated rock
K_{frame}	Bulk modulus of rock frame
K_{matrix}	Bulk modulus of mineral matrix
K_{fluid}	Bulk modulus of pore fluid
β	Biot coefficient
M	Gassmann's pore space modulus
ϕ	Porosity
λ	Incompressibility
ρ_{sat}	Density of saturated rock
μ	Shear modulus or rigidity of rock
μ_{sat}	Shear modulus of the saturated rock
μ_{dry}	Shear modulus of the dry rock
σ	Poisson's ratio
V_p	P-wave velocity
V_s	S-wave velocity
$R(\theta)$	P-wave reflection coefficient at any incident angle
R_p	Normal incident P wave reflection coefficient
I_p	P-wave impedance
I_s	S-wave impedance
AI	Acoustic impedance
EI	Elastic impedance
γ_{sat}	Vp/Vs for saturated rock
γ_{dry}	Vp/Vs for dry rock
A	Intercept
B	Gradient
G	Gradient
R_i	General reflectivity term
ΔF	Fluid factor
LMR	Lambda-mu-rho method
f	Fluid term
s	Dry rock frame term
c	Scaling factor for $I_p^2 - cI_s^2$ method
FIC	Fluid indicator coefficient

CHAPTER 1: INTRODUCTION

1.1 Thesis objective

The use of seismic shear waves has been known for decades as a promising method to extract rock information that infers the hydrocarbon content in a potential reservoir. However, its popularity has been limited by its higher recording cost and processing difficulties. In contrast, methods related to AVO (amplitude versus offset) using the conventional compressional seismic wave to extract shear wave information have become more popular because of its lower acquisition cost and a more straightforward analysis. This thesis focuses on the AVO method and introduces a refined processing method.

AVO methods were introduced to make up for the limitation of the horizontal stacking technique. Although horizontal stacking improves the signal–noise ratio of the seismic profile, it removes the valuable information embedded in the pre-stack gathers by computing the average amplitude for various offsets instead of the amplitude for the zero offset. Therefore, the horizontal stacking technique can't give the exact information for hydrocarbon and lithology discrimination.

At the early stage of AVO technology, bright spot, phase reversal, and dim out anomalies were largely used to recognize hydrocarbon anomalies on stacked seismic profiles. These three anomalies correspond to Rutherford and Williams's AVO classification: Class III (bright spot), Class II (phase reversal), and Class I (dim out).

Standard AVO methods used in the industry arise from the Zoeppritz equations. The Zoeppritz equations relate wave amplitudes of a reflected P-wave as a function of incident angle and rock properties. However, the formulation is quite complex and does not give us an intuitive understanding how these amplitudes relate to various rock

properties and incident angle. Over the years, to simplify the computations, a number of linearized approximations to Zoeppritz equations have been developed to give more insight into the parameters that control amplitude changes with offset or incident angle. Based on these approximations, numerous fluid terms are estimated to help to discriminate hydrocarbon anomalies from the non-reservoir background.

In the first phase of the AVO application, the emphasis was on studying the variations between the P-wave velocity or impedance and the S-wave velocity or impedance to identify hydrocarbon anomalies related to the pore fluid changes and lithology variation. The intercept-gradient method proposed by Shuey (1985) was used to extract P-wave and S-wave reflectivities. The fluid factor method proposed by Smith and Gidlow (1987) gave us an alternative way to identify fluid anomalies. Other methods included V_p / V_s ratio, Poisson's ratio reflectivity (Hilterman, 1989), and impedance contrast (Fatti et al., 1994). Elastic impedance, proposed by Connolly (1999), provided another approach to identify hydrocarbon anomalies using a partial stacking method.

Later, efforts to study the Lamé parameters: incompressibility (λ), rigidity (μ), and bulk modulus (K) attracted industry attention. It has been known that velocity is the main factor that dominates the wave propagation. In fact, the underlying physics demonstrates that the wave propagation is controlled by the Lamé parameters: incompressibility (λ), rigidity (μ), and density (ρ). Goodway et al. (1997) used Fatti et al.'s approximation to estimate the P-wave and S-wave impedance and further to derive the $\lambda\rho$ and $\mu\rho$ for fluid discrimination (LMR method). The $\lambda\rho$ term, dependent on the combination of rock matrix and fluid, is often called fluid term and the $\mu\rho$ term, only dependent on the rock

matrix, is called the lithology term. Goodway et al. argued that the LMR ratio (λ / μ) is the best fluid indicator to discriminate the fluid content in the porous sandstone.

Gray et al. (1999) reformulated the Zoeppritz's equation in terms of incompressibility reflectivity $\Delta\lambda / \lambda$, rigidity reflectivity $\Delta\mu / \mu$, bulk modulus reflectivity $\Delta K / K$, and density reflectivity $\Delta\rho / \rho$. These parameters offer an intuitive discrimination for the fluid changes in the porous sandstone, and also avoid squaring the impedances, thus enhancing noise, as is necessary in Goodway et al.'s method.

Recently, the research interest has moved to extracting pure fluid term using the theory of poroelasticity. The pore space modulus (K_p) method proposed by Hedlin (2000), the $K-\mu$ method proposed by Batzle et al. (2001), and the generalized fluid method proposed by Russell et al. (2003) used the standard poroelasticity theory (Biot, 1941, and Gassmann, 1951) to derive the pure fluid term which provides a direct look at the effect of pore fluid on the bulk modulus. The first two methods (Hedlin, 2000, Batzle et al., 2001) were derived under some assumptions. The pore space modulus method was based on the assumption: K_{dry} / μ=0.9 whereas the $K-\mu$ method was based on the assumption: K_{dry} / μ=1.0. To generalize these two methods, the generalized fluid method uses the scaling factor $(V_p / V_s)^2_{dry}$ to derive the generalized fluid method. The value of $(V_p / V_s)^2_{dry}$ depends on the dry rock property in the local reservoir and can be calibrated using core sample and well logs.

Although there are various methods to derive fluid terms to identify the fluid anomaly, these methods are based on various assumptions and which one is more sensitive to the fluid content in the pore space is still under debate. The objectives of this study are to:

1. Summarize various fluid discriminators and describe their theory background.
2. Use various datasets, such as laboratory measurements, well logs, and seismic data, to study the sensitivity of each fluid term to the fluid content.
3. Study the generalized fluid method proposed by Russell et al. (2003) to find the optimal value for $(V_p / V_s)^2_{dry}$.

1.2 Data used

Hilterman's (2001) Class I, II, and III sand models derived from Gulf of Mexico were used to diagnose the sensitivity of the each fluid indicator to the hydrocarbons in the gas and wet sandstones.

To diagnose the sensitivity of the generalized fluid term with other fluid indicators, Han's dataset (Han et al., 1986), which covers a wide range of porosities and clay contents at different pressure, was used. These samples are used not only for calculating the fluid terms but also for investigating the effect of clay content, porosity, and pressure on the value of $(V_p / V_s)^2_{dry}$ for the dry sandstone.

The Blackfoot 3C-3D P-P data shoot in 1995 was used to derive P-wave impedance, S-wave impedance, and fluid terms using the optimal value of $(V_p / V_s)^2_{dry}$ based on the well logs. The objective is to use the generalized fluid method to image the extension of porous sandstone within the Glauconitic incised valley system and the fluid information within the channel system in the Blackfoot area.

1.3 Hardware and software used

The work presented in this thesis was created on a Sun Microsystems network operated by the CREWES Project of the Department of Geology and Geophysics at University of Calgary. Crossplot analysis and regression analysis using the laboratory measurements and numerical examples were done in the MATLAB programming language. The well log data were loaded and stored using Geoview from Hampson-Russell Software Ltd. The Blackfoot 3C-3D data were processed to limited-offset gathers on PROMAX and VISTA. AVO analysis and AVO attributes were derived from the AVO package from Hampson-Russell Software Ltd. The P-P pre-stack inversion was performed using Strata package from Hampson-Russell Software Ltd. Word processing and thesis assembly was done on a PC based computer using Microsoft WORD.

1.4 Thesis organization

This thesis was divided into six chapters with this first chapter forming an introduction. Chapter 2 covers the basic principles of AVO and the previous fluid discrimination methods derived from AVO. In Chapter 2 various approximations of Zoeppritz's equation are reviewed and methodologies for the fluid discrimination were summarized. Chapter 3 deals with the Biot-Gassmann theory and methodology of the generalized fluid method proposed by Russell et al. (2003). In Chapter 4, Han's dataset (Han et al., 1986) is used to investigate the effect of clay content, porosity, and pressure on the P-wave and S-wave velocity ratio for dry sandstones, which is scale factor for the generalized fluid term calculation. In Chapter 5, numerical examples and lab measurements are used to diagnose the sensitivity of the generalized fluid term with other fluid indicators. Chapter 6 covers a real seismic data example for the generalized fluid method to map the upper

and lower valley porous sandstone in the Glauconitic valley system and fluid information inside the channel system, using the Blackfoot dataset.

1.5 The contribution of this thesis

The key issue in the generalized fluid method proposed by Russell et al. (2003) is to derive an accurate value for P-wave and S-wave velocity ratio $(V_p/V_s)_{dry}$ for the dry rock. In this study Han's dataset (Han et al., 1986) was used to better understand the effect of clay content, porosity, and pressure on the compressional velocity, shear velocity, and $(V_p/V_s)_{dry}$ for the dry sandstone. Through this study it can be concluded that $(V_p/V_s)_{dry}$ for the dry sandstone increases with porosity and decreases with clay content. The average value of $(V_p/V_s)_{dry}$ for the dry clean sandstone is around 1.52 and 1.55 for the dry shaly sandstone.

The generalized fluid method was applied to the numerical examples of Class I, II, and III sand models given by Hilterman (2001) and Han's dataset (Han et al., 1986) to diagnose the sensitivity of the generalized fluid term with other fluid indicators. Through this study, it can be concluded that porosity, clay content, and pressure will affect the discrimination capability of the generalized fluid method. The analysis results also show there is a great deal of equivalence between fluid indicators: $Ip^2 - c*Is^2$, $K-\mu$, $\lambda\rho$, λ/μ. For the core measurements of sandstones, the attribute $Ip^2 - c*Is^2$ is the most sensitive fluid term in absolute terms. However, most of these indicators give the similar results in magnitude and each can give us insights into the meaning of the others.

The generalized fluid method was also applied to the Blackfoot P-P seismic data in order to map the upper and lower incised valleys and to identify the fluid information within

the incised valley system. The results showed the successful discriminate of the upper and lower incised valleys from the background and the heterogeneity inside the channel system.

The main contributions of this thesis are as follows:

1. The optimal $(V_p / V_s)_{dry}$ value for the dry sandstone for extracting the exact fluid term using the generalized fluid method is determined and the effect of clay content, porosity, and pressure on the compressional velocities, shear velocity, and $(V_p / V_s)_{dry}$ of sandstones is also determined.

2. The fluid discrimination capability for various fluid indicators and their inherent connection with each other is examined.

3. The generalized fluid method is applied to the real seismic data to derive the fluid term and to investigate its feasibility and veracity.

4. It is determined that, compared with other fluid indicators, the generalized fluid method can successfully discriminate the upper and lower incised valleys from the background and the fluid information inside the channel system, when used on the Blackfoot P-P seismic data.

CHAPTER TWO: AVO THEORY AND FLUID EXTRACTION METHODS

2.1 Introduction

This chapter will review various linearized approximations to the Zoeppritz equations and discuss the connections between these approximations. All these approximations reformulate the linearized Zoeppritz equations in different terms to emphasize each term's contribution to the amplitude variations using different assumptions. Summarizing all these approximations, the generalized linearized equation proposed by Russell et al. (2006) is also introduced.

This chapter also covers various fluid indicators derived from these approximations to the Zoeppritz equations. Some fluid indicators relate the presence of hydrocarbon to the direct AVO response, such as bright-spot and dim-out. Some fluid indicators, such as V_p / V_s ratio and Fluid factor, are used to measure the effect of fluid saturation on the seismic properties. Furthermore, some indicators relate the presence of hydrocarbon to the more intuitive physical parameters, such as incompressibility (λ) and bulk modulus (K). All these fluid indicators have been successfully used to discriminate the hydrocarbon-charged reservoir from the background or wet sand and cross plot analysis of these parameters allows us to highlight the anomalies which infer the fluid content.

2.2 The linearized AVO equation

Knott (1899) and Zoeppritz (1919) developed the theoretical work necessary for AVO theory based on an earth model of a two layer elastic medium with a single horizontal interface. They developed equations for plane-wave reflection amplitude variation as a function of incident angle. Koefoed (1955) described the relationship between the amplitude variation with offset and change in Poisson's ratio across the boundary.

Koefoed's results were based on the exact Zoeppritz equations. The conclusions drawn by Koefoed are the basis of today's AVO interpretation. Afterwards, Bortfeld (1961) derived a linearized approximation to the Zoeppritz equations, which is the basis of other approximations.

2.2.1 The Zoeppritz equations

The Zoeppritz equations describe the amplitudes of the reflected and transmitted P-wave and S-wave when a P-wave is incident at a boundary between two elastic media. In general, this process will produce two reflected waves and two transmitted waves. The energy of the incident wave is divided among these four components in proportion which depend on the P-wave and S-wave velocities, density, and the angle of incidence. Figure 2.1 illustrates the reflection, transmission, and mode conversion of a P-wave at a boundary.

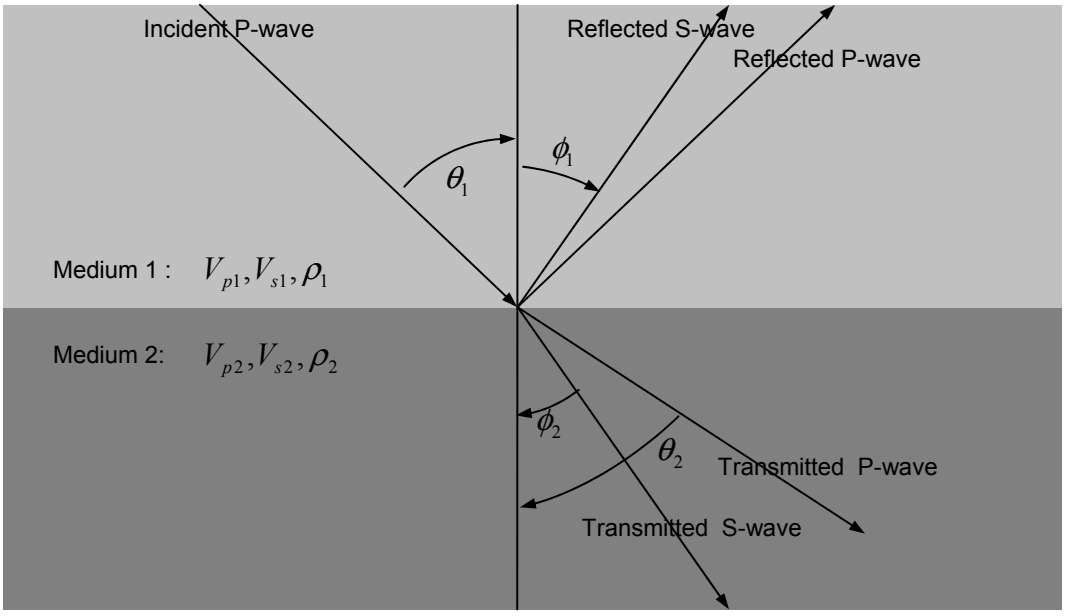

Figure 2.1 The partition of energy among reflected and transmitted P-wave and S-wave at a layer boundary.

The Zoeppritz equations provide the exact solution for the energy partition among the reflected and transmitted P-waves and S-waves but have complicate form which are expressed in equation (2.1):

$$\begin{bmatrix} R_p \\ R_s \\ T_p \\ T_s \end{bmatrix} = \begin{bmatrix} -\sin\theta_1 & -\cos\phi_1 & \sin\theta_2 & \cos\phi_2 \\ \cos\theta_1 & -\sin\phi_1 & \cos\theta_2 & -\sin\phi_2 \\ \sin 2\theta_1 & \frac{V_{P1}}{V_{S1}}\cos 2\phi_1 & \frac{\rho_2 V^2{}_{S2} V_{P1}}{\rho_1 V^2{}_{S1} V_{P2}}\sin 2\theta_2 & \frac{\rho_2 V_{S2} V_{P1}}{\rho_1 V^2{}_{S1}}\cos 2\phi_2 \\ -\cos 2\phi_1 & \frac{V_{S1}}{V_{P1}}\sin 2\phi_1 & \frac{\rho_1 V_{P2}}{\rho_1 V_{P1}}\cos 2\phi_2 & -\frac{\rho_2 V_{S2}}{\rho_1 V_{P1}}\sin 2\phi_2 \end{bmatrix}^{-1} \begin{bmatrix} \sin\theta_1 \\ \cos\theta_1 \\ \sin 2\theta_1 \\ \cos 2\phi_1 \end{bmatrix}, \quad (2.1)$$

where, the four unknown values R_p, R_s, T_p, and T_s are reflected P-wave, reflected S-wave, transmitted P-wave, and transmitted S-wave amplitudes, V_{P1} and V_{S1} are P-wave and S-wave velocities for the top layer, V_{P2} and V_{S2} are P-wave and S-wave velocities for the bottom layer. ρ_1 and ρ_2 are densities for the top and bottom layers. The angles θ_1, θ_2, ϕ_1, and ϕ_2 are denoted in Figure 2.1. These equations require the continuity of normal and tangential components of displacements and stress. They assume a plan wave at the interface of two homogenous, isotropic, elastic, and lossless media.

2.2.2 Bortfeld approximation

The Zoeppritz equations allow us to understand how the amplitude of the reflected P-wave changes with the incident angle. The non-linearized form of the Zoeppritz equations are so complicated that they don't give us an intuitive understanding of how these amplitude changes relate to various rock properties. Over the years, a number of linearized approximations to the Zoeppritz equations have been made, which make the interpretation more intuitive. Among them, the first approximation to the Zoeppritz equation for P-P reflection amplitude is reformulated by Bortfeld (1961):

$$R(\theta_1) = \frac{1}{2}\ln\left(\frac{V_{p2}\rho_2\cos\theta_2}{V_{p1}\rho_1\cos\theta_1}\right) + \left[2 + \frac{\ln\frac{\rho_2}{\rho_1}}{\ln\frac{V_{p2}}{V_{p1}} - \ln\frac{V_{p2}V_{s1}}{V_{p1}V_{s2}}}\right]\frac{V_{s1}^{\ 2} - V_{s2}^{\ 2}}{V_{p1}^{\ 2}}\sin^2\theta_1, \quad (2.2)$$

where, V_{p1} and V_{s1} are P-wave and S-wave velocities for the top layer, V_{P2} and V_{S2} are P-wave and S-wave velocities for the bottom layer; ρ_1 and ρ_2 are densities for the top and bottom layers; θ_1 and θ_2 are the reflection and transmission angles for P-wave.

The first term in the Bortfeld's approximation is mainly related to the P-wave velocity and so called the fluid term whereas the second term is mainly related to the S-wave velocity and so called the rigidity term. Although the Bortfeld's approximation provides us an insight into the amplitude variation as a function of rock properties, it does not explicitly indicate the amplitude variation with the incident angle.

2.2.3 Aki-Richards-Frasier approximation

The Bortfeld approximation was further reformulated by Richards and Frasier (1976) and re-published by Aki and Richards (1980). The Aki-Richards-Frasier approximation is written in three terms, the first term involving P-wave velocity, the second term involving S-wave velocity, and the third term involving density. Their formula can be written as:

$$R(\theta) = \left[\frac{1}{2}\left(1 + \tan^2\theta\right)\right]\frac{\Delta V_p}{V_p} - \left[4\frac{V_s^{\ 2}}{V_p^{\ 2}}\sin^2\theta\right]\frac{\Delta V_s}{V_s} + \left[\frac{1}{2}\left(1 - 4\frac{V_s^{\ 2}}{V_p^{\ 2}}\sin^2\theta\right)\right]\frac{\Delta\rho}{\rho}, \quad (2.3)$$

where $V_p = (V_{p1} + V_{p2})/2$, average P-wave velocity, $\Delta V_p = V_{p2} - V_{p1}$,

$V_s = (V_{s1} + V_{s2})/2$, average S-wave velocity, $\Delta V_s = V_{s2} - V_{s1}$, $\rho = (\rho_1 + \rho_2)/2$, average

density, $\Delta\rho = \rho_2 - \rho_1$, and $\theta = (\theta_1 + \theta_2)/2$, average of the incidence and transmission angles for P-wave.

The Aki-Richards-Frasier approximation attributed the amplitude variation to the separate variation in the P-wave velocity, S-wave velocity, and density. Equation (2.3) can be used to derive P-wave reflectivity, S-wave reflectivity, and density reflectivity. However, in practice, it is not easy to derive the three terms because the coefficient of first term and third term are very close for moderate incident angles (i.e. less than 30 degrees), which make the inversion process unstable.

2.2.4 Shuey's approximation

The Shuey's approximation (Shuey, 1985) gave the explicit form relating the amplitude variation to the incident angle:

$$R(\theta) = [\frac{1}{2}(\frac{\Delta V_p}{V_p} + \frac{\Delta\rho}{\rho})] + [\frac{1}{2}\frac{\Delta V_p}{V_p} - 4\frac{{V_s}^2}{{V_p}^2}\frac{\Delta V_s}{V_s} - 2\frac{{V_s}^2}{{V_p}^2}\frac{\Delta\rho}{\rho}]\sin^2\theta + [\frac{1}{2}\frac{\Delta V_p}{V_p}](\tan^2\theta - \sin^2\theta) \quad . \qquad (2.4)$$

Afterwards, equation (2.4) was rewritten in term of Poisson's ratio rather than S-wave velocity:

$$R(\theta) = \left[\frac{1}{2}(\frac{\Delta V_p}{V_p} + \frac{\Delta\rho}{\rho})\right] + \left[\frac{1}{2}\frac{\Delta V_p}{V_p}\left(2\frac{\Delta V_p}{V_p} + \frac{\Delta\rho}{\rho}\right)\left(\frac{1-2\sigma}{1-\sigma}\right) + \frac{\Delta\sigma}{(1-\sigma)^2}\right]\sin^2\theta, \qquad (2.5)$$
$$+ \frac{\Delta V_p}{2V_p}(\tan^2\theta - \sin^2\theta)$$

Setting the S-wave to P-wave velocity ratio $V_s/V_p = 0.5$ and dropping the third term when the incident angle is less than 30 degrees, equation (2.4) can be rewritten as:

$$R(\theta) = [\frac{1}{2}(\frac{\Delta V_p}{V_p} + \frac{\Delta \rho}{\rho})] + [\frac{1}{2}\frac{\Delta V_p}{V_p} - \frac{\Delta V_s}{V_s} - \frac{1}{2}\frac{\Delta \rho}{\rho}]\sin^2\theta . \quad (2.6)$$

Since the linearized P-wave and S-wave reflectivity can be written as:

$$R_p \cong \frac{1}{2}(\frac{\Delta V_p}{V_p} + \frac{\Delta \rho}{\rho}), \text{ and} \quad (2.7)$$

$$R_s \cong \frac{1}{2}(\frac{\Delta V_s}{V_s} + \frac{\Delta \rho}{\rho}) . \quad (2.8)$$

We can substitute equation (2.7) and equation (2.8) into equation (2.6) to get:

$$R(\theta) = R_p + (R_p - 2R_s)\sin^2\theta = R_p + G\sin^2\theta , \quad (2.9)$$

where $G = R_p - 2R_s$, $R_s = (R_p - G)/2$.

Considering $\sin^2\theta$ as a variable, linear regression can be performed on equation (2.9) to estimate intercept R_p and gradient G. Given AVO intercept R_p and AVO gradient G attributes, shear wave reflectivity R_s can be derived using the equation: $R_s = (R_p - G)/2$.

2.2.5. Hilterman's approximation

Using the assumption: $V_p / V_s = 2$, Hilterman (1995) rearranged Shuey's equation to another popular approximation to solve for delta Poisson's ratio reflectivity:

$$R(\theta) = R_p \cos^2\theta + \frac{\Delta\sigma}{(1-\sigma)^2}\sin^2\theta . \quad (2.10)$$

The delta Poisson's ratio reflectivity in equation (2.10) can be defined as:

$$\frac{\Delta\sigma}{(1-\sigma)^2} = 8\left(\frac{V_s}{V_p}\right)^2 (R_p - R_s) , \quad (2.11)$$

where R_p and R_s are the normal incident reflectivities for P-wave and S-wave , respectively.

Equation (2.10) highlights the Poisson's ratio change, which is indicative of fluid content or lithology changes.

2.2.6 Smith and Gidlow approximation

Smith and Gidlow (1987) gave another approximation based on the Aki and Richards equation. They first rearranged the equation as:

$$R(\theta) = [\frac{1}{2}(\frac{\Delta V_p}{V_p} + \frac{\Delta \rho}{\rho})] - 2\frac{V_s^{\ 2}}{V_p^{\ 2}}[2\frac{\Delta V_s}{V_s} + \frac{\Delta \rho}{\rho}]\sin^2\theta + \frac{1}{2}\frac{\Delta V_p}{V_p}\tan^2\theta . \quad (2.12)$$

And then they simplified equation (2.12) by removing the dependence on density by using Gardner's relationship:

$$\rho = aV_p^{\ 1/4} . \quad (2.13)$$

Equation (2.13) can be differentiated to give:

$$\frac{\Delta \rho}{\rho} = \frac{1}{4}\frac{\Delta V_p}{V_p} . \quad (2.14)$$

Substituting equation (2.14) into equation (2.12) gives:

$$R(\theta) = c\frac{\Delta V_p}{V_p} + d\frac{\Delta V_s}{V_s} , \quad (2.15)$$

where $c = 5/8 - 1/2\left(V_s^{\ 2}/V_p^{\ 2}\right)\sin^2\theta + 1/2\tan^2\theta$ and $d = -4(V_s^{\ 2}/V_p^{\ 2})\sin^2\theta$.

Using equation (2.15), P-wave reflectivity $\Delta V_p / V_p$ and S-wave reflectivity $\Delta V_s / V_s$ can be estimated by least-squares regression. Smith and Gidlow also derived two other attributes (Pseudo-Poisson's ratio reflectivity and the fluid factor) to infer the fluid content.

2.2.7 Fatti et al.'s approximation

Aki-Richards approximation was rearranged into equation (2.16) by Fatti et al. (1994):

$$R(\theta) = \frac{1}{2}[1+\tan^2\theta]\frac{\Delta I_p}{I_p} + 4\frac{V_s^{\,2}}{V_p^{\,2}}\sin^2\theta\frac{\Delta I_s}{I_s} - [\frac{1}{2}\tan^2\theta - 2\frac{V_s^{\,2}}{V_p^{\,2}}\sin^2\theta]\frac{\Delta\rho}{\rho} \quad . \tag{2.16}$$

Equation (2.16) can be simplified by dropping the third term in the equation when the incident angle is less than 30 degrees:

$$R(\theta) = \frac{1}{2}[1+\tan^2\theta]\frac{\Delta I_p}{I_p} + 4\frac{V_s^{\,2}}{V_p^{\,2}}\sin^2\theta\frac{\Delta I_s}{I_s} \quad . \tag{2.17}$$

Equation (2.17) is often used to derive P-wave and S-wave reflectivities, and then to estimate the P-wave and S-wave impedance.

2.2.8 Gray's approximation

Gray et al. (1999) formulated Aki-Richards approximation in terms of incompressibility (λ), rigidity (μ), bulk modulus (K), and density (ρ):

$$R(\theta) = [\frac{1}{4} - \frac{1}{2}\frac{V_s^{\,2}}{V_p^{\,2}}]\sec^2\theta\frac{\Delta\lambda}{\lambda} + \frac{V_s^{\,2}}{V_p^{\,2}}[\frac{1}{2}\sec^2\theta - 2\sin^2\theta]\frac{\Delta\mu}{\mu} + [\frac{1}{2} - \frac{1}{4}\sec^2\theta]\frac{\Delta\rho}{\rho} \quad \text{, and} \tag{2.18}$$

$$R(\theta) = [\frac{1}{4} - \frac{1}{3}\frac{V_s^{\,2}}{V_p^{\,2}}]\sec^2\theta\frac{\Delta K}{K} + \frac{V_s^{\,2}}{V_p^{\,2}}[\frac{1}{3}\sec^2\theta - 2\sin^2\theta]\frac{\Delta\mu}{\mu} + [\frac{1}{2} - \frac{1}{4}\sec^2\theta]\frac{\Delta\rho}{\rho} \quad . \tag{2.19}$$

Equation (2.18) and equation (2.19) give the explicit forms relating the amplitude variation to the elastic rock parameters and incident angle. However, the challenge of this method is to get the appropriate value for V_s / V_p ratio because the inaccuracy of the V_s / V_p ratio will affect the inversion process (Gray et al., 1999).

2.2.9 The general linearized equation

As just shown, there are numerous linearized approximations of the Zoeppritz equation, each with a different emphasis. Bortfeld's equation (1961) emphasized the fluid and rigidity terms, which provided insight when interpreting fluid substitution, while Aki and Richards' equation (1980) emphasized the contribution of variations in the P-wave and S-wave velocities and density. Shuey's equation (1985) relates the amplitude variation to changes in Poisson's ratio, P-wave velocity, and density. The equation proposed by Smith and Gidlow (1987) can be used to extract P-wave and S-wave velocity reflectivities and then to derive the fluid factor. Fatti et al.'s equation (1994) gives us a direct estimation of P-wave impedance and S-wave impedance, based on which Goodway et al. (1997) proposed LMR method. Hilterman's approximation (1995) can be used to derive P-wave reflectivity and Poisson's reflectivity. Gray et al.'s equation (1999) is used to extract Lambda reflectivity $\Delta\lambda / \lambda$, Mu reflectivity $\Delta\mu / \mu$, and bulk modulus reflectivity $\Delta K / K$.

To generalize the linearized approximations above, Russell et al. (2006) expressed the Zoeppritz equation in three terms:

$$R(\theta) = aR_1 + bR_2 + cR_3 . \tag{2.20}$$

where a, b, and c are the coefficient which are functions of incident angle and $(Vp/Vs)^2$, R_i are reflectivity terms for the rock properties. Table 2.1 and Table 2.2 summarize the corresponding terms for a, b, c and R_i for each approximation.

Table 2.1 R_i terms for the general linearized equation (Modified from Russell et al., 2006).

Approximations	R_1	R_2	R_3	**Assumption**
Aki-Richards (1980)	$\frac{\Delta V_p}{V_p}$	$\frac{\Delta V_s}{V_s}$	$\frac{\Delta \rho}{\rho}$	From Bortfeld's approximation
Shuey (1985)	$\frac{\Delta I_p}{I_p}$	$\frac{\Delta I_p}{I_p} - 2\frac{\Delta I_s}{I_s}$	$\frac{\Delta V_p}{2V_p}$	The third term can be ignored for $\theta < 30^o$; Assume $V_p / V_s = 2$
Smith and Gidlow (1987)	$\frac{\Delta V_p}{V_p}$	$\frac{\Delta V_s}{V_s}$	$\frac{\Delta V_p}{2V_p}$	Gardner's relationship for density; No assumption for incident angle
Fatti et al. (1994)	$\frac{\Delta I_p}{I_p}$	$\frac{\Delta I_s}{I_s}$	$\frac{\Delta \rho}{\rho}$	The third term can be ignored for $\theta < 30^o$
Hilterman (1995)	$\frac{\Delta I_p}{I_p}$	$\frac{\Delta \sigma}{(1-\sigma)^2}$	0	From Shuey's approximation Assume $V_p / V_s = 2$
Gray ($\lambda\mu\rho$) (1999)	$\frac{\Delta \lambda}{\lambda}$	$\frac{\Delta \mu}{\mu}$	$\frac{\Delta \rho}{\rho}$	No assumption
Gray ($K\mu\rho$) (1999)	$\frac{\Delta K}{K}$	$\frac{\Delta \mu}{\mu}$	$\frac{\Delta \rho}{\rho}$	No assumption

Table 2.2 Terms a, b, and c for the general linearized equation (Modified from Russell et al., 2006).

Approximations	a	b	c
Aki-Richards (1980)	$\frac{\sec^2\theta}{2}$	$-\frac{4}{\gamma^2_{sat}}\sin^2\theta$	$\frac{1}{2}-\frac{2}{\gamma^2_{sat}}\sin^2\theta$
Shuey (1985)	1	$\sin^2\theta$	$\tan^2\theta-\sin^2\theta$
Smith and Gidlow (1987)	$5-\frac{1}{2}\frac{\sin^2\theta}{\gamma^2_{sat}}+\frac{\tan^2\theta}{2}$	$-4\frac{\sin^2\theta}{\gamma^2_{sat}}$	$\tan^2\theta$
Fatti et al. (1994)	$1+\tan^2\theta$	$-\frac{8\sin^2\theta}{\gamma^2_{sat}}$	$\frac{2\sin^2\theta}{\gamma^2_{sat}}-\frac{1}{2}\tan^2\theta$
Hilterman (1995)	$\cos^2\theta$	$\sin^2\theta$	0
Gray ($\lambda\mu\rho$) (1999)	$\left(\frac{1}{4}-\frac{1}{2\gamma^2_{sat}}\right)\sec^2\theta$	$\frac{\sec^2\theta-4\sin^2\theta}{2\gamma^2_{sat}}$	$\frac{1}{2}-\frac{1}{4}\sec^2\theta$
Gray ($K\mu\rho$) (1999)	$\left(\frac{1}{4}-\frac{1}{3\gamma^2_{sat}}\right)\sec^2\theta$	$\frac{\sec^2\theta-6\sin^2\theta}{3\gamma^2_{sat}}$	$\frac{1}{2}-\frac{1}{4}\sec^2\theta$

2.3 Early fluid extraction methods

2.3.1 Intercept and gradient

Intercept and gradient analysis is a well known standard approach for AVO analysis. The intercept and gradient can be derived using Shuey's (1985) approximation (equation 2.4), which can be simplified as:

$$R(\theta) = A + B\sin^2\theta + C\sin^2(\theta)\tan^2(\theta), \qquad (2.22)$$

where R is the reflection coefficient, A is the normal incidence reflectivity or intercept, the same term R_p used in equation (2.9), B is the incident angle dependence term or gradient, the same term G used in equation (2.9), and C is a curvature term. For incident angles less than 30 degrees, the C term may be dropped.

Castagna and Smith (1994) argued that the product of A and B is often used to verify the classical bright spots because the low impedance gas sand encased in shale will have a larger negative intercept (A) and a larger negative gradient (B). Therefore, the product of A and B should be an excellent indicator for class III type gas sand. Furthermore, the combination of A and B also gives estimations for other attributes.

Assuming $V_p / V_s = 2$, the sum of A and B ($A+B$) will give an estimation of Poisson's ratio reflectivity $\Delta\sigma$ and the subtraction of B from A (A - B) will give the estimation of S-wave reflectivity (Castagna and Smith, 1994).

The crossplot of A versus B can reveal different AVO behaviours. Based on Castagna et al.'s (1998) analysis, there is a background trend line in the crossplot of A versus B for the wet sand and shale. This line is a function of the background V_p / V_s ratio. The deviation from the background trend line indicates the presence of hydrocarbon. This is

the basis of Smith and Gidlow's (1987) fluid factor method and other related indicators to be discussed in the next section.

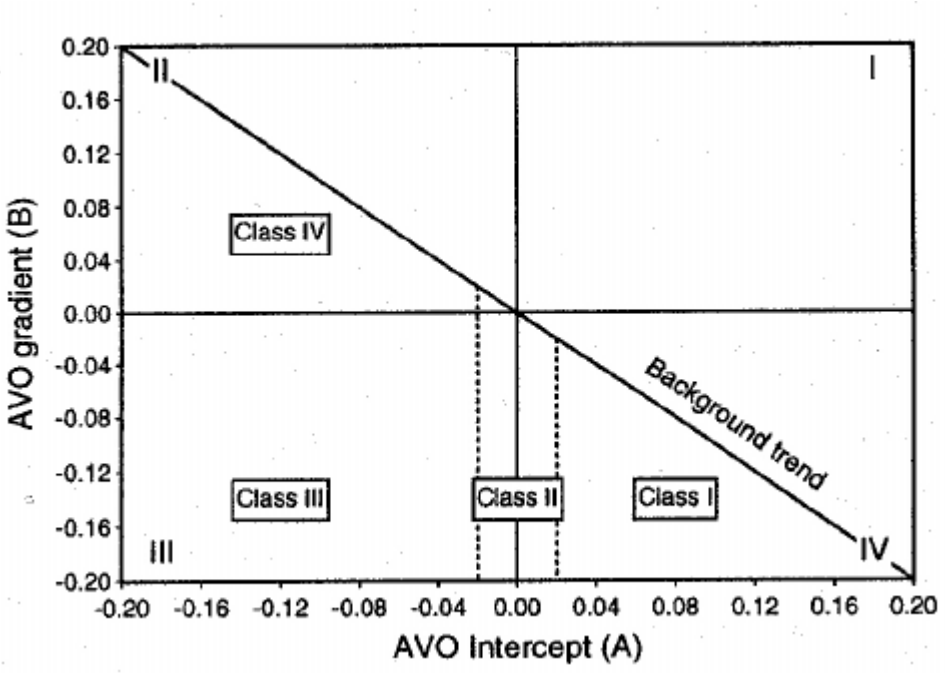

Figure 2.2 AVO intercept (A) versus gradient (B) crossplot showing four possible quadrants (Castagna et al., 1998).

Using the crossplot of A versus B, hydrocarbon-saturated sands can be classified according to their locations in the A-B plane. According to Castagna et al.'s (1998) analysis, the top of Class III gas sand should fall into the third quadrant (negative A and B). Conversely, the bottom of a gas sand should fall into the first quadrant (positive A and B). The top of Class I gas sand will fall into the fourth quadrant (positive A and negative B). The top of Class II gas sand will fall between the second quadrant and the fourth quadrant. The top of Class IV gas sand will fall into the second quadrant (negative

A and positive B). Figure 2.2 shows the quadrant location in the Cartesian coordinate system for Class I, II, III, and IV gas sands.

2.3.2 The fluid factor

The fluid factor method was introduced by Smith and Gidlow (1987) using Castagna's mudrock line. Castagna et al. (1985) defined a straight line called mud-rock line in the plane of P-wave velocity versus S-wave velocity as shown in Figure 2.3. The line is defined by the equation:

$$V_p \approx a + bV_s = 1360 + 1.16V_s, \tag{2.23}$$

where a and b are empirically determined from the well logs or rock samples. For a water-saturated sand the suggested values for a and b are 1360 m/sec and 1.16 (Castagna et al., 1985). Deviation from the mudrock line indicates the presence of hydrocarbon or a lithology change.

Differentiating both sides of equation 2.23 gives:

$$\frac{\Delta V_p}{V_p} = b\frac{V_s}{V_p}\frac{\Delta V_s}{V_s}. \tag{2.24}$$

The P-wave velocity reflectivity $\Delta Vp/Vp$ and S-wave velocity reflectivity $\Delta Vs/Vs$ can be derived from equation (2.15). The P-wave velocity reflectivity $\Delta Vp/Vp$ also can be estimated directly from the equation (2.24).

The fluid factor is therefore defined as:

$$\Delta F = \frac{\Delta V_p}{V_p} - b\frac{V_s}{V_p}\frac{\Delta V_s}{V_s}, \tag{2.25}$$

where the first term can be derived from equation (2.15), and the second term can be estimated based on the S-wave velocity reflectivity using the mud-rock line. Equation

(2.25) was later reformulated by Fatti et al. (1994) in terms of P-wave and S-wave reflectivities:

$$\Delta F = R_p - 1.16\frac{V_s}{V_p}R_s . \qquad (2.26)$$

For gas-saturated sandstones, the fluid factor will be negative whereas it will be near zero for water-saturated sandstones and shale. It should be noticed that lithology also can produce a fluid factor anomaly. Therefore, care must be taken to define the background trend based on the known lithology. For example, it is different for carbonate (Castagna and Backus, 1993).

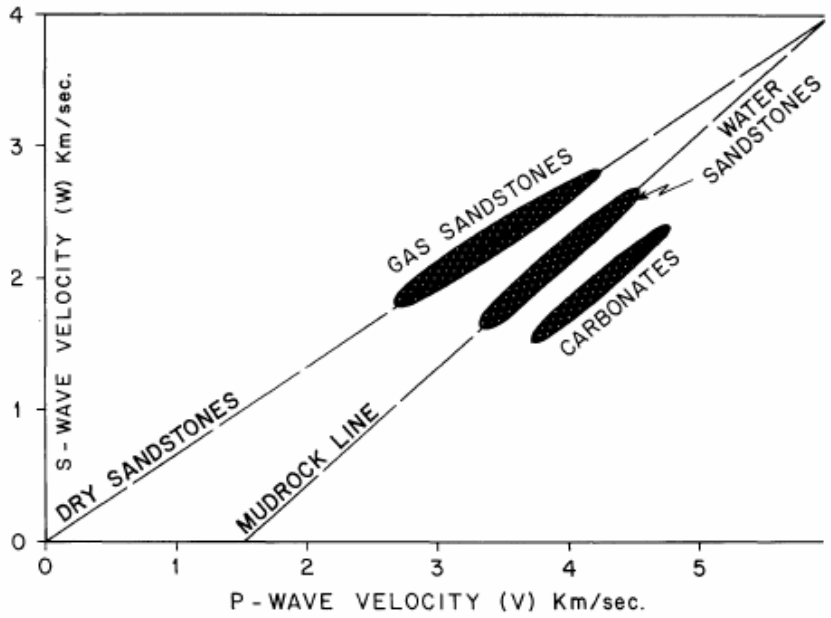

Figure 2.3 Crossplot of P-wave velocity versus S-wave velocity (Castagna et al. 1985).

2.3.3 Elastic impedance

The concept of elastic impedance was introduced by Connolly (1999). It has been proven to be a useful method for fluid and lithology discrimination. Inspired by the normal-incidence reflection coefficient defined by the acoustic impedance contrast between the

lower and upper media, Connolly (1999) proposed an alternative expression for the P-wave reflection coefficient at the given incidence angle in the following form:

$$R(\theta) = \frac{EI_2 - EI_1}{EI_2 + EI_1} \approx \frac{1}{2}\frac{\Delta EI}{EI} \approx \frac{1}{2}\Delta \ln(EI), \tag{2.27}$$

where EI is elastic impedance which is the function of P-wave velocity, S-wave velocity, and density.

Based on Aki and Richards' approximation for the Zoeppritz equation, substituting constant factor $K = (Vs/Vp)^2$ and the equation $\Delta \ln x = \Delta x / x$, Aki-Richards equation (2.3) can be reformulated:

$$\Delta \ln(EI) = \Delta \ln\left(V_p^{(1+\tan^2\theta)} V_s^{(-8K\sin^2\theta)} \rho^{(1-4K\sin^2\theta)}\right). \tag{2.28}$$

Equation (2.28) can be rewritten to get the expression for EI :

$$EI(\theta) = V_p^{(1+\tan^2\theta)} V_s^{(-8K\sin^2\theta)} \rho^{(1-4K\sin^2\theta)}, \tag{2.29}$$

where $K = (Vs/Vp)^2$. It is noticed that $EI(0)$ is same as acoustic impedance (AI).

Connolly (1999) demonstrated the capability of EI to discriminate an oil sand from the background using a suite of logs. Figure 2.4 showed the computed curves for AI and EI at 30 degrees. It can be observed that there is significant difference between the elastic impedance and acoustic impedance, which is indicative to the presence of hydrocarbon in sandstones.

Range limit stack processing of the seismic data can provide the near offset and far offset stack profiles. Near offset stack profile represents the elastic impedance for the small incident angles and far offset stack profile represents the elastic impedance for the larger incident angle. Examining the difference between these two stack profiles can infer the presence of hydrocarbon.

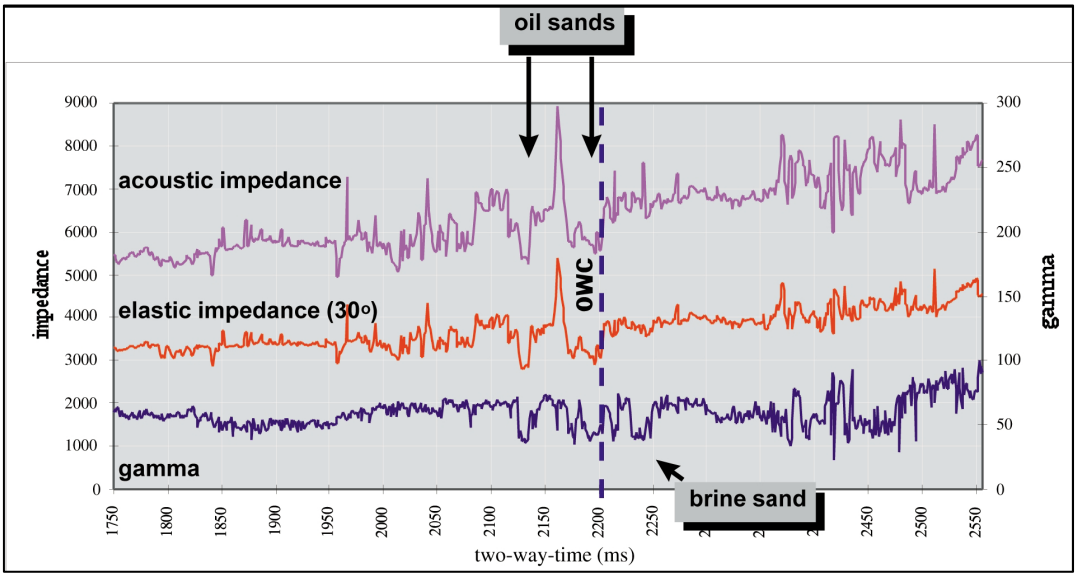

Figure 2.4 The acoustic impedance (AI) and Elastic Impedance (EI) curves at 30 degrees (Connolly, 1999).

2.3.4 The LMR method

Goodway et al. (1997) proposed the LMR method based on Fatti et al.'s approximation for the Zoeppritz equation. P-wave reflectivity $\Delta I_p / I_p$ and S-wave reflectivity $\Delta I_s / I_s$ can be estimated from equation (2.17). Following the estimation of the P-wave and S-wave reflectivity, the P-wave and S-wave impedance can be computed by the inversion process. By using the impedance attributes: Ip and Is , Goodway et al. (1997) proposed two attributes: $\lambda\rho$ and $\mu\rho$ for discrimination of fluid and lithology change:

$$\begin{aligned} \lambda\rho &= I^2{}_p - 2I^2{}_s \\ \mu\rho &= I^2{}_s \end{aligned} \quad . \tag{2.30}$$

This approach is widely used and is called the LMR (lambda-mu-rho) method, where L, M, and R represent λ , the first Lamé parameter, μ , the shear modulus or second Lamé

parameter, and ρ, the density. It was observed by Goodway et al. (2001) that $\lambda\rho$ and $\mu\rho$ are more orthogonal in crossplot space than Ip versus Is, which enables us to use $\lambda\rho$ versus $\mu\rho$ as a effective indicator to separate the gas sand from wet sand or shale (Figure 2.5). Goodway et al. (2001) also argued that the value of λ/μ is more sensitive to fluid discrimination than other attributes, such as λ, $\lambda\rho$, V_p/V_s, or σ.

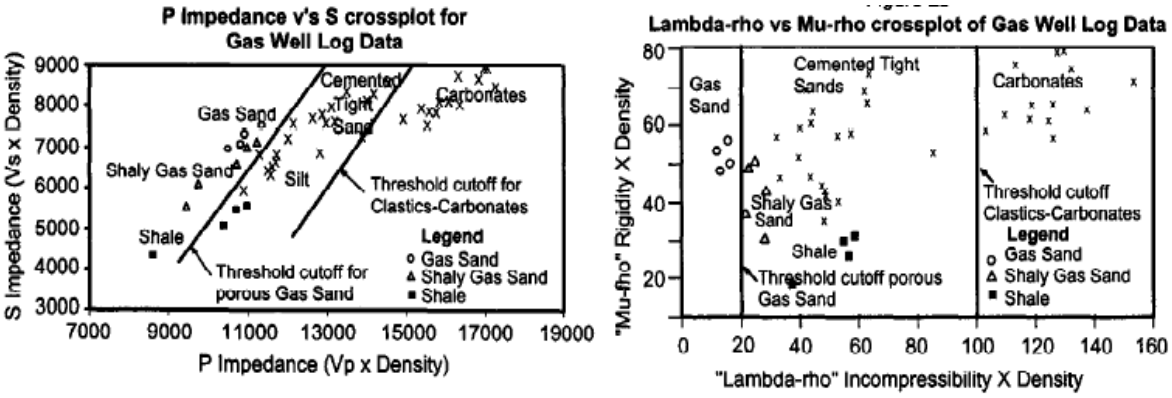

Figure 2.5 Crossplot of P-impedance versus S-impedance (left) and lambda-rho versus Mu-rho (right) (Goodway et al., 1997).

2.3.5 Pore space modulus (Kp)

Hedlin (2000) argued that Lambda and Vp/Vs are not only related to the pore fluid but also contains the contribution of the rock skeleton. His work was based on an empirical study by Murphy et al. (1993). The changes of Lambda and Vp/Vs don't only represent the fluid change in the pore space, but also the change in the rock skeleton. The change of the fluid can be estimated from the second term in the Gassmann equation which represents the contribution of the pore fluid to the bulk modulus of a porous rock.

Therefore, Hedlin (2000) proposed the pore space modulus (K_p) method to measure the effect of fluid change on the bulk modulus.

Based on the theory of poroelasticity, the sedimentary rocks are composed of fluid and minerals. Seismic wave transmitting through the porous rock will have P-wave and S-wave velocities estimated as:

$$V_p = \sqrt{(\lambda + 2\mu)/\rho} = \sqrt{(K + 4/3\mu)/\rho} \text{ , and} \tag{2.31}$$

$$V_s = \sqrt{\mu/\rho}\,, \tag{2.32}$$

where Vp and Vs are P-wave and S-wave velocities, K is bulk modulus, λ is the Lamé parameter or incompressibility, μ is shear modulus or rigidity, and ρ is density.

Hedlin (2000) rewrote the equation (2.31) as:

$$V_p = \sqrt{(K_p + K_{dry} + 4/3\mu)/\rho}\,. \tag{2.33}$$

where K_{dry} is the bulk modulus of the drained rock framework, and K_p is pore space modulus.

Equation (2.33) divides by Equation (2.32) will get:

$$\gamma^2 = \left(\frac{Vp}{Vs}\right)^2 = \frac{K_p}{\mu} + \frac{K_{dry}}{\mu} + \frac{4}{3}. \tag{2.34}$$

Equation (2.34) suggest that the change of Vp/Vs comes from two parts. One part involves the rock skeleton because K_{dry} and μ are independent of pore fluid. So the pore fluid contribution lies in K_p/μ term.

Hedlin (2000) used the empirically derived *Vp*-*Vs* and *Vp*-density relationships from Mavko et al.'s (1998) analysis to obtain K_{dry}/μ =0.9 and $K_p = \rho V_p^{\,2} - 2.233\rho V_s^{\,2}$.

Hedlin (2000) argued that the value of 0.9 for K_{dry} / μ is valid only for clean sandstone (Murphy et al, 1993), for shaly sandstones, the presence of clay may affect the values of K_{dry} by softening the grain contacts and lowering the frame modulus. Given the optimal value for K_{dry} / μ, the value of K_p from the seismic data can offer a good discrimination for the fluid content in the potential hydrocarbon reservoirs.

CHAPTER THREE: BIOT-GASSMANN THEORY FOR POROUS ROCK

3.1 Introduction

This chapter will introduce Biot-Gassmann theory, enabling us to understand how the fluid in the porous rock affects the elastic modulus of the rock and in turn affect the P-wave and S-wave velocities. Biot-Gassmann theory plays an important role in seismic rock physics analysis and provides a powerful tool to study the seismic response due to changes in lithology, porosity, saturation, and fluids. The concepts of Biot-Gassmann theory and the formulation, and limitation of the Gassmann fluid substitution will be discussed in this chapter.

The generalized fluid method proposed by Russell et al. (2003) based on the Biot-Gassmann theory will also be discussed in this chapter. This chapter will demonstrate how Russell et al. (2003) reformulated the Gassmann equation in fluid term (f) and dry skeleton term (s), which gives us a new insight into the fluid contribution to the bulk modulus and P-wave velocity, and further, reformulated the linearized AVO approximations in terms of f , m , and r , which is called *f-m-r* (fluid-mu-rho) method.

3.2 Biot-Gassmann theory

The objective of the Gassmann equation is to model the effect of fluid saturation on the bulk modulus and further to estimate the seismic properties, such as P-wave and S-wave velocity and density for the saturated porous rock. At low frequency, seismic velocity for a porous rock in an isotropic media can be estimated using known saturated rock elastic modulus and density:

$$V_p = \sqrt{\frac{\lambda + 2\mu}{\rho}} = \sqrt{\frac{K + 4/3\mu}{\rho}} \text{ , and} \tag{3.1}$$

$$V_s = \sqrt{\frac{\mu}{\rho}}, \tag{3.2}$$

where V_p and V_s are P-wave and S-wave velocities, K is bulk modulus, μ is shear modulus, λ is the first Lamé parameter, and ρ is density. From equation (3.1) the relationship between K and λ can be obtained as:

$$K = \lambda + 2/3\mu \,. \tag{3.3}$$

For a porous rock, when the pore fluid changes, the elastic modulii: K , μ , and λ for the saturated rock can be estimated using the Gassmann equation. Using the known bulk modulus and shear modulus, P-wave and S-wave velocities for the saturated rock can be estimated from equations (3.1) and (3.2).

3.2.1 Biot-Gassmann equation

Sedimentary rocks can be considered as porous aggregates of various minerals filled with a fluid mixture. When the seismic wave travels through the saturated porous rock, the rock frame will be deformed by the compression that arises from the seismic wave. The pore fluid is compressed and therefore stiffens the rock (Murphy et al., 1993). Gassmann equation has been routinely used to predict the stiffening effect of the fluid on the bulk modulus.

To facilitate understanding of the Gassmann equation, the saturated porous rock is usually simplified as the mixture of mineral and fluid. Not only the content of the mineral but also the texture of the mineral affects the porous rock's properties. Therefore, the porous rock can be divided into three components: pore fluid, rock matrix, and dry rock

frame. Figure 3.1 is the schematic diagram for the three components of the saturated porous rock.

The pore fluid is compromised of gas, water, and oil. The rock matrix is defined as the mixture of different minerals and the dry rock frame represents the skeleton of the rock without fluid filled in. (Russell et al, 2001).

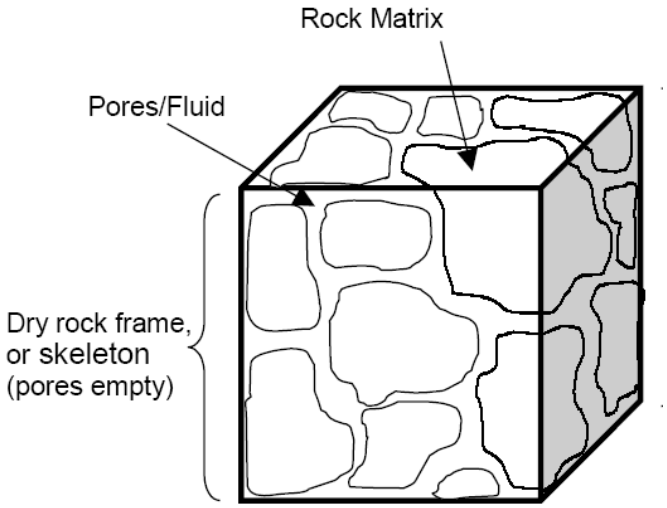

Figure 3.1 The schematic diagram for the porous saturated rock (Russell et al, 2001).

Gassmann equations formulate the bulk modulus of a saturated porous rock using the properties of pore fluid, rock matrix, and dry rock frame. According to the Gassmann theory (Gassmann, 1951), the bulk modulus and shear modulus for the saturated porous rock are defined as:

$$K_{sat} = K_{frame} + \frac{(1 - K_{frame}/K_{matrix})^2}{\frac{\phi}{K_{fluid}} + \frac{1-\phi}{K_{matrix}} - \frac{K_{frame}}{K_{matrix}^2}}, \text{ and} \quad (3.4)$$

$$\mu_{sat} = \mu_{dry}, \quad (3.5)$$

where, K_{sat}, K_{frame}, K_{matrix}, and K_{fluid} are the bulk modulus of the saturated rock, rock frame, rock matrix, and pore fluid respectively, μ_{sat} and μ_{dry} are the shear modulii of the saturated rock and dry rock. In the Gassmann formulation, shear modulus is independent of the pore fluid and remains unchanged during fluid substitution.

Usually, bulk modulus (K_{sat}) and shear modulus (μ_{sat}) at in-situ condition can be estimated from the seismic data or the wire line log data by rewriting equations (3.1) and equation (3.2) as:

$$K_{sat} = \rho(V_p^2 - 4/3V_s^2), \text{ and} \quad (3.6)$$

$$\mu_{sat} = \rho V_s^2. \quad (3.7)$$

K_{matrix} can be estimated from Voigt-Reuss-Hill (VRH) averaging method (Hill, 1952) when the mineral components have been determined. K_{fluid} can be estimated by inverse bulk modulus averaging (Wood's equation) and ρ_{sat} can be estimated by arithmetic averaging of densities of individual mineral.

3.2.2 Some assumptions for Biot-Gassmann theory

Since the Gassmann equation was derived from very complicated elastic wave theory for the fluid saturated elastic porous media, some assumptions were made to simplify the equation (Wang, 2001):

1) Gassmann theory assumes the porous rock is macroscopically homogeneous and isotropic for the matrix and rock frame, which implies that the seismic wavelength is

much longer than the grain and pore sizes (Wang, 2001). Therefore, in practice, the rock and mineral anisotropy is ignored.

2) Gassmann theory assumes all the pores are interconnected and there is perfect communication between the fluids in the pore space. That means the fluids can easily flow and relax these wave-induced pore pressure gradients during a seismic period (Wang, 2001). This assumption applies best to the low viscosity pore fluids and to the high porosity rocks with good pore space connectivity. This assumption will be violated for heavy oil, very high frequencies through ultrasonic measurements, high shale content, and low permeability (Mavko, 2005).

3) The pore fluid system is closed. This assumption is valid for most laboratory-measured systems. However, for some cases, the in-situ fluid may flow, which allows the seismic data only record the information caused by the rock matrix and skeleton (Wang, 2001).

4) The pore fluid does not interact with the solid to soften or harden the rock frame. In fact, the interaction between fluid and solid is inevitable and this assumption ignores the effects of chemical or physical interactions between the rock matrix and the pore fluid (Wang, 2001).

3.3 Generalized fluid method for impedances

Russell et al. (2003) proposed the generalized fluid method by using Biot-Gassmann theory. They reformulated the equation for P-wave velocity using a fluid term and skeleton term, which give more intuitive insight into the effect of pore fluid on the bulk modulus and P-wave velocity.

Under the low frequency assumption, the incompressibility and bulk modulus for the saturated porous sandstone can be expressed as the sum of the dry term and fluid term (Biot, 1941, and Gassmann, 1951):

$$\lambda_{sat} = \lambda_{dry} + \beta^2 M \text{ , and} \tag{3.8}$$

$$K_{sat} = K_{dry} + \beta^2 M \text{ ,} \tag{3.9}$$

where λ_{sat} and K_{sat} are the incompressibility and bulk modulus for the saturated rock, λ_{dry} and K_{dry} are the incompressibility and bulk modulus for the dry skeleton, β is the Biot coefficient, and M is Gassmann's pore space modulus.

In the above formulations, $\beta^2 M$ represents the contribution of the pore fluid. β measures the ratio of the volume change in the fluid to the volume change in the formation when hydraulic pressure is constant (Russell et al., 2003). It can also be equated to the terms used in Gassmann equation in the following way:

$$\beta = 1 - \frac{K_{dry}}{K_{matrix}}, \tag{3.10}$$

where K_{matrix} and K_{dry} is the bulk modulus of the matrix material and dry skeleton.

Gassmann's pore space modulus M is defined as the pressure needed to force water into the formation without changing the volume (Russell et al., 2003). It can also be related to the Gassmann parameters by:

$$\frac{1}{M} = \frac{\beta - \phi}{K_{matrix}} + \frac{\phi}{K_{fluid}} \text{ ,} \tag{3.11}$$

where K_{fluid} is the bulk modulus of the fluid, and ϕ is porosity.

Substituting equations (3.10) and equation (3.11) into equation (3.9), the equation will be formulated the same as the equation (3.4). Substituting the second term in equation (3.4)

with $\beta^2 M$, the equation for P-wave velocity for the saturated porous rock can be reformulated as:

$$V_p = \sqrt{\frac{\lambda_{dry} + 2\mu + \beta^2 M}{\rho_{sat}}} = \sqrt{\frac{K_{dry} + \frac{4}{3}\mu + \beta^2 M}{\rho_{sat}}} . \quad (3.12)$$

Russell et al. (2003) reformulated the equation (3.12) in terms of fluid term (f) and dry skeleton term (s) instead of λ , μ , and ρ , or K , μ , and ρ , which make it easier for us to understand which part come from fluid contribution and which part is associated with skeleton contribution:

$$V_p = \sqrt{\frac{s + f}{\rho_{sat}}} , \quad (3.13)$$

where f is a fluid term equal to $\beta^2 M$, and s is a dry skeleton term which can be formulated as $K_{dry}+(4/3)\mu$ or $\lambda_{dry}+2\mu$. Note that in equations (3.12) and (3.13), it is assumed that $\mu = \mu_{dry} = \mu_{sat}$.

Now, by having a fluid term and a skeleton term in the P-wave equation (3.13), the fluid term can be derived using P-wave and S-wave impedances. To extract the fluid term, the equations for P-wave and S-wave impedance can be reformulated as:

$$I_p = \rho V_p = \sqrt{\rho(f + s)} , \text{ and} \quad (3.14)$$

$$I_s = \rho V_s = \sqrt{\rho\mu} . \quad (3.15)$$

Using equation (3.14) and (3.15), the following function can be constructed:

$$I_p^2 - cI_s^2 = \rho(s + f - c\mu). \tag{3.16}$$

Russell et al. (2003) suggested that proper selection of c value could counteract the dry skeleton term in the equation (3.16) with only fluid term left in the right side of equation (3.16).

Letting

$$c = \frac{\lambda_{dry}}{\mu} + 2 = \frac{K_{dry}}{\mu} + \frac{4}{3} = \left(\frac{V_p}{V_s}\right)^2_{dry}, \tag{3.17}$$

the fluid term can be written as:

$$I_p^2 - cI_s^2 = \rho(s + f - c\mu) = \rho f. \tag{3.18}$$

Given the c value and P-wave and S-wave impedances, fluid term can be estimated.

When equation (3.18) is divided by $\rho\mu = I_s^2$, another fluid indicator will be obtained:

$$\frac{f}{\mu} = \left(\frac{V_p}{V_s}\right)^2_{sat} - \left(\frac{V_p}{V_s}\right)^2_{dry}. \tag{3.19}$$

Equation (3.17) shows that the constant c is defined by the terms of P-wave and S-wave velocities for dry rocks or the elastic modulus for the dry rock. For different reservoirs, the value of the constant c will vary with lithology, shale content, temperature, and consolidation. The value of c can be derived from the wellbore logs or rock samples for the local reservoir interval.

Is there any connection between the generalized fluid method and previous fluid method? Actually, the equation (3.18) can be reformulated as:

$$I_p^2 - cI_s^2 = (I_p + \sqrt{c}I_s)(I_p - \sqrt{c}I_s). \tag{3.20}$$

The difference term in the above equation is much more sensitive than the sum term to differentiate the fluid content. In fact, this difference term is very same as the fluid factor

ΔF proposed by Smith and Gidlow (1987). This also agrees with Dillon et al. (2003)'s observation that $I_p - I_s$ is a good discriminant for seismic data when $c = 1$.

The fluid term estimated from the generalized fluid method using $c = 2$ is equal to $\lambda\rho$ which can be derived from LMR method (Goodway et al., 1997). Although the fluid term $\lambda\rho$ can give good discrimination between hydrocarbon bearing porous sandstone and shale, it doesn't provide the pure fluid information in the way that the generalized fluid method does. There is still a contribution of the rock skeleton left in the fluid term: $\lambda\rho$. This can be explained by the fact that $\lambda\rho$ represents the change coming from the combination of fluid and rock skeleton.

The fluid term $I_p^{\,2} - 2.233 * I_s^{\,2}$ proposed by Hedlin (2000) is based on the assumption that $K_{dry} / \mu = 0.9$ (Murphy et al., 1993), which mean c is equal to 2.233. Hilterman (2001) used $I_p^{\,2} - 2.333 * I_s^{\,2}$ as the fluid indicator, which is based on the empirical relationship between K_{dry} and μ: $K_{dry} / \mu = 1$, which implies that $c = 2.333$.

So, the challenge for the generalized fluid method is the selection of c value. Theoretically, the generalized fluid method can provide the exact absolute fluid term based on the equation (3.18). However, the value of c varies horizontally and vertically for a specific reservoir, and depends on the variance of mineral mixture, porosity, clay content, and pressure in the reservoir. The best way is to find the background trend for the c value to derive the relative fluid term.

Based on the analysis of Murphy et al. (1993), the value of K_{dry} / μ is equal to 0.9, which correspondent to $c = 2.233$. Batzle et al. (2001) found that $K_{dry} / \mu = 1$ for the clastic

reservoir which means that $c = 2.333$. Russell et al. (2003) argued that $c = 2.333$ is more appropriate for the reservoir rocks such as consolidated sandstones. Dillon et al. (2003) calculated the c value using numerous measured rock samples. For young and more poorly consolidated samples, they concluded c should be around 3.1. For older and more consolidated materials, c drops to approximately 2.6.

To investigate how c affects the generalized fluid term $I_p^2 - c * I_s^2$, wet sandstone samples from Han's dataset (Han et al., 1986) were used to calculate attributes of $I_p^2 - cI_s^2$. Figure (3.2) is the plot of $I_p^2 - cI_s^2$ versus I_p using different c values. The attributes of $I_p^2 - cI_s^2$ using $c = \frac{K_{dry}}{\mu_{dry}} + \frac{4}{3} \approx 2.33$ are plotted in red stars and the trend line fitting these attributes is also drawn in red. The plot show that the red line representing $I_p^2 - 2.33I_s^2$ is almost perpendicular to the x axis which means $I_p^2 - 2.33I_s^2$ is orthogonal to y axis (I_p). For the blue trend line representing $I_p^2 - 2I_s^2$ and the black trend line representing $I_p^2 - 2.67I_s^2$, they deviate toward the left side and right side of the red line. Although they are not orthogonal to I_p, they still can provide a better clustering in $I_p^2 - cI_s^2$ direction. For the green and cyan trend lines, which correspondent to $I_p^2 - 1.33I_s^2$ and $I_p^2 - I_s^2$ respectively, they slope to the top right and the value range for $I_p^2 - cI_s^2$ become larger, which provide the worse clustering. A solution of $c = 2.233$ appears to be best suited with a vertical linear trend and will be used in the analysis of data in Chapter 5.

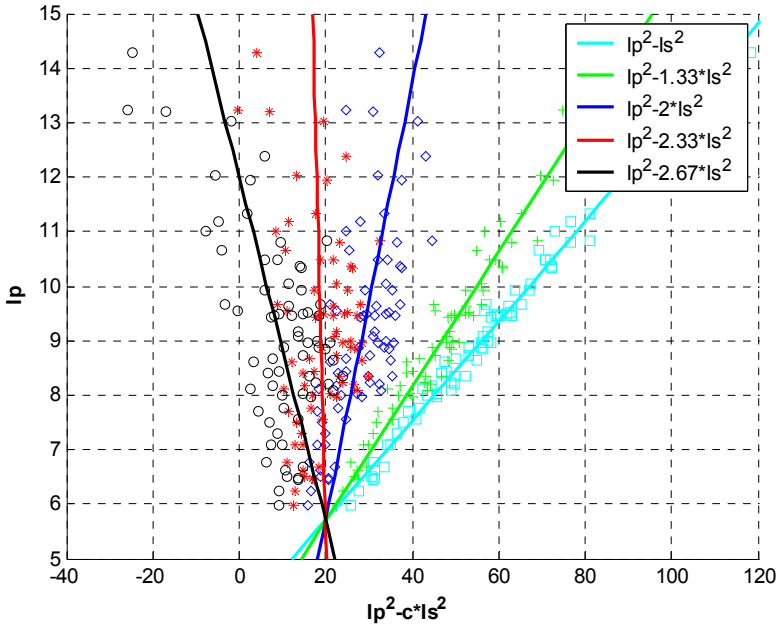

Figure 3.2 Plot of $I_p{}^2 - c * I_s{}^2$ versus I_p (P-wave impedance) using different c values.

3.4 Generalized fluid method for the linearized AVO

From the linearized approximations (Table 2.1 and Table 2.2) for Zoeppritz equation, Russell et al. (2006) found that they fall into two categories. One category involves with the parameters that are linearly related to V_p, V_s, ρ. Aki and Richard's equation emphasizes the contribution of variations in the P-wave and S-wave velocities and density. Shuey's approximation gives us the three extracted parameters that are called intercept, gradient, and curvature. Fatti et al.'s approximation can be used to estimate the P-wave and S-wave reflectivities and density reflectivity. These equations have been widely used to derive the reflectivity terms and further to estimate the acoustic impedance, shear impedance, and density (Russell et al., 2006).

Another option involves reformulating to the linearized approximations in terms of σ, λ, μ, and K, which are nonlinearly related to V_p, V_s, and ρ. Shuey (1982) transformed from V_s, and ΔV_s to Poisson's ratio σ, and $\Delta\sigma$. Gray et al. (1999) expressed the linearized approximation in terms of λ, μ, and ρ, and K, μ, and ρ.

Although λ and K can help to detect the fluid content, their values reflect the contributions from dry skeleton and pore fluid combined. Russell et al. (2006) suggested using f, μ, and ρ to generalize Gray's equations for fluid term extraction.

The fluid term (f) can be considered as the function of P-wave velocity, rigidity, and density. Russell et al. (2006) presented the differential form for the fluid term (f). For the detail derivation of the f term, please refer to the reference. The differential equation for the fluid term (f) can be written as:

$$\Delta f = \frac{\partial f}{\partial V_p}\Delta V_p + \frac{\partial f}{\partial \mu}\Delta\mu + \frac{\partial f}{\partial \rho}\Delta\rho . \tag{3.21}$$

Using equation (3.21), Russell et al. (2006) reformulate the Aki-Richards equation in terms of f, μ, and ρ:

$$R_{pp}(\theta) = a\frac{\Delta f}{f} + b\frac{\Delta\mu}{\mu} + c\frac{\Delta\rho}{\rho} . \tag{3.22}$$

where $a = (1/4 - \gamma^2_{dry}/4\gamma^2_{sat})\sec^2\theta$, $b = \gamma^2_{dry}/4\gamma^2_{sat}\sec^2\theta - 2/\gamma^2_{sat}\sin^2\theta$, $c = 1/2 - 1/4\sec^2\theta$, $\gamma^2_{sat} = (V_p/V_s)^2_{sat}$, and $\gamma^2_{dry} = (V_p/V_s)^2_{dry}$.

Russell et al. (2006) called equation (3.22) as the *f-m-r* (fluid-mu-rho) equation since it gives a new physical insight into the relationship between linearized AVO and rock properties. It is noticed that equation (3.22) is a generalization of the equations of Gray et

al. (1999). Russell et al. (2006) pointed out that the Gray et al. (1999) expression for λ, μ, and ρ is one case of equation (3.22) when $\gamma^2_{dry} = 2$ and the Gray et al. (1999) expression for K, μ, and ρ is one case of equation (3.22) when $\gamma^2_{dry} = 4/3$.

To extract the fluid term reflectivity, the constant values for γ^2_{dry} and γ^2_{sat} need to be known to build the coefficient matrix for least-squares solution.

CHAPTER FOUR: EMPIRICAL STUDY USING HAN'S DATASET

4.1 Introduction

This chapter investigates the effect of clay content, porosity, and pressure on $(Vp/Vs)^2_{dry}$ for the dry rock, which plays an important role in the generalized fluid method. The generalized fluid method proposed by Russell et al. (2003), gives us an alternative approach to discriminate the fluid content. However, the success of this method is subject to the correct estimation of $(Vp/Vs)^2_{dry}$, where V_p and V_s are the P-wave and S-wave velocities for the dry rock.

Actually, the $(V_p/V_s)^2{}_{dry}$ value varies a lot for different reservoirs with varying lithologies, clay content, porosity, and pressure. Based on the study of the well log examples from the White Rose area of offshore eastern Canada, Russell et al. (2003) concluded that the average $(V_p/V_s)^2{}_{dry}$ value should be 2.333, which implies that $K_{dry}/\mu_{dry}=1$ and Poisson's ratio is 0.125. Murphy et al. (1993) measured the K_{dry}/μ_{dry} value for clean quartz sandstones over a wide range of porosities and found that this value was approximately 0.9, which corresponds to $(V_p/V_s)^2{}_{dry}=2.233$. Batzle et al. (2001) found that the K_{dry}/μ_{dry} value is close to 1.0, which implies $\sigma_{dry}=0.125$ and a corresponding $(V_p/V_s)^2{}_{dry}$ value of 2.333.

Dillon et al. (2003) applied the generalized fluid method to Tertiary and Cretaceous siliciclastic reservoirs of Brazilian offshore fields and conducted the $(V_p/V_s)^2{}_{dry}$ analyses based on lab measurements under real subsurface reservoir conditions. These

studies demonstrated that the optimal value for $(V_p / V_s)^2_{dry}$ is 3.00 for the Tertiary reservoir, 2.6 for the Cretaceous reservoir, and an average of 2.9 for both reservoirs. Rojas et al. (2006) analyzed the laboratory measurements of 301 core samples with different lithologies, clay content, porosities, and pressures. They found that $(V_p / V_s)^2_{dry}$ would increase with porosity and decrease with clay content. The resulting investigation showed that $(V_p / V_s)^2_{dry}$ varies between 2 and 2.9 for sandstones and between 2.5 and 3.5 for carbonates.

Although there are many other theoretical models to study the effect of porosity, pore shape, and fluid on the elastic properties of rocks, their effects on dry P-wave, S-wave velocities, and the values of $(V_p / V_s)^2_{dry}$ are still not clear as most of the studies were limited to the saturated case. In this chapter, the effect of clays, porosity, and pressure on the value of $(V_p / V_s)^2_{dry}$ will be investigated based on Han's laboratory measurements.

4.2 Sample description

The sandstone samples used in this study were found in Han's papers (Han et al., 1986) and are referred to as Han's dataset. These rock samples exhibit varying porosity ranging from 0.02 to 0.3 and varying clay content from 0 to 0.5. Some rock samples are poorly consolidated and some are well consolidated. Ten rock samples are clean sandstones with less than one percent clay content and the others are shaly sandstones. P-wave and S-wave velocities used in this study are measured at dry condition at different differential pressures. Figure 4.1 shows the clay content versus porosity for all samples.

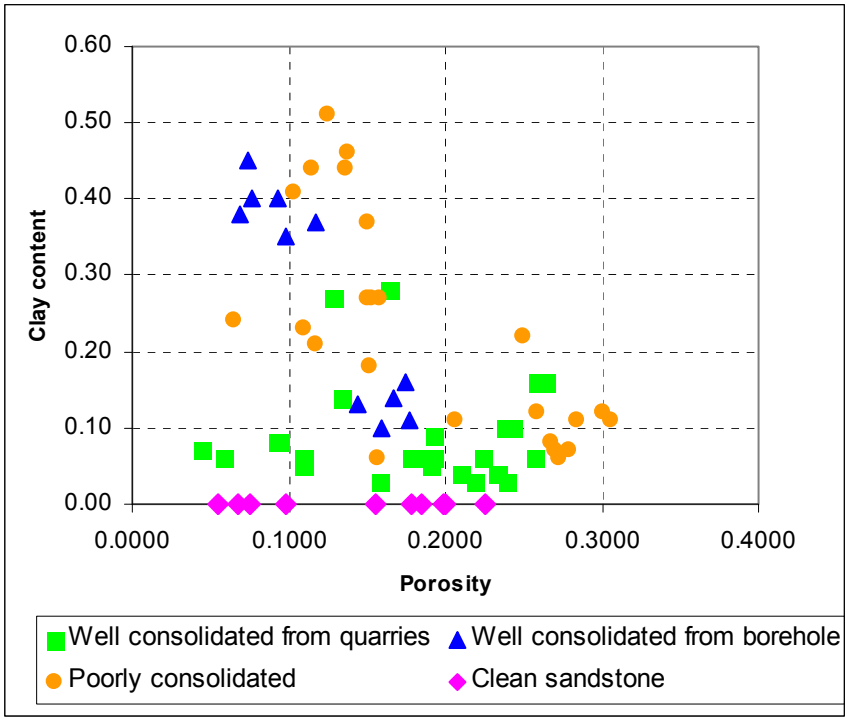

Figure 4.1 The ranges of clay content and porosity for 75 shaly sandstones of this study. Porosity ranges from 2 to 30 percent, and clay content ranges from 0 to about 50 percent (Han et al., 1986).

4.3 Clean sandstones

The effects of porosity on velocities and *Vp/Vs* ratio

Although there are only ten samples for the clean sandstones, the obvious trend can be observed from a plot of V_p versus porosity, V_s versus porosity, and V_p / V_s versus porosity (Figure 4.2 to Figure 4.4). These plots indicate that both V_p and V_s decrease with increasing porosity, whereas V_p / V_s increase with increasing porosity.

To model the relationship between porosity and velocity, an empirical linear model $V = a + b * \phi$ was used to fit V_p, V_s, and V_p / V_s data, where a and b are constant factors and ϕ is porosity.

The following best fits to the data at the differential pressure 5 MPa are obtained by least-square regression. For the P-wave velocity,

$$V_p = 5.64 - 8.67 * \phi, \tag{4.1}$$

for the S-wave velocity,

$$V_s = 3.83 - 6.43 * \phi, \tag{4.2}$$

and for V_p / V_s ratio,

$$V_p / V_s = 1.46 + 0.37 * \phi. \tag{4.3}$$

From the coefficients of the empirical expression for P-wave velocity and S-wave velocity, it can be concluded that the influence of porosity on P-wave velocity should be higher than that on shear velocity. The V_p / V_s ratio increases with porosity owing to that S-wave velocity drops faster than P-wave velocity does when porosity goes up.

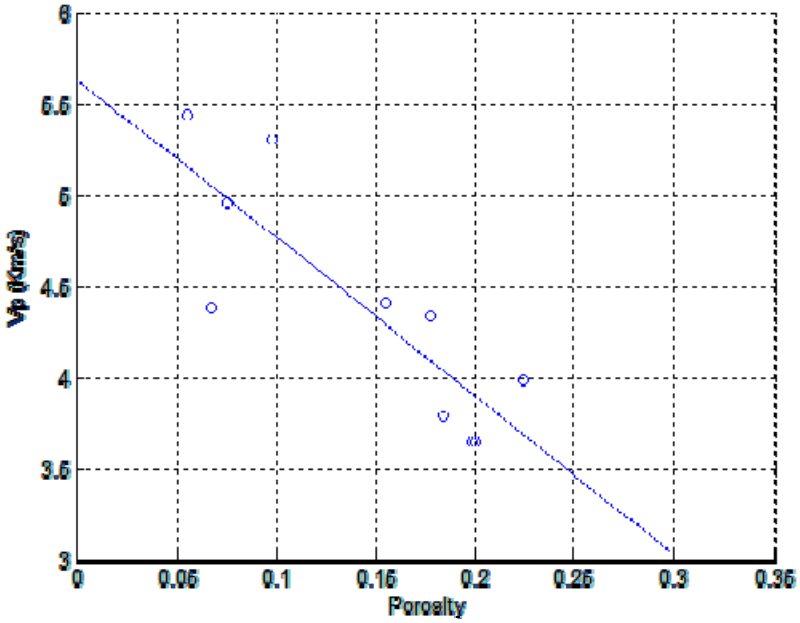

Figure 4.2 Measured P-wave velocity versus porosity for 10 clean sandstones at Pe = 5 MPa (Han et al., 1986).

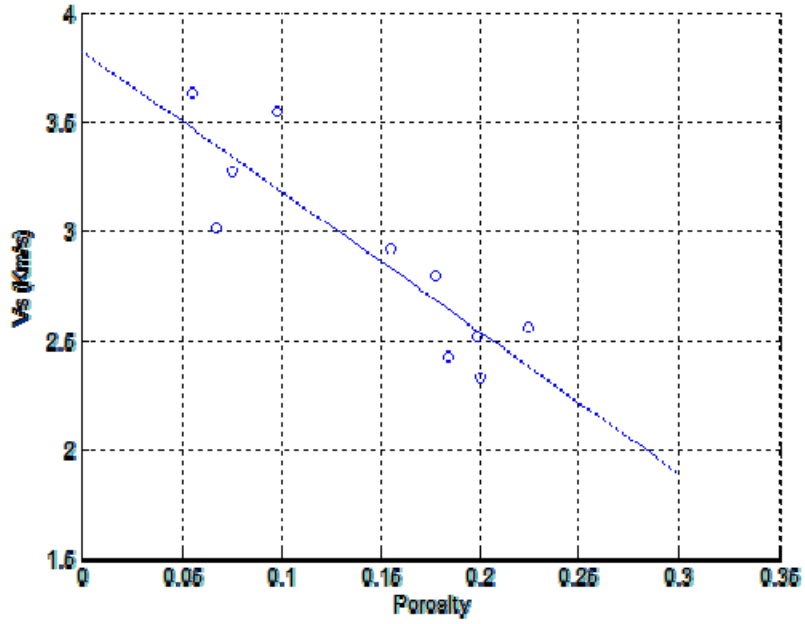

Figure 4.3 Measured S-wave velocity versus porosity for 10 clean sandstones at Pe = 5 MPa (Han et al., 1986).

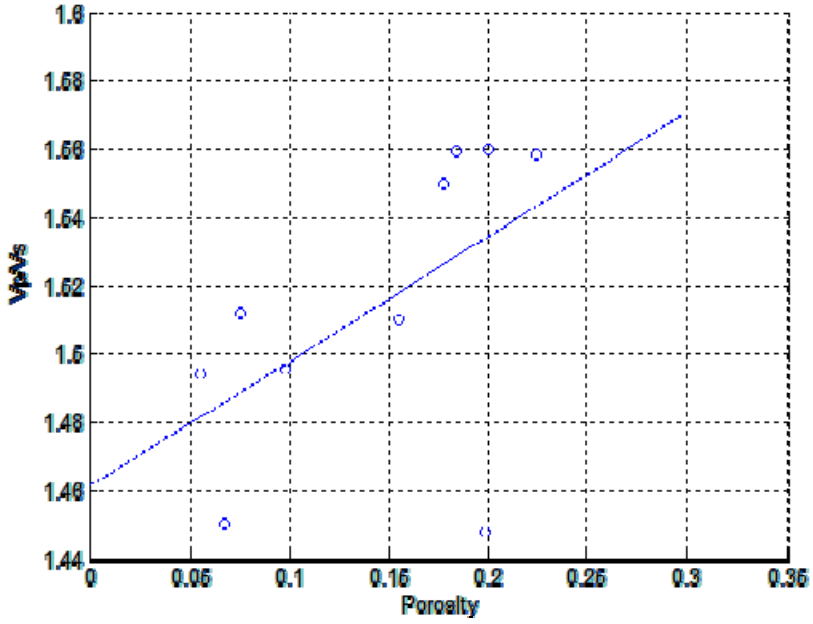

Figure 4.4 Plot of V_p / V_s ratio versus porosity for 10 clean sandstones at Pe = 5 MPa (Han et al., 1986).

4.4 Shaly sandstones

The effects of porosity and clay content on velocities

Plots of P-wave velocity (V_p) versus porosity, S-wave velocity (V_s) versus porosity ϕ plots for all of the shaly sandstone samples are shown in Figures 4.5 and 4.6. Despite some scatters, clear trends indicate that both V_p and V_s decrease with increasing porosity and clay content.

Considering the effects of porosity and clay content on the P-wave and S-wave velocity, the empirical linear model $V = a + b * \phi + c * Clay$ was used to fit both P-wave velocity and S-wave velocity, where a, b, and c are constant factors, ϕ is porosity and $Clay$ is clay content. The following best fits to the data at the differential pressure 5 MPa are obtained by least-square regression. For the P-wave velocity,

$$V_p = 4.73 - 6.43 * \phi - 2.67 * Clay, \tag{4.4}$$

and for the shear velocity,

$$V_s = 3.23 - 4.86 * \phi - 1.65 * Clay \cdot \tag{4.5}$$

Figure 4.5 and 4.6 show that P-wave velocity and S-wave velocities have an obvious inverse correlation with porosity and clay content except for some shaly sandstones. From equation (4.4) it is noticed that when $Clay = 0$, the equation should be for clean sandstones. However this equation is different from the equation (4. 1) for clean sandstones. This distinct difference between the empirical equations for the clean and shaly sandstones implies that even small amounts of clay can have significant influence on the velocities. Mavko et al. (1998) explained the effect of clay on the velocity. Theoretically, clay in sandstones tends to soften grain contacts significantly. This kind of

softening is most likely associated with the clay type and texture of clay particles between matrix grain boundaries. In the case that clay is present in the rock, even a small amount of clay will cover the entire pore surface and matrix grain contact, which will soften the grain contact (Mavko et al., 1998). It can be concluded that the clay adherent on the contact is responsible for the decrease of velocity from clean sandstones to shaly sandstones.

Secondly, it is hard to understand why some clusters of points with high clay content deviated from the fitted lines so much. This phenomenon suggests that the P-wave and S-wave velocities may be dependent of the texture of the clay and the way of the clay particles embedded in the rock matrix.

Finally, the coefficients in equation (4.4) indicate that the influence of porosity on V_p is much more than that of clay on V_p. Equation (4.5) exhibits the same phenomena for V_s.

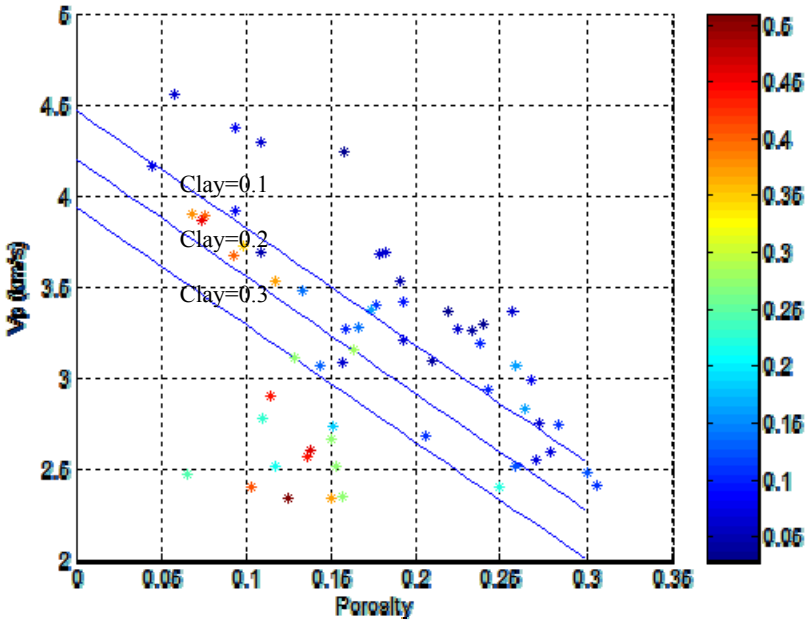

Figure 4.5 Measured P-wave velocity versus porosity color-coded with clay content for shaly sandstones at Pe = 5 MPa (Han et al., 1986).

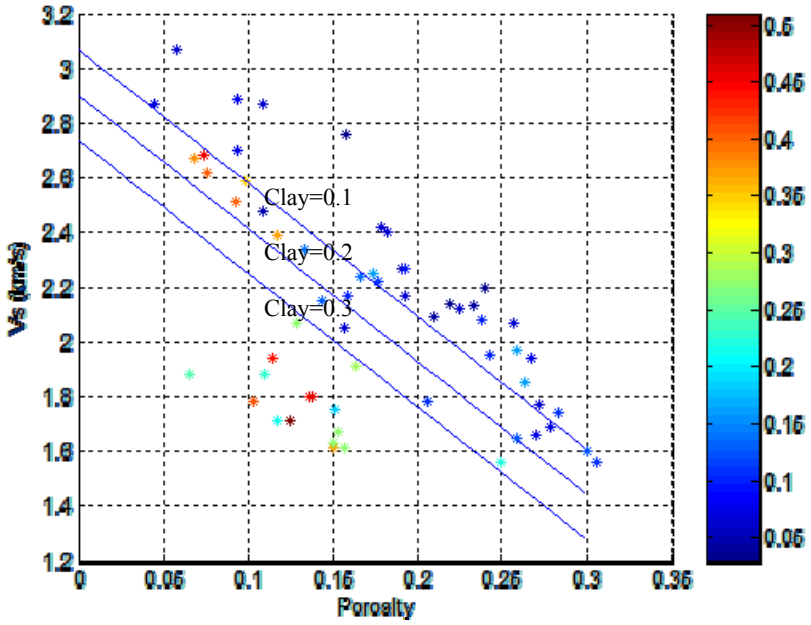

Figure 4.6 Measured S-wave velocity versus porosity color-coded with clay content for shaly sandstones at Pe = 5 MPa (Han et al., 1986).

The effects of porosity and clay content on dry *Vp/Vs* ratio

The value of V_p / V_s ratio provides significant insight into petrophysical properties, including lithology, porosity, pore structure, pore fluid, and other factors (Wang et al., 1997, Tatham, 1991). Previous laboratory studies have suggested correlations between lithology, porosity, and V_p / V_s ratio values. However their studies are mainly limited to the saturated cases and the behaviour of V_p / V_s ratio for the dry condition is different from the saturated condition.

Han's dataset shows that the velocity ratio for dry shaly sandstones depends upon both porosity and clay content. By least-square regression, this dependence is found to be:

$$V_p / V_s = 1.44 + 0.42 * \phi - 0.10 * Clay \cdot \tag{4.6}$$

where ϕ is porosity and $Clay$ is clay content.

Although the V_p/V_s ratio exhibits a wide range of values from 1.3 to 1.65, the results show that V_p/V_s increases with porosity and decreases with clay content (Figure 4.7) and that V_p/V_s is more sensitive to porosity changes. That means V_p/V_s will be higher for unconsolidated sandstones and lower for well-consolidated sandstones.

It should be noticed that V_p/V_s under dry condition for shaly sandstones is different from that under the saturated condition. The V_p/V_s ratio under the saturated conditions increases with clay content (Han et al. 1986). However, V_p/V_s under dry conditions have an inverse correlation with clay content (Figure 4.7), and also, V_p/V_s ratio behaves differently for different rock types. The V_p/V_s ratio for dry carbonate decreases with increasing porosity while it increases with increasing porosity for sandstones (Han et al. 2003).

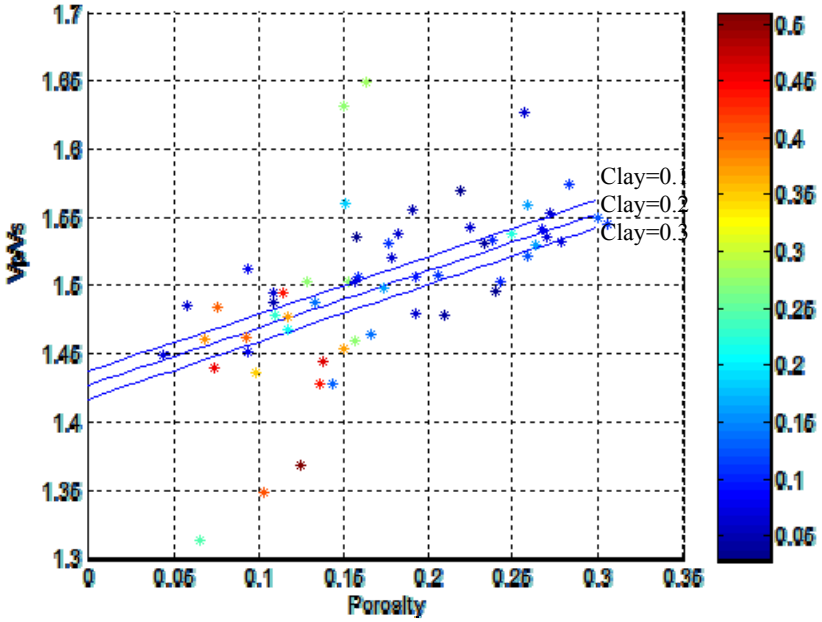

Figure 4.7 Plot of V_p/V_s versus porosity color-coded with clay content for shaly sandstones at Pe = 5 MPa (Han et al., 1986).

4.5 The effects of pressure on *Vp, Vs* and *Vp/Vs* ratio

P-wave and S-wave velocities and V_p / V_s ratio for the saturated rock have been widely studied while fewer studies have been conducted on the dry rock case. For the saturated rock, V_p / V_s ratio decreases with increasing differential pressure (Han et al., 1986). However, dry rocks exhibit the opposite effect. Nur (1969) and Toksoz et al. (1976) were probably the first authors to record the increase of V_p / V_s with increasing differential pressure in room-dry granite and dolomite samples. Recently, Vanorio et al. (2006) also found that V_p / V_s ratio increases with the differential pressure.

Table 4.1 and Table 4.2 show empirical expressions for P-wave velocity, S-wave velocity, and V_p / V_s ratio for dry shaly sandstones and dry clean sandstones. Let us analyze these results.

First, note that Figure 4.8 indicates that P-wave velocity and S-wave velocity for dry shaly sandstones increases with increasing differential pressure. Clean sandstones exhibit a similar effect as shown in Figure 4.10. The observed effect of differential pressure on P-wave velocity and S-wave velocity can be explained through the following mechanism: increasing or decreasing of the differential pressure will stiffen or soften the rock, therefore, making the grain contacts close or open, which ends up increasing or decreasing of the velocity.

Second, the coefficients for the clay content term and porosity term are very close for different pressures (Table 4.1 and Table 4.2). These results suggest that the effects of porosity and clay content on the velocities are fairly independent of differential pressure.

Third, P-wave and S-wave velocities and V_p / V_s ratio for the shaly sandstones change faster at lower differential pressure than they do at higher differential pressure (Figure 4.8 and Figure 4.9). For dry clean sandstones, P-wave and S-wave velocities exhibit the similar behavior as those for shaly sandstones whereas V_p / V_s ratio keeps fairly constant with differential pressure (Figure 4.10 and Figure 4.11).

Lastly, the average value for V_p / V_s is around 1.55 for shaly sandstones and 1.52 for clean sandstones (Figure 4.9 and Figure 4.11).

Table 4.1 Pressure dependence on V_p, V_s, and V_p / V_s ratio for shaly sandstones (Han et al., 1986).

Pressure	***Vp***	***Vs***	***Vp/Vs***
5 Mpa	4.73-6.43*Φ-2.67*C	3.23-4.86*Φ-1.65*C	1.44+0.42* Φ -0.10*C
10 Mpa	4.93-6.14*Φ-2.73*C	3.32-4.57*Φ-1.72*C	1.47+0.36* Φ -0.05*C
20 Mpa	5.17-6.17*Φ-2.81*C	3.44-4.50*Φ-1.77*C	1.49+0.31* Φ -0.03*C
30 Mpa	5.31-6.26*Φ-2.87*C	3.51-4.54*Φ-1.81*C	1.50+0.31* Φ -0.03*C
40 Mpa	5.40-6.36*Φ-2.90*C	3.56-4.59*Φ-1.84*C	1.51+0.29* Φ -0.02*C
50 Mpa	5.46-6.44*Φ-2.93*C	3.60-4.62*Φ-1.86*C	1.51+0.29* Φ -0.02*C

Table 4.2 Pressure dependence on V_p, V_s, and V_p / V_s ratio for clean sandstones (Han et al., 1986).

Pressure	***Vp***	***Vs***	***Vp/Vs***
5 Mpa	5.64-8.67*Φ	3.83-6.43*Φ	1.46+0.36* Φ
10 Mpa	5.71-7.79*Φ	3.88-5.83*Φ	1.47+0.34* Φ
20 Mpa	5.83-7.67*Φ	3.94-5.66*Φ	1.48+0.28* Φ
30 Mpa	5.90-7.68*Φ	3.99-5.73*Φ	1.47+0.31* Φ
40 Mpa	5.97-7.84*Φ	4.03-5.84*Φ	1.47+0.31* Φ
50 Mpa	6.01-7.95*Φ	4.06-5.90*Φ	1.47+0.31* Φ

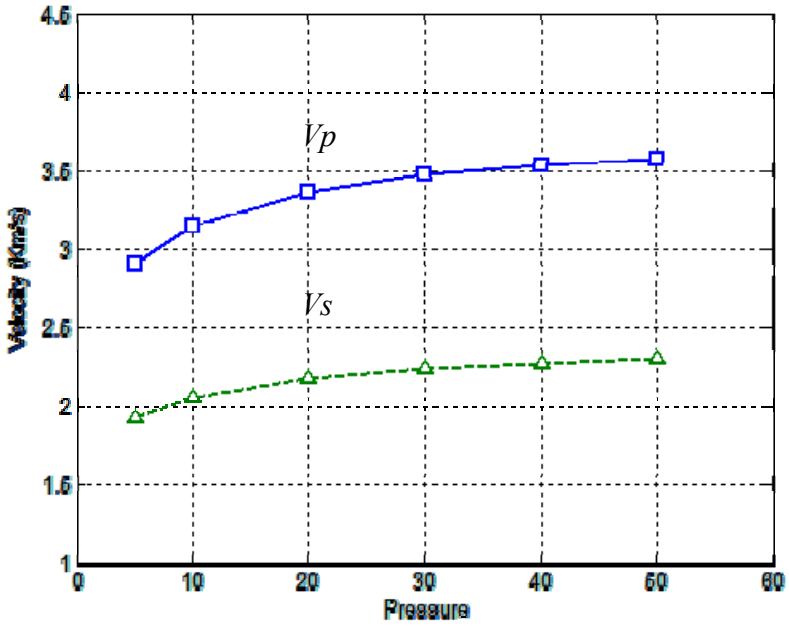

Figure 4.8 Plot of V_p and V_s versus pressure for shaly sandstone samples using an empirical relation when porosity =0.2 and clay content =0.2 (Han et al., 1986).

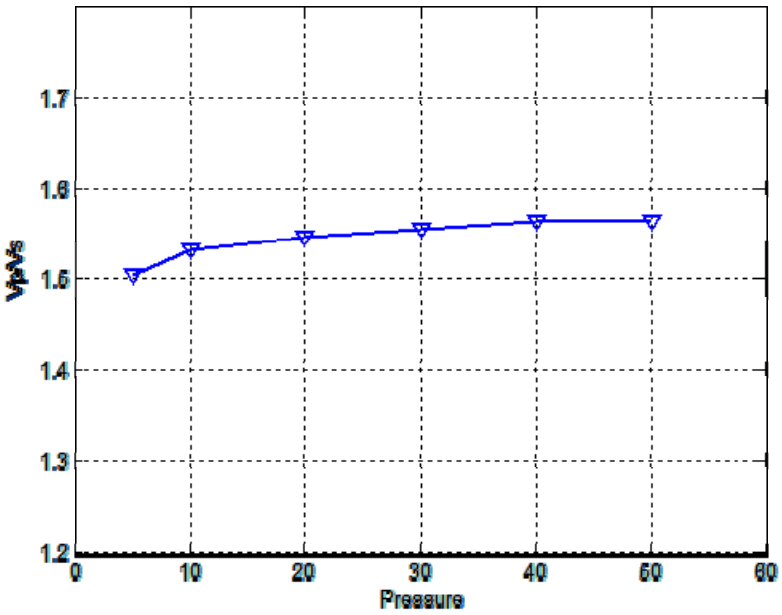

Figure 4.9 Plot of V_p / V_s versus pressure for shaly sandstones using an empirical relation when porosity =0.2 and clay content =0.2 (Han et al., 1986).

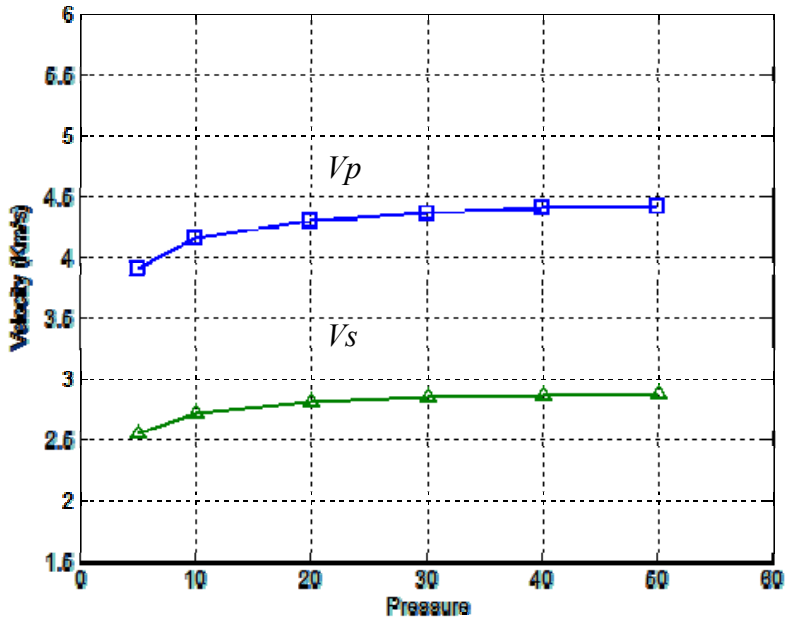

Figure 4.10 Plot of V_p and V_s versus pressure for clean sandstones using an empirical relation when porosity =0.2 (Han et al., 1986).

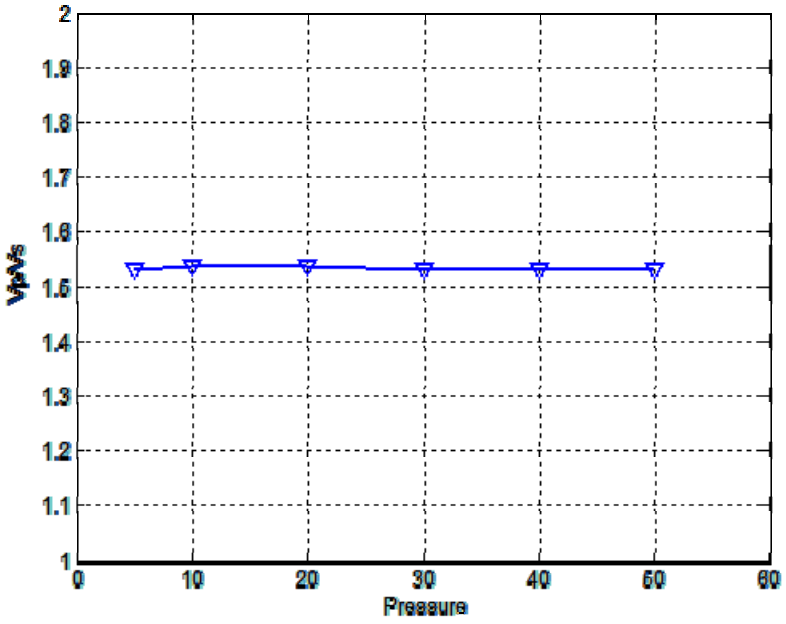

Figure 4.11 Plot of V_p / V_s ratio versus pressure for clean sandstones using an empirical relation when porosity =0.2 (Han et al., 1986).

Table 4.3 Effects clay content (shale), porosity, and pressure on V_p, V_s, and V_p / V_s ratio (Han et al., 1986).

	Vp	***Vs***	***Vp/Vs***
Shale ↑	↓	↓	↓
Porosity ↑	↓	↓	↑
Pressure ↑	↑	↑	↑

4.6 Summary

Table 4.3 summarized the effects of porosity, clay content, and pressure on the V_p, V_s, and V_p / V_s ratio. Based on the laboratory measurements, it can be concluded that:

1. For dry shaly sandstones, P-wave velocity (V_p) and S-wave velocity (V_s) show an inverse correlation with porosity and clay content. Clean sandstones exhibit a similar effect.
2. A small amount of clay can significantly soften the sandstone matrix, which leads to reducing velocities and the P-wave velocity (V_p) drops faster than S-wave velocity does, which end up with the decreasing of V_p / V_s ratio.
3. From the coefficients for the porosity term and clay content term in the empirical expression for V_p and V_s, the effect of porosity is larger than that of clay content.
4. V_p / V_s ratio for dry sandstones increases with porosity and decreases with clay content (Figure 4.12 and Figure 4.13). For the dry shaly sandstones, V_p / V_s ratio increases with increasing differential pressure. However, V_p / V_s ratio stays constant with different differential pressures for the clean sandstones.
5. Histograms of V_p / V_s ratio at different differential pressures show that V_p / V_s ratio increases with differential pressure and standard deviation of V_p / V_s ratio decreases with differential pressure (Figure 4.14).
6. The average value of V_p / V_s ratio for dry clean sandstones is approximately 1.52 and 1.55 for dry shaly sandstones.

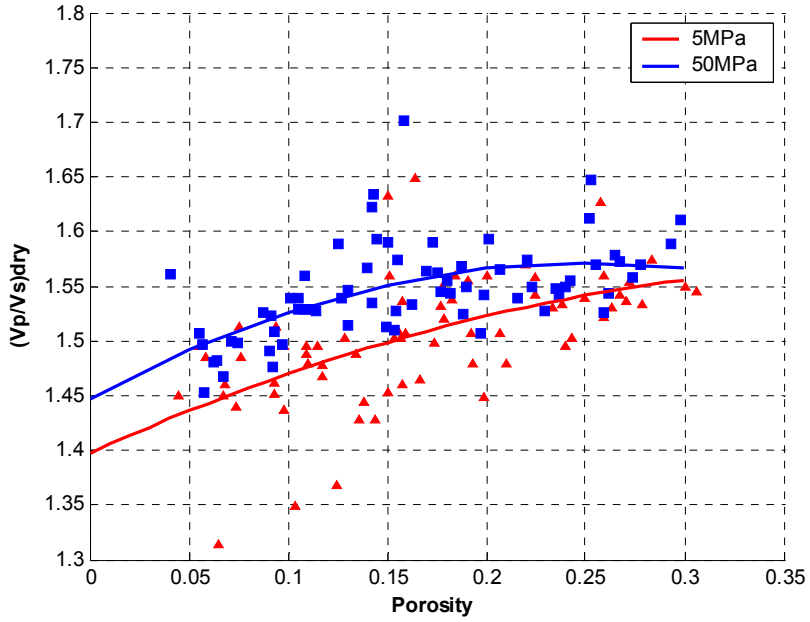

Figure 4.12 Correlation between V_p / V_s ratio and porosity for the whole dataset at Pe = 5 MPa and 50MPa (Han et al., 1986).

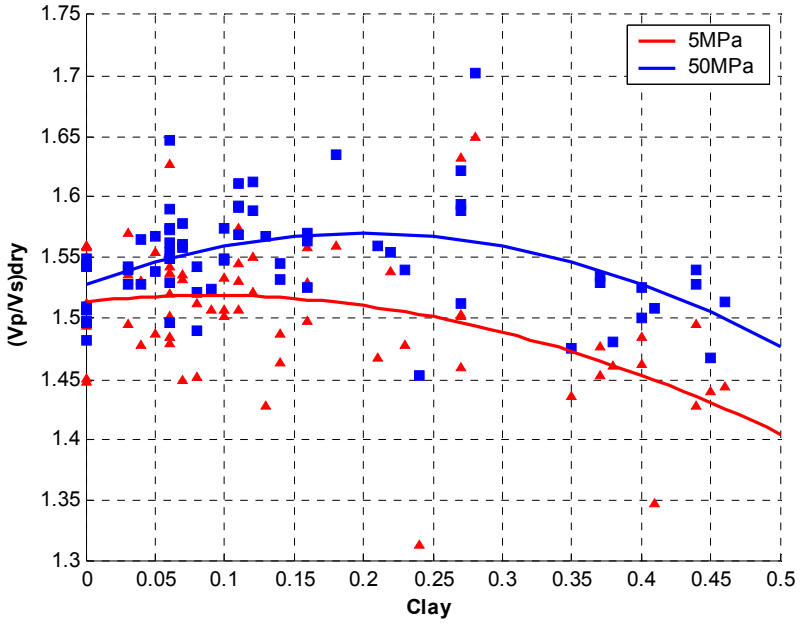

Figure 4.13 Correlation between V_p / V_s ratio and clay content for the whole dataset at Pe = 5 MPa and 50MPa (Han et al., 1986).

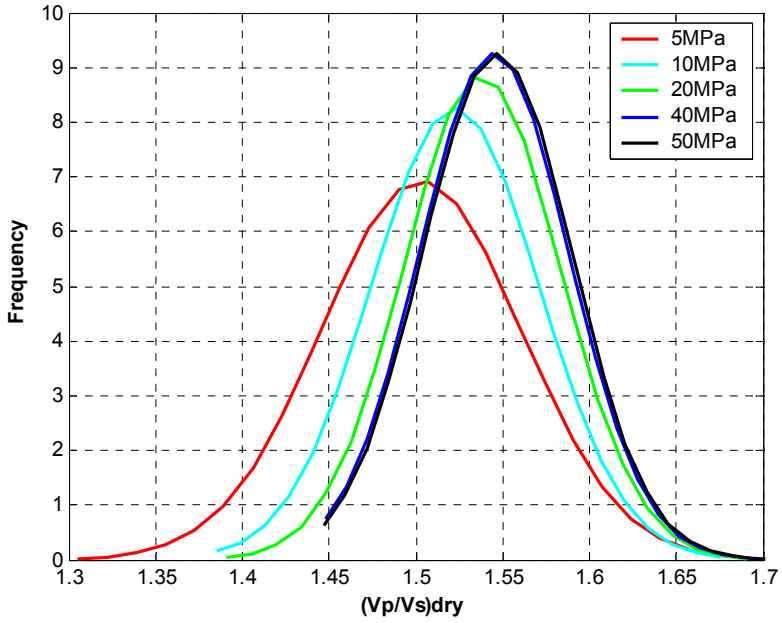

Figure 4.14 V_p / V_s ratio histograms for 5 MPa, 10 MPa, 20 MPa, 30 MPa, 40 MPa, and 50 MPa pressure. Note that V_p / V_s ratio increases with differential pressure (Han et al., 1986).

CHAPTER FIVE: SENSITIVITY ANALYSIS FOR FLUID INDICATORS

5.1 Introduction

Various approaches have been published to derive fluid indicators to infer the hydrocarbon content in a reservoir. The basic objective of these methods is to use the linearized Zoeppritz equations to extract petrophysical parameters, such as P-wave and S-wave impedances, P-wave and S-wave velocities, Poisson's ratio, etc., and also to derive more interpretable parameters such as the elastic modulii, Lamé's parameters, and other fluid indicators to detect the fluid content and lithology. Usually, these indicators provide a good method to quickly identify hydrocarbon zones. Some fluid indicators work well in some specific reservoirs, but don't work in other reservoirs. Therefore, there is probably no one best fluid indicator.

The objectives of this chapter are to examine which indicator can most easily discriminate gas or oil sandstones from wet sandstones or shale background and which indicator is most sensitive to the pore-fluid content.

In this chapter, the numerical examples of class I, II, and III sand models given by Hilterman (2001) are used to model the discrimination ability of these fluid indicators at given reservoir conditions and to analyze the sensitivity of each fluid indicator to the fluid content. Han's dataset measured for the wet case and dry case at different differential pressures is used to find which fluid indicator is most sensitive to the fluid content. The dataset is also used to diagnose the effect of c value to the performance of the discrimination of the generalized fluid term proposed by Russell et al. (2003).

5.2 Analysis using Class I, II, and III sand models

Hilterman's (2001) Class I, II, and III sand models derived from the Gulf of Mexico are a standard dataset for AVO analysis. The following thirteen indicators: V_p / V_s, Ip, Is, $\mu\rho$, $\lambda\rho$, K, μ, λ, λ / μ, Poisson's ratio (σ), $K - \mu$, $Ip^2 - c * Is^2$, and Fluid factor (ΔF) were derived for sensitivity analysis. The c term in the $Ip^2 - c * Is^2$ fluid indicator was derived based on the assumption that porosity is 20 % and saturation is 20 %.

The fluid indicator coefficient (Dillon et al., 2003) was used to diagnose the sensitivity to the fluid discrimination. In this data analysis it is defined as the difference between shale and wet sand or shale and gas sand divided by the value related to the shale as reference. A higher value represents better discrimination.

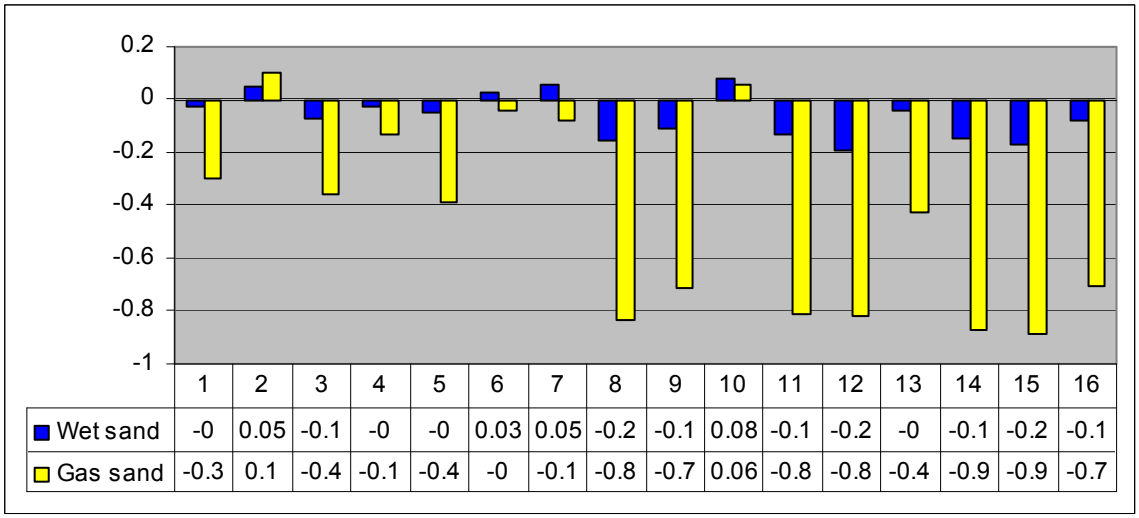

	1	2	3	4	5	6	7	8	9	10	11	12	13	14	15	16
Wet sand	-0	0.05	-0.1	-0	-0	0.03	0.05	-0.2	-0.1	0.08	-0.1	-0.2	-0	-0.1	-0.2	-0.1
Gas sand	-0.3	0.1	-0.4	-0.1	-0.4	-0	-0.1	-0.8	-0.7	0.06	-0.8	-0.8	-0.4	-0.9	-0.9	-0.7

Figure 5.1 Calculated fluid indicators for Class III sand model (4000 ft depth). 1. V_p, 2. V_s, 3. (V_p / V_s), 4. ρ, 5. Ip, 6. Is, 7. $\mu\rho$, 8. $\lambda\rho$, 9. K, 10. μ, 11. λ, 12. λ / μ, 13. Poisson's ratio (σ), 14. $K - \mu$, 15. $Ip^2 - c * Is^2$, 16. Fluid factor (ΔF). Observe that the fluid indicators, $Ip^2 - c * Is^2$, $\lambda\rho$, K, λ, λ / μ, $K - \mu$, and Fluid factor (ΔF) are more effective for both the wet sand and the gas sand. Also there is good separation between the wet sand and the gas sand.

From Figures 5.1 to Figure 5.3, it can be observed that the fluid indicators, $Ip^2 - c * Is^2$, $\lambda\rho$, $K - \mu$, λ, and λ / μ are more effective for both the wet sand and gas sand. In addition, there is a good separation between the wet and gas sand. However, for Class II and Class I sand, the fluid indicator coefficient decreases and the difference between the wet and the gas sand decreases, which makes it very difficult to separate the gas sand from the wet sand. That means it is very easy to discriminate the gas sand from the wet sand for the Class III gas sand. Usually, the Class III gas sand is at a shallow depth with high porosity and therefore has high impedance contrast (high negative intercept). When the depth is deeper, the gas sand will become more consolidated with less porosity and therefore has a weaker impedance contrast (either zero intercept or slightly positive intercept).

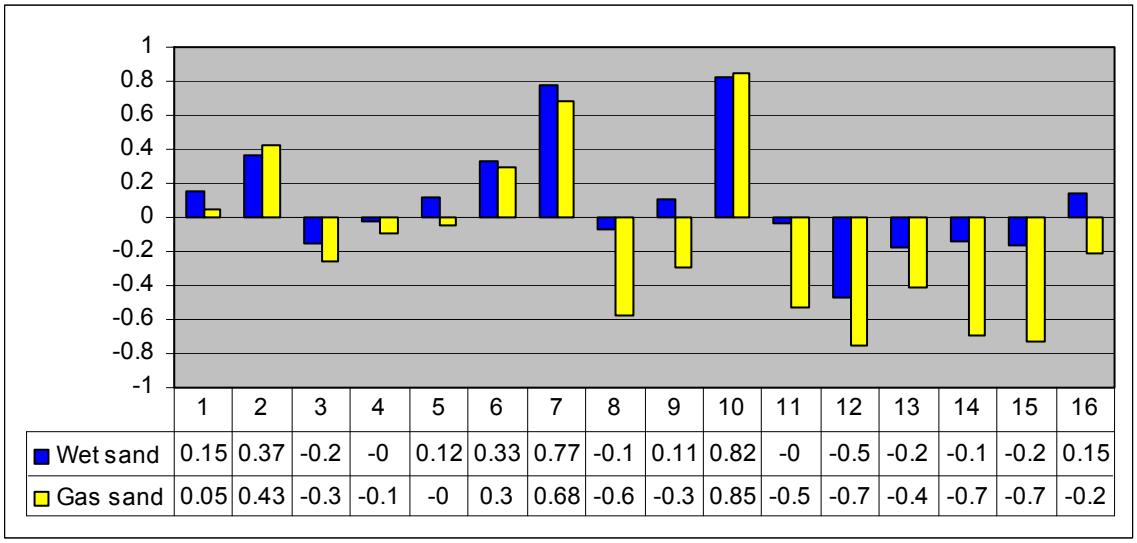

	1	2	3	4	5	6	7	8	9	10	11	12	13	14	15	16
Wet sand	0.15	0.37	-0.2	-0	0.12	0.33	0.77	-0.1	0.11	0.82	-0	-0.5	-0.2	-0.1	-0.2	0.15
Gas sand	0.05	0.43	-0.3	-0.1	-0	0.3	0.68	-0.6	-0.3	0.85	-0.5	-0.7	-0.4	-0.7	-0.7	-0.2

Figure 5.2 Calculated fluid indicators for Class II sand model (9000-ft depth). 1. V_p, 2. V_s, 3. (V_p / V_s), 4. ρ, 5. Ip, 6. Is, 7. $\mu\rho$, 8. $\lambda\rho$, 9. K, 10. μ, 11. λ, 12. λ / μ, 13. Poisson's ratio (σ), 14. $K - \mu$, 15. $Ip^2 - c * Is^2$, 16. Fluid factor (ΔF). Notice that $Ip^2 - c * Is^2$, $\lambda\rho$, K, λ, λ / μ, $K - \mu$, and Fluid factor (ΔF) are still more effective than other indicators.

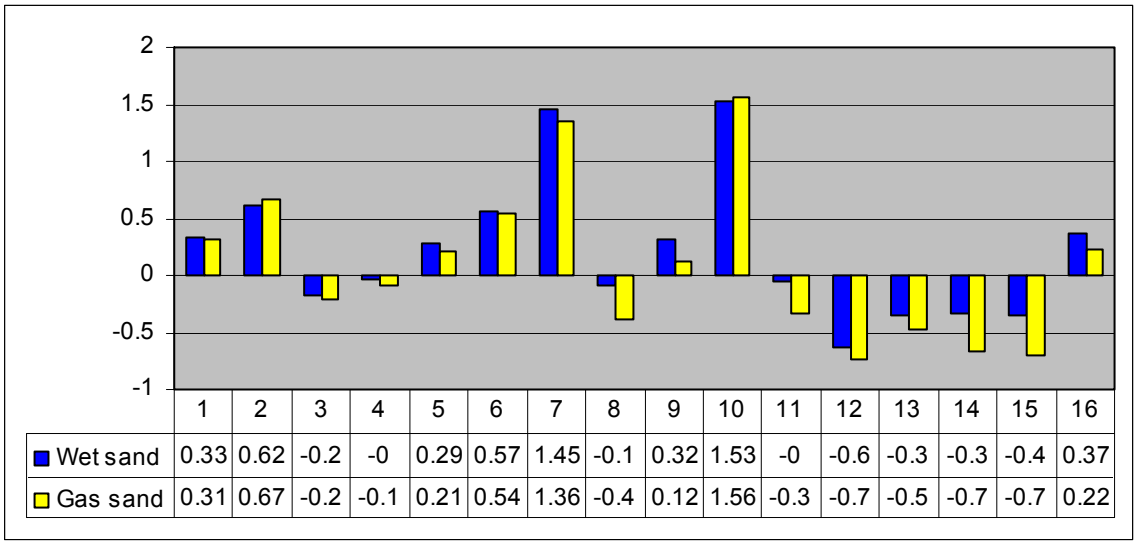

	1	2	3	4	5	6	7	8	9	10	11	12	13	14	15	16
Wet sand	0.33	0.62	-0.2	-0	0.29	0.57	1.45	-0.1	0.32	1.53	-0	-0.6	-0.3	-0.3	-0.4	0.37
Gas sand	0.31	0.67	-0.2	-0.1	0.21	0.54	1.36	-0.4	0.12	1.56	-0.3	-0.7	-0.5	-0.7	-0.7	0.22

Figure 5.3 Calculated fluid indicators for Class I sand model (14000-ft depth). 1. V_p, 2. V_s, 3. (V_p/V_s), 4. ρ, 5. Ip, 6. Is, 7. $\mu\rho$, 8. $\lambda\rho$, 9. K, 10. μ, 11. λ, 12. λ/μ, 13. Poisson's ratio (σ), 14. $K-\mu$, 15. $Ip^2 - c*Is^2$, 16. Fluid factor (ΔF). Notice that $Ip^2 - c*Is^2$, $\lambda\rho$, and λ are still more effective than other indicators. However the absolute value of the fluid indicator coefficient for them decreases compared with Class I and Class II sand model and the difference between the wet sand and the gas sand decreases.

5.3 Analysis using Han's dataset

Han's dataset includes P-wave velocity, S-wave velocity, and density measurements for both dry case and wet case at different pressures of 5MPa, 10MPa, 20MPa, 30MPa, 40MPa, and 50MPa. P-wave and S-wave velocities and density were used to calculate Ip, Is, $\lambda\rho$, $\mu\rho$, K, μ, λ, λ/μ, σ, $K-\mu$, $Ip^2 - c*Is^2$, and Fluid factor (ΔF). The fluid indicator coefficient used here is defined as the difference between the mean value for the dry sand and mean value for wet sand divided by the standard deviation value of the dry sand. This indicator has the advantage of taking into account the spread

of the attribute value within the collection of samples considered (Dillon et al., 2003). A higher value represents better discrimination.

The lab measurements are also used to estimate the value for the c term in the $Ip^2 - c * Is^2$ fluid indicator using P-wave and S-wave velocity and density for dry case. As shown from Figure 4.13, the best value of $(V_p / V_s)_{dry}$ for different differential pressure ranges from 1.5 to 1.55, thus the best c value should between 2.25 and 2.4. Table 5.1 and Table 5.2 show the mean value, standard deviation and the fluid indicator coefficient for the fluid indicators related to the dry case and wet case at different differential pressures. It can be observed that the fluid coefficients for $\lambda\rho$, K, λ, λ/μ , σ , $K-\mu$, $Ip^2 - c * Is^2$, and Fluid factor (ΔF) are higher than those for other indicators, which means these indicators can easily separate the wet sandstone from the dry sandstone. Among these indicators, $Ip^2 - c * Is^2$ is the most sensitive indicator to the fluid content since we found the optimal value of c value. The rigidity modulus related attributes, such as V_s, Is, $\mu\rho$, μ, have no chance to distinguish the dry sandstone from the wet sandstone.

Figure 5.4 is the plot of the fluid indicator coefficient versus differential pressure. These lines suggest that with increasing differential pressure, we have a less chance to separate the dry sandstone from the wet sandstone. At a pressure of 5 MPa, the fluid indicator coefficients for $\lambda\rho$, K, λ, λ/μ, σ, $K-\mu$, $Ip^2 - c * Is^2$, and Fluid factor (ΔF) are a slightly higher than those at a pressure of 50 MPa. That means that the chance to differentiate the dry sandstone from the wet sandstone increases at shallow depths, but decreases at deeper depths.

Table 5.1 Mean and standard deviation values and fluid indicator coefficients for fluid indicators at 5 MPa.

Fluid indicators		V_p **(km/s)**	V_s **(km/s)**	V_p/V_s **(-)**	ρ **(g/cc)**	I_p **(km/s.g/cc)**	I_s **(km/s.g/cc)**	$\mu\rho$ **(GPa.g/cc)**	$\lambda\rho$ **(GPa.g/cc)**
Dry	Mean	3.33	2.22	1.5	2.2	7.4	4.94	26.34	6.29
	Std.dev.	0.73	0.49	0.06	0.2	2.07	1.41	15.74	4.68
Wet	Mean	3.84	2.19	1.77	2.37	9.15	5.22	29.19	28.59
	Std.dev.	0.6	0.48	0.12	0.13	1.8	1.34	15.76	6.97
FIC		**0.70**	**0.06**	**4.50**	**0.85**	**0.85**	**0.20**	**0.18**	**4.76**
Fluid indicators		K **(GPa)**	μ **(GPa)**	λ **(GPa)**	λ/μ **(-)**	σ **(-)**	$K-\mu$ **(GPa)**	$I_p^2 - cI_s^2$ **(GPa.g/cc)**	ΔF **(-)**
Dry	Mean	10.61	11.62	2.86	0.26	0.1	-1.01	-0.29	-0.29
	Std.dev.	5.5	6.13	2.01	0.17	0.06	1.86	3.85	0.06
Wet	Mean	20.03	12.11	11.96	1.16	0.26	7.92	21.29	-0.04
	Std.dev.	5.35	6.07	2.42	0.42	0.05	2.6	6.31	0.08
FIC		**1.71**	**0.08**	**4.53**	**5.29**	**2.67**	**4.80**	**5.61**	**4.17**

Differential Pressure:5MPa
FIC: Fluid Indicator Coefficient

Table 5.2 Mean and standard deviation values and fluid indicator coefficients for fluid indicators at 50 MPa.

Fluid indicators		V_p **(km/s)**	V_s **(km/s)**	V_p/V_s **(-)**	ρ **(g/cc)**	I_p **(km/s.g/cc)**	I_s **(km/s.g/cc)**	$\mu\rho$ **(GPa.g/cc)**	$\lambda\rho$ **(GPa.g/cc)**
Dry	Mean	4.02	2.6	1.55	2.2	8.89	5.77	34.97	12.59
	Std.dev.	0.58	0.41	0.04	0.2	1.86	1.3	16.26	4.56
Wet	Mean	4.21	2.5	1.69	2.37	10.03	5.97	37.26	28.93
	Std.dev.	0.54	0.44	0.09	0.13	1.71	1.28	16.59	7.04
FIC		**0.33**	**0.24**	**3.50**	**0.85**	**0.61**	**0.15**	**0.14**	**3.58**
Fluid indicators		K **(GPa)**	μ **(GPa)**	λ **(GPa)**	λ/μ **(-)**	σ **(-)**	$K-\mu$ **(GPa)**	$I_p^2 - cI_s^2$ **(GPa.g/cc)**	ΔF **(-)**
Dry	Mean	16.03	15.52	5.69	0.39	0.14	0.51	5.6	-0.25
	Std.dev.	5.27	6.12	1.84	0.13	0.03	1.91	3.6	0.05
Wet	Mean	22.45	15.5	12.12	0.88	0.23	6.95	21.48	-0.08
	Std.dev.	5.11	6.27	2.52	0.3	0.05	3.09	6.9	0.09
FIC		**1.22**	**0.00**	**3.49**	**3.77**	**3.00**	**3.37**	**4.41**	**3.40**

Differential Pressure:50MPa
FIC: Fluid Indicator Coefficient

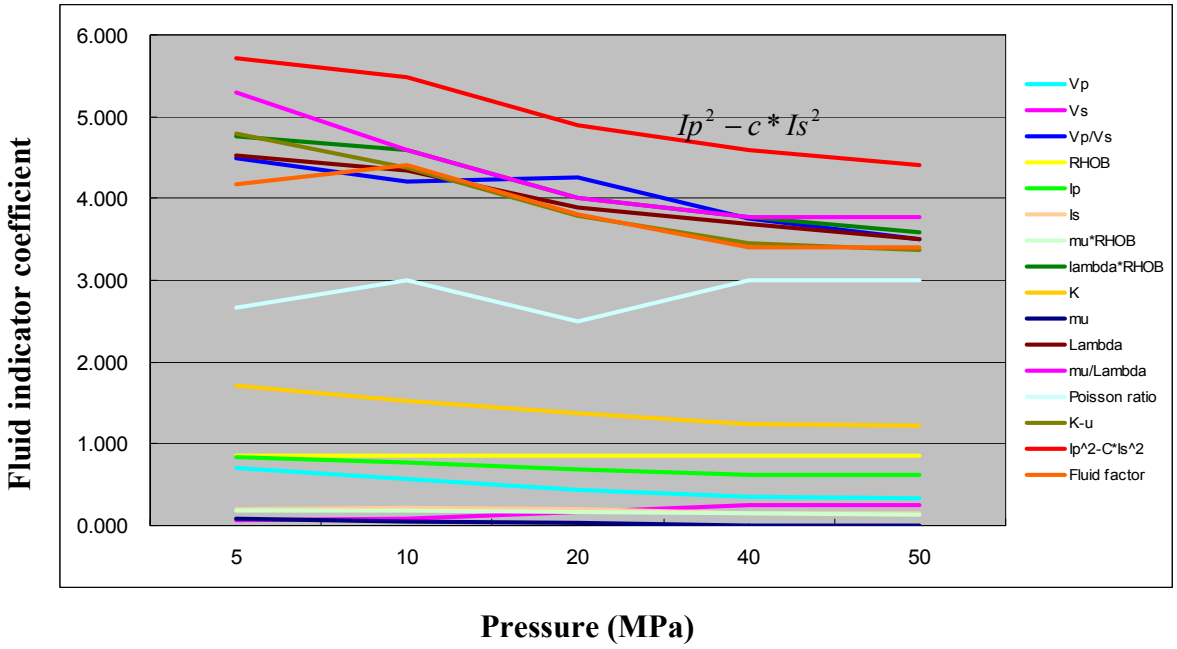

Figure 5.4 Fluid indicators coefficient versus pressure. Observe that the indicator: $Ip^2 - c * Is^2$ is most effective indicator.

5.4 Crossplot analysis for the fluid indicators

A number of observations can be made from the cross-plot analysis:

1) Figure 5.5 is a crossplot of $Ip^2 - c * Is^2$ versus Ip for 5 MPa pressure with c equal to 2.233. Figure 5.6 is a crossplot of $K - \mu$ versus Ip and Figure 5.7 is a crossplot of $\lambda\rho$ versus Ip. Comparing these cross-plots, although there are poor separation between the dry sandstone and the wet sandstone for Ip, it can be observed that there is good clustering for dry sandstone and wet sandstone in $Ip^2 - c * Is^2$ direction. This means Ip and $Ip^2 - c * Is^2$ values are fundamentally more orthogonal, which provides the best clusters for dry sandstone and wet sandstone.

2) There is a better clustering for dry sandstone than for wet sandstone. The reason for this stems from the difference in the bulk modulus between gas and water. The larger bulk modulus of water makes the values range of $Ip^2 - c * Is^2$ much larger. Although the range of $Ip^2 - c * Is^2$ for wet sandstone is larger than that for dry sandstone, there is no overlap for the dry and wet sandstones in $Ip^2 - c * Is^2$ direction.

3) The clay content also affects the separation between dry sandstone and wet sandstone. The color bars in the Figure 5.5 to Figure 5.7 represent the clay content. It can be observed that with increasing clay content the dry sandstone with high clay content scatter to the left. However, the wet sandstone with high clay scatters to the right. The reason for this may be due to the bound water in the imbedded shale which makes the fluid term much larger for wet sandstone. By contrast, the clay in dry sandstone makes the fluid term more negative. Thus, a certain fraction of clay content may help improve the discrimination capability of $Ip^2 - c * Is^2$ between dry and wet sandstones.

4) Not only clay content but also porosity will affect the discrimination between dry sandstone and wet sandstone. Figure 5.8 shows the crossplot of the fluid term using c=2.2333 versus P-wave impedance color-coded with porosity for the dry and wet sandstone samples at pressure of 5 MPa. The samples with high porosity, which are in red, cluster easily and do not overlap. However, those samples with lower porosity, which are in blue color, scatter to both sides and there is overlap between wet sandstone and dry sandstone when an improper c value is applied. In other words, for the porous sandstone with high porosity, whatever c value is chosen, they are ready to cluster which make it easy to discriminate dry sandstone from wet sandstone. For the tight sandstone

with lower porosity, an improper c value will make the fluid terms overlap between wet sandstone and dry sandstone, which makes it difficult to separate two cases.

5) Lastly, the pressure also affects the discrimination capability of $Ip^2 - c * Is^2$. Figure 5.9 shows the crossplot of the fluid term using c=2.2333 versus P-wave impedance, color-coded with porosity, for dry and wet sandstone samples at pressure of 50 MPa. Comparing Figure 5.8 with Figure 5.9, it can be observed that there is an obvious separation between the wet and dry sandstones at a pressure of 5 MPa. On the contrary, the samples for wet and dry sandstones overlap and there is poor separation between wet and dry sandstones at a pressure of 50MPa. That means that increasing differential pressure makes the discrimination between wet sandstone and dry sandstone more difficult. This observation agrees with the analysis result in Figure 5.4.

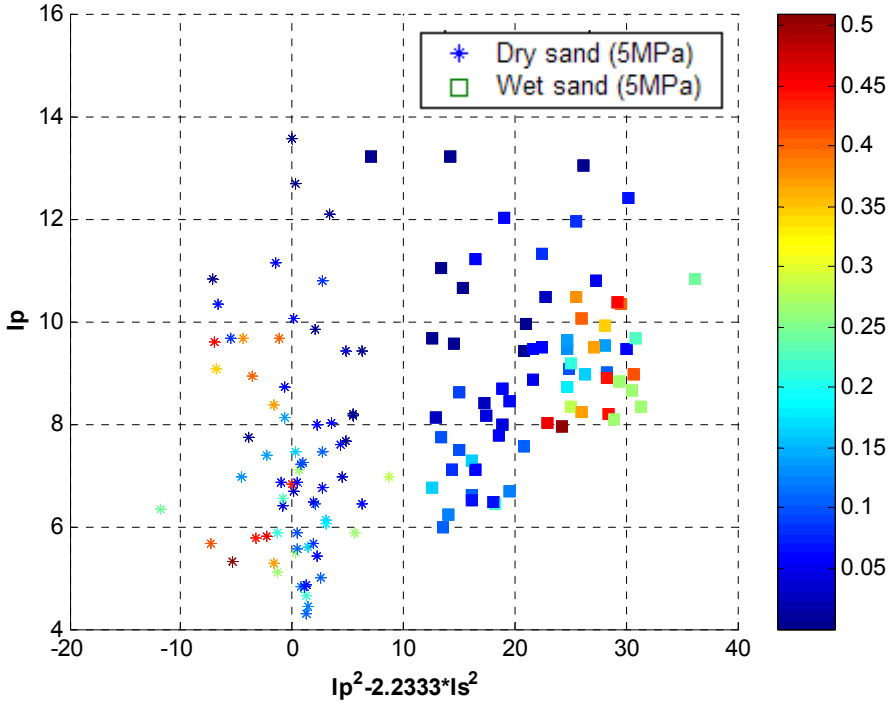

Figure 5.5 Crossplot of fluid term ($\rho f = Ip^2 - 2.2333 * Is^2$) versus P-wave impedance (Ip) color-coded with clay content for dry and wet sandstone samples at Pe=5 MPa.

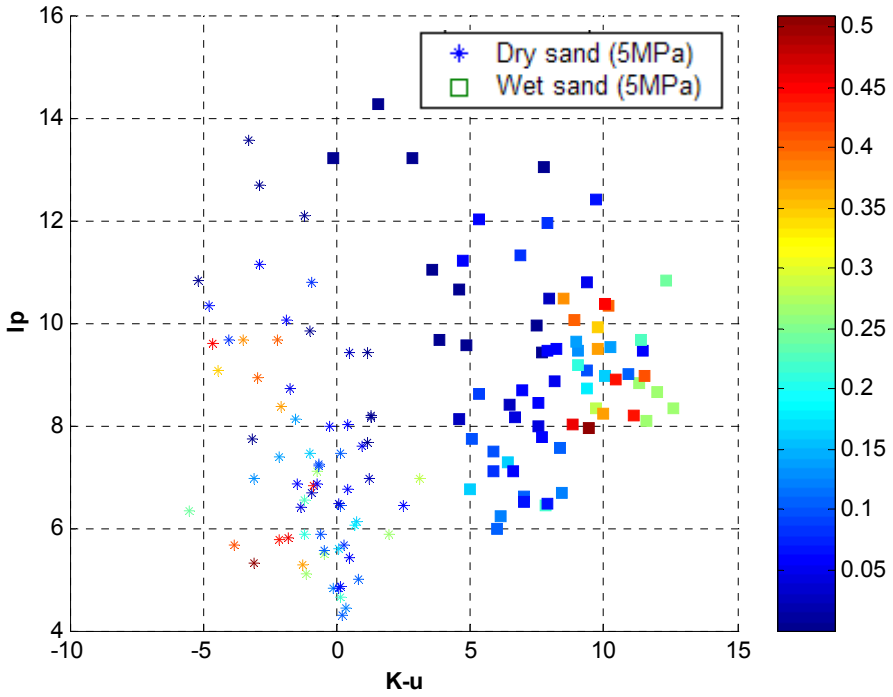

Figure 5.6 Crossplot of fluid term ($K-\mu$) versus P-wave impedance (Ip) color-coded with clay content for dry and wet sandstone samples at Pe=5 MPa.

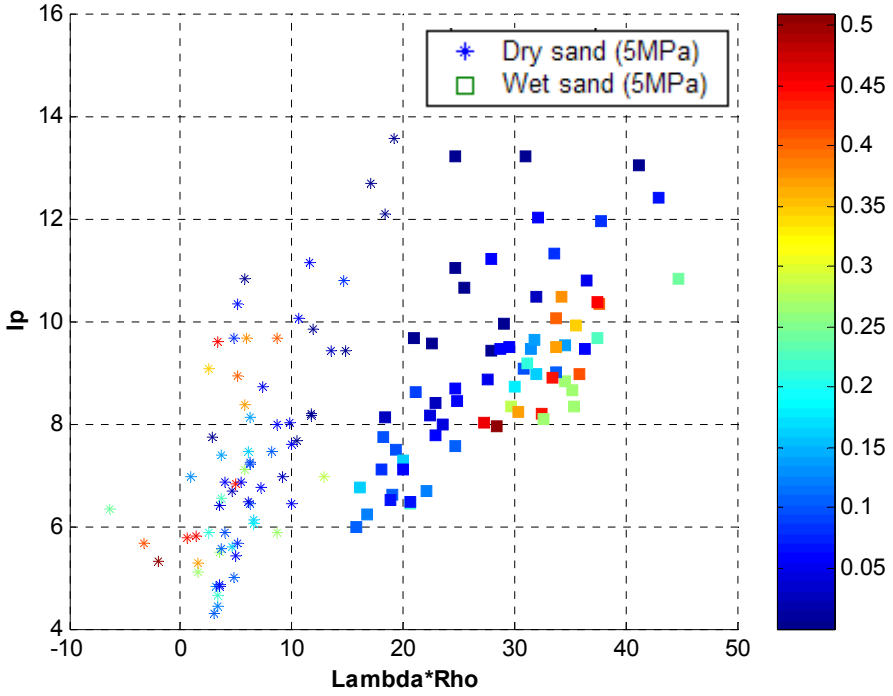

Figure 5.7 Crossplot of fluid term ($\lambda\rho$) versus P-wave impedance (Ip) color-coded with clay content for dry and wet sandstone samples at Pe=5 MPa.

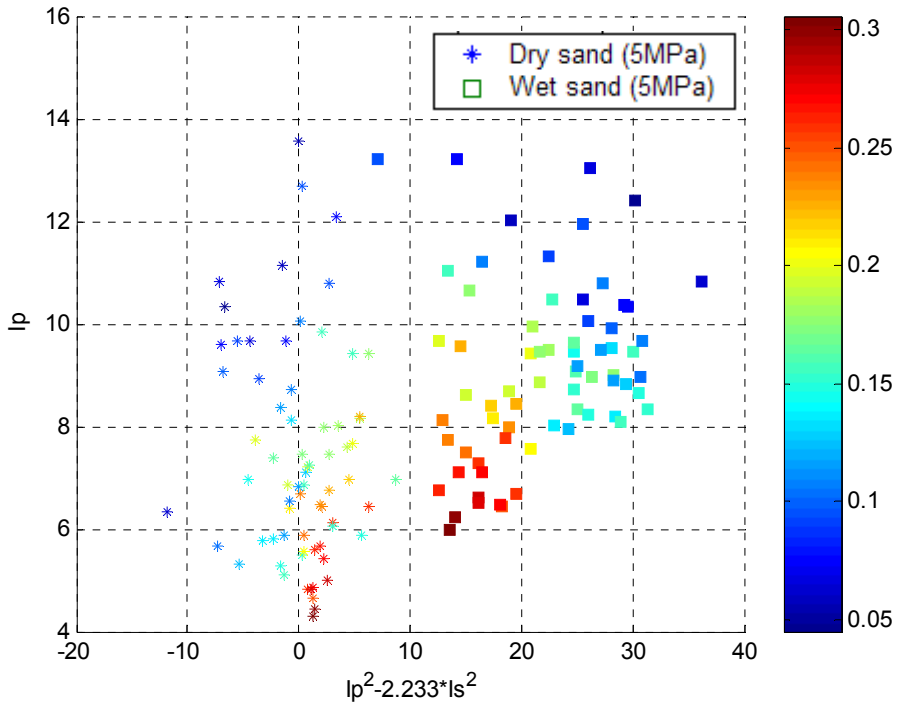

Figure 5.8 Crossplot of fluid term ($\rho f = Ip^2 - 2.2333 * Is^2$) versus P-wave impedance (Ip) color-coded with porosity for dry and wet sandstone samples at Pe=5 MPa.

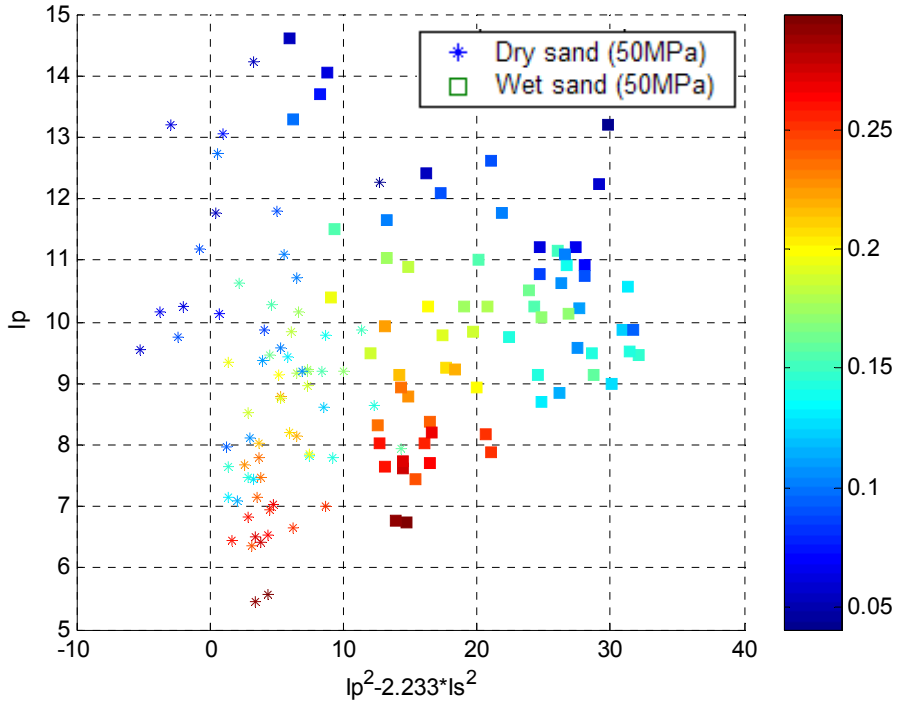

Figure 5.9 Crossplot of fluid term ($\rho f = Ip^2 - 2.2333 * Is^2$) versus P-wave impedance (Ip) color-coded with porosity for dry and wet sandstone samples at Pe=50MPa.

5.5 Using different C values

Since $Ip^2 - c * Is^2$ is the best fluid indicator for discriminating wet sandstone from dry sandstone, it is very important to select an appropriate c value to get a better separation between dry and wet sandstones. Crossplot analysis using different c values shows how c value affects the clustering of dry and wet sandstones. Figures 5.10 to Figure 5.13 show the crossplots of Ip versus ρf using different c values (c equal to 2.8, 2.333, 2.233, and 2 respectively). The dry and wet cases are indicated by different symbols.

On a crossplot of Ip versus ρf (Figure 5.10, $c = 2.8$), there are two clusters associated with wet and dry sandstones. For the samples with high Ip value, they deviate from the base lines (ρf =0 for dry sandstones and ρf =20 for wet sandstones) to the left. It is hard to select a cut-off value to separate wet sandstone from dry sandstone.

For the crossplots of Ip versus ρf (Figure 5.11, $c = 2.333$, Figure 5.12, $c = 2.233$), some samples with high Ip value start to align along the base lines to show the better separation between dry sandstone and wet sandstone.

In the crossplot of Ip versus ρf (Figure 5.13, $c = 2$), the samples deviate from the base lines to the right. That is, the separation line trends from bottom left to top right.

Comparing these crossplots from c =2 to c =2.8, it can be observed that the best choice would appear to be $c = 2.233$, because the clustering of dry sandstone are much closer to the base line (ρf =0) and there is best separation between wet and dry sandstones. The crossplot using $c = 2$, which corresponds to the LMR (lambda-mu-rho) method of Goodway et al. (1997), would not give as good a separation between dry and wet sandstones.

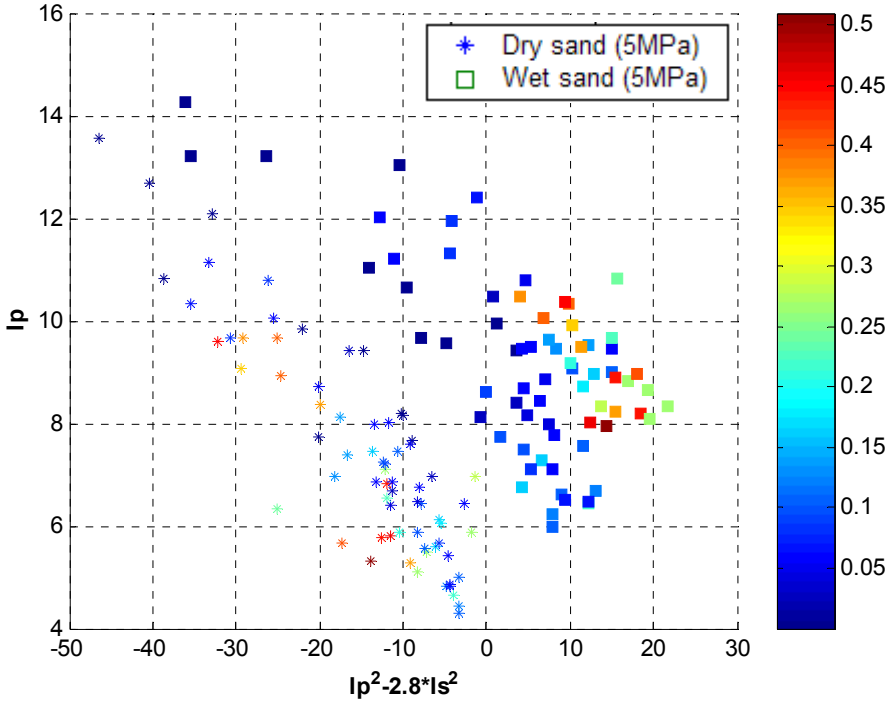

Figure 5.10 Crossplot of fluid term (ρf , $c = 2.8$) versus P-wave impedance (Ip) color-coded with clay content for dry and wet sandstone samples at Pe=5 MPa.

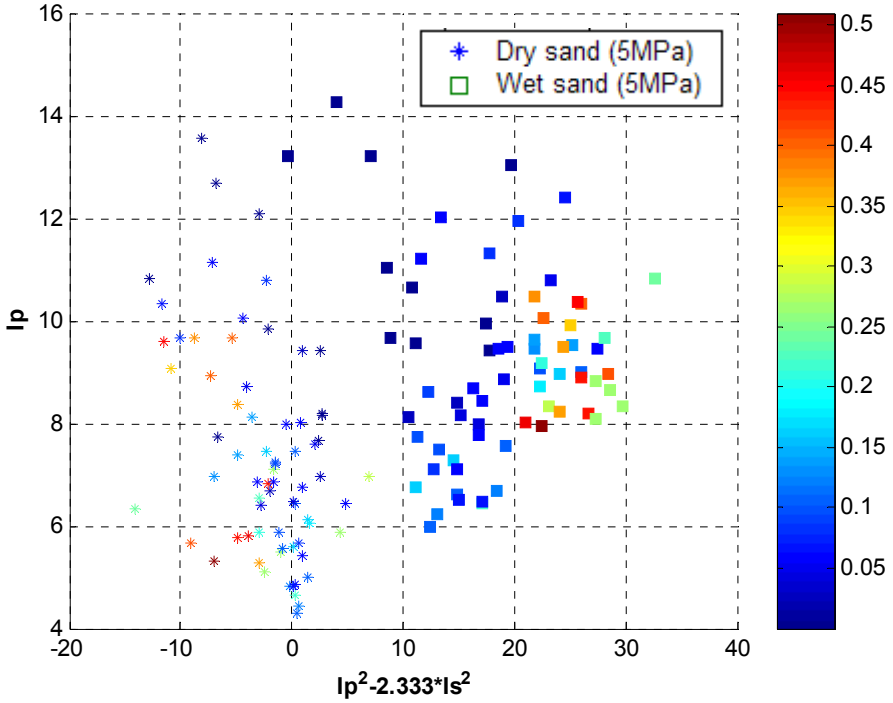

Figure 5.11 Crossplot of fluid term (ρf , $c = 2.333$) versus P-wave impedance (Ip) color-coded with clay content for dry and wet sandstone samples at Pe=5 MPa.

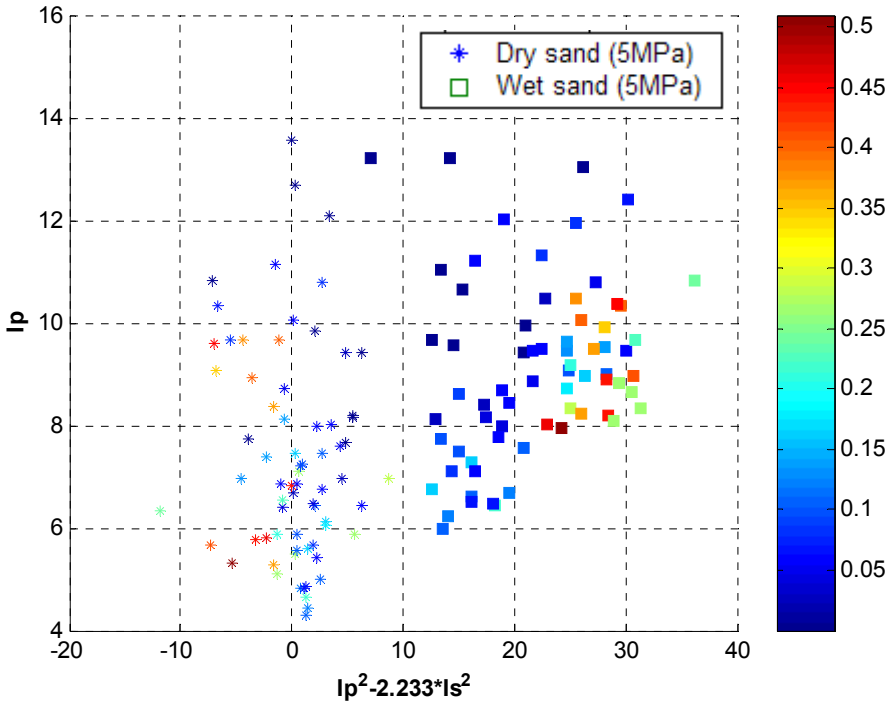

Figure 5.12 Crossplot of fluid term (ρf , $c = 2.233$) versus P-wave impedance (Ip) color-coded with clay content for dry and wet sandstone samples at Pe=5 MPa.

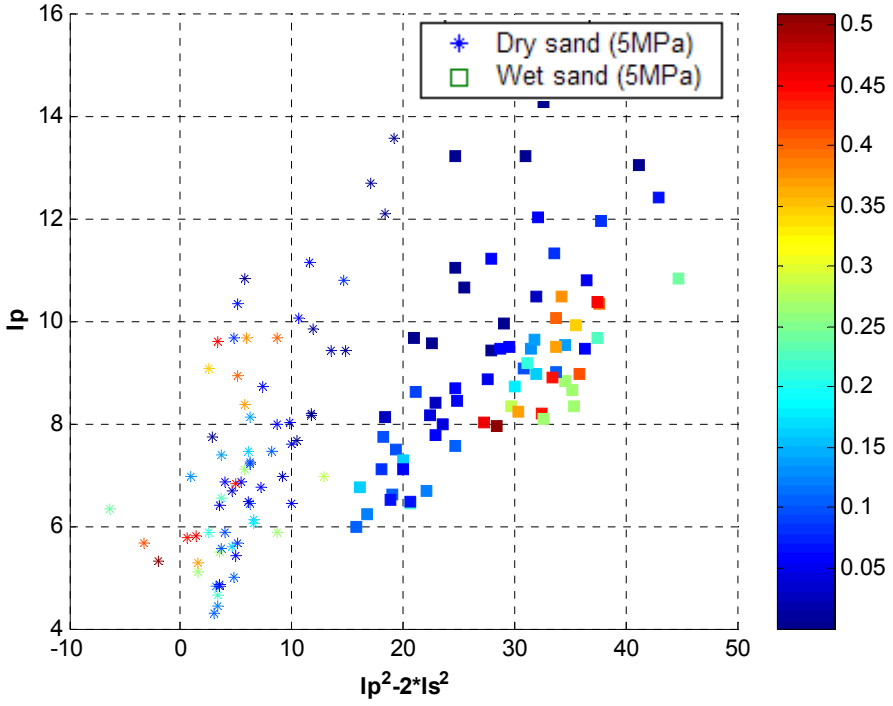

Figure 5.13 Crossplot of fluid term (ρf , $c = 2$) versus P-wave impedance (Ip) color-coded with clay content for dry and wet sandstone samples at Pe=5 MPa.

5.6 Conclusion

Based on the above analysis, it can be summarized that:

1. The fluid indicators: $Ip^2 - c * Is^2$, $K - \mu$, $\lambda\rho$, K, λ, λ / μ, and σ are more sensitive to fluid content than other attributes, such as V_p / V_s ratio, and P-wave impedance. Cross plots show that the fluid indicators: $Ip^2 - c * Is^2$, $K - \mu$ exhibit almost the same discrimination capability between the dry and wet sandstones. However, the fluid indicator $\lambda\rho$ does not provide a better separation between wet and dry sandstones. Among these fluid indicators, $Ip^2 - c * Is^2$ is the most sensitive to the fluid content. The theoretical reason for this is that this attribute is dominated by the pore fluid whereas other fluid indicators are affected by fluid and rock skeleton combined.

2. For unconsolidated sandstone with higher porosity, the fluid indicators $Ip^2 - c * Is^2$, $K - \mu$, $\lambda\rho$ provide better discrimination between dry and wet sandstones. However, for consolidated sandstone with lower porosity, the fluid indicator $Ip^2 - c * Is^2$ offers the best discrimination between dry and wet sandstones.

3. With an increasing pressure, the sensitivity of fluid indicators ($Ip^2 - c * Is^2$, $K - \mu$, $\lambda\rho$, K, λ, λ / μ, and σ) to the fluid content is reduced. This means that with increasing compaction and cementation, the discrimination of the dry sandstone from the wet sandstone will therefore be more difficult.

4. The c value plays an important role in the fluid indicator: $Ip^2 - c * Is^2$. Success of $Ip^2 - c * Is^2$ method is subject to the appropriate estimation of c value. This can be done empirically using measured well log values.

CHAPTER SIX: BLACKFOOT CASE STUDY

6.1 Introduction

With the conventional stacked P-wave seismic reflection data only, the interpretation is limited to the structure and P-wave impedance. However, with the AVO analysis, additional information such as S-wave velocity and impedance and elastic rock parameters are available, which can provide more detailed information for estimating lithology and fluid content.

In this chapter, the generalized fluid method is applied to P-wave seismic data in Blackfoot area to image the areal extent of porous sandstone within a Glauconitic incised valley system and also to discriminate the fluid content of the channel system.

For real seismic data, not only the selection of c value but also the quality of AVO inversion of the seismic data will affect the result of the generalized fluid method. The estimation of the c value using well logs, and based on Gassmann fluid substitution theory, will be discussed in this chapter. Pre-stack inversion is performed to extract P-wave and S-wave impedance using the AVO and STRATA packages from Hampson-Russell Software. Finally, the fluid indicator $Ip^2 - c * Is^2$ will be extracted to better understand the capability of this method to indicate the presence of hydrocarbons within the Glauconitic incised valley system.

6.2 Seismic and well data

In 1995, a 3C-3D survey was acquired over the Blackfoot Field, located 20 km southeast of Strathmore, Alberta, as shown Figure 6.1. This figure shows the paleogeography of the Lower Cretaceous, at the time the incised valley system was formed. The objectives of the survey were to: 1) delineate a Glauconitic incised valley system, 2) distinguish

between sand and shale valley fills, and 3) delineate hydrocarbon content within the Glauconitic incised valley system (Margrave et al., 1998). The seismic data used in this study is one portion of the whole survey of the P-P data, covers the Glauconitic incised valley system and two wells which have P-wave and S-wave sonic well logs. An amplitude-preserving processing scheme was run using PROMAX and VISTA software and AVO attributes were derived using STRATA package from Hampson-Russell Software. The zone of interest is the upper valley around 1024 ms and lower valley at 1040 ms on the P-wave post-stack seismic section (see figure 6.4).

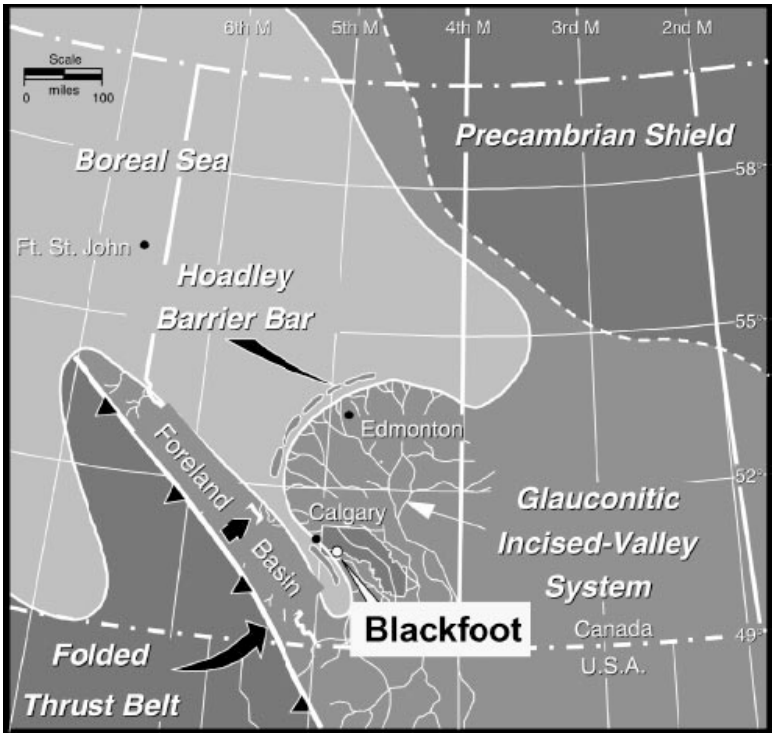

Figure 6.1 Paleogeography of Lower Cretaceous during the formation of the Glauconitic incised-valley system and location of Blackfoot area (Dufour et al., 2002).

There are only two wells available (08-08 and 04-16) which have P-wave and S-wave sonic logs and density logs. The dipole logs were acquired from the top of the Mannville to the top of Mississippian, which cover the Glauconitic incised valley system. These two wells were loaded into Geoview package from Hampson-Russell Software for well calibration and c value extraction.

6.3 Geological background

The depositional environment in Blackfoot area is characterized by a meandering fluvial system with paledrainage from south to north of figure 6.1. Three sets of incised valleys: upper, lithic, and lower valleys, which correspond to the different fluvial and estuarine sediments during the increasing and falling of relative sea level, are found in the complex compound incised-valley system (Broger et al., 1997).

Figure 6.2 is a schematic diagram for the three different incised valleys. The upper and lower incised valleys are mainly composed of sandstone with an average porosity of approximately 18% and permeability around 750 md, and are the main reservoirs. The lithic incised valleys are made of denser lithic sandstone of low permeability are considered as non-reservoir (Miller, 1996).

The main production zone in the Blackfoot area is the upper Glauconitic Group and the primary fluid in the upper incised valleys is oil. Gas is occasionally present in the upper incised valleys (Miller, 1996). Figure 6.3 shows the time structure of Ostracod horizon, which indicates a structure trap around the 08-08 well and the 04-16 well. Figure 6.4 show the seismic section with horizons and the resistivity log superimposed. The horizons labeled Ostracod and Mississippian represent the top and base of the Glauconitic

incised valley system. The large value in the resistivity well log indicates the presence of hydrocarbons.

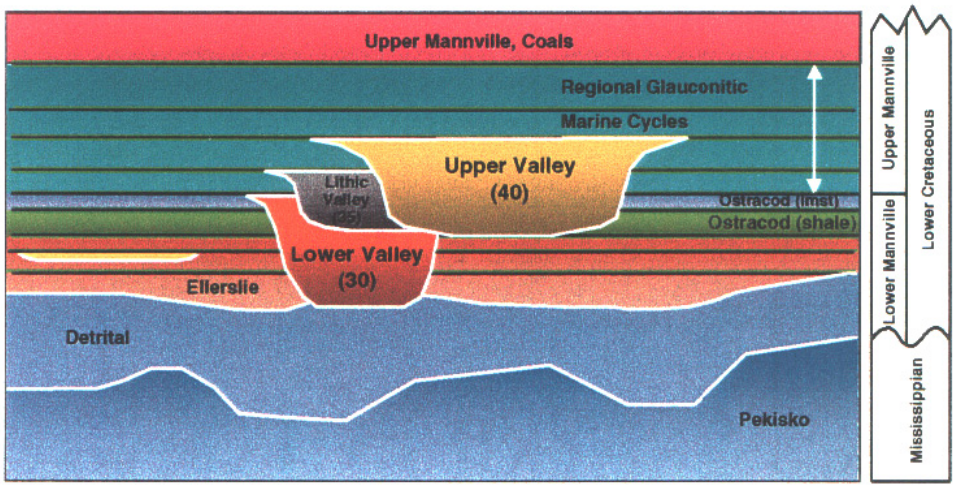

Figure 6.2 Schematic stratigraphy of the Glauconitic incised valley system (Dufour et al., 2002).

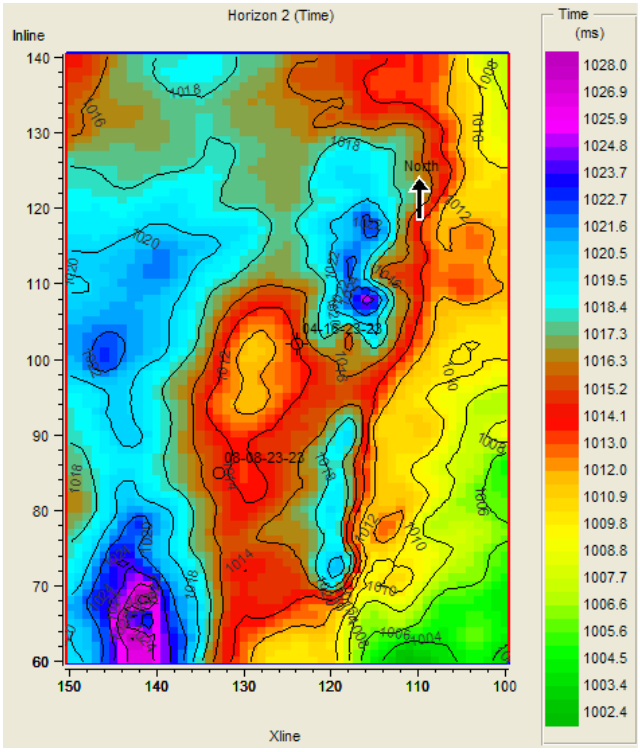

Figure 6.3 The time structure for the Ostracod horizon (upper valley) and well locations.

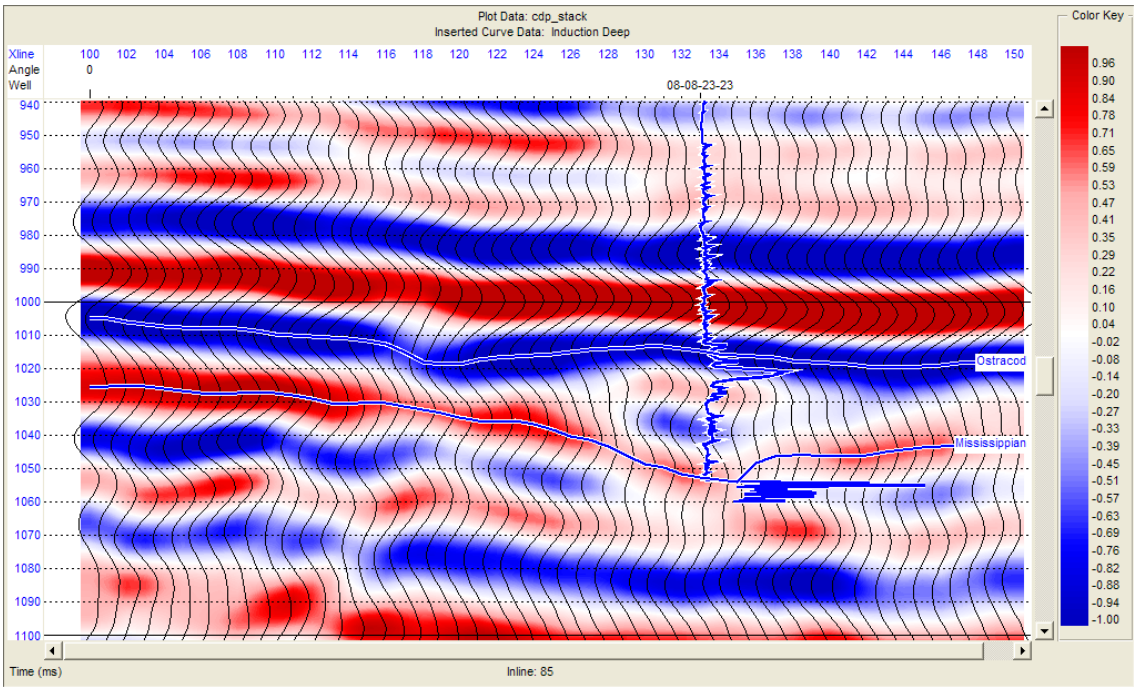

Figure 6.4 Seismic section across the well 08-08 with Ostracod and Mississippian horizons and resistivity well log.

Post-stack seismic data can provide interpretation of structural traps or lithological facies distribution. The time slices in figure 6.5 show anomalous amplitudes associated with the upper and lower incised valleys with gas or oil bearing porous sandstone. The wide upper valley goes from south to north and the narrow lower valley goes from southwest to northeast. These two incised valleys both run across the 08-08 and 04-16 wells. However, it is hard to infer the presence of the hydrocarbon in the upper and lower valley systems. Based on the resistivity logs and other rock property curves for the 08-08 and 04-16 wells, the 08-08 well indicates the presence of hydrocarbon in the upper valley whereas the 04-16 well does not. Therefore, the post-stack seismic does not support the interpretation of the hydrocarbon in the Glauconitic incised valley system. However, the generalized fluid method can provide additional fluid information together with other elastic rock

parameters and it can greatly improve the imaging and fluid interpretation in the Glauconitic incised valley systems.

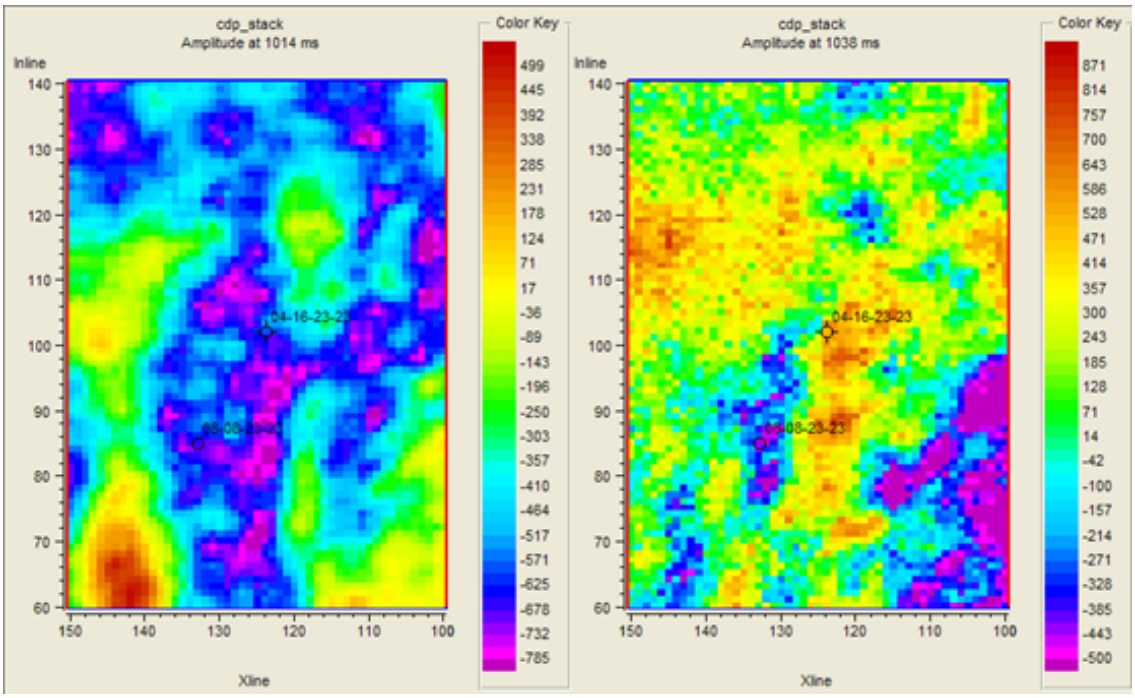

Figure 6.5 Time slices from P-wave stack which show the upper valley (left) and lower valley (right). The low amplitude maps the porous sandstone in the Glauconitic channel system.

6.4 True amplitude processing of the Blackfoot PP data

The success of AVO pre-stack inversion is subject not only to the inversion algorithms but also to the processing sequence applied to the data. For obvious and strong AVO effects, the amplitude bias introduced by poor processing algorithms can be overcome. However, for weak AVO effect, often associated with the presence of hydrocarbons, unsatisfactory processing is even more damaging (Allen and Peddy, 1993).

There are three important issues throughout the amplitude-preserving process:

1) The relative amplitudes for the common reflection point (CRP) gather must be preserved to maintain the amplitude variation with offset.

2) Surface-consistent related techniques should be applied to maintain the relative amplitudes within common reflection point (CRP) gathers, such as surface-consistent static correction and surface-consistent deconvolution.

3) An appropriate migration algorithms must be used to properly image the amplitudes prior to the pre-stack amplitude inversion to derive the AVO attributes.

The best processing sequence should be chosen by investigating the amplitude behaviour from each processing sequence and then calibrating with the theoretical reflection coefficients derived from the well logs. After evaluation, the chosen processing flow for the P-P data was follows: 1) 3D geometry registration, 2) trace editing, 3) true amplitude recovery, 4) surface-consistent deconvolution, 5) elevation and refraction statics corrections, 8) velocity analysis, 9) residual surface consistent statics, 10) normal moveout, 11) trim statics, 12) transformation from offset gather to angle gathers, and 13) gather smoothing.

6.5 Pre-stack seismic inversion

Using a linearized approximation for the Zoeppritz equations, and a least-squares curve fitting to the reflection amplitude variation, various reservoir parameters could be estimated. The typical outputs of pre-stack inversion are P-wave and S-wave reflectivities. These reflectivities can be transformed to the P-wave and S-wave impedance through conventional post-stack inversion. Other attributes can be estimated based on the P-wave and S-wave impedance. These include P-wave and S-wave velocity, density, and the attributes discussed in earlier chapters.

A key issue in pre-stack inversion is wavelet extraction. The extraction methods fall into three categories: 1) deterministic; 2) statistical; 3) using a well log. In this study the third method was used to extract the wavelets. Multiple wavelets should be estimated from different offsets to compensate for offset-dependent phase, bandwidth, tuning, and NMO stretch.

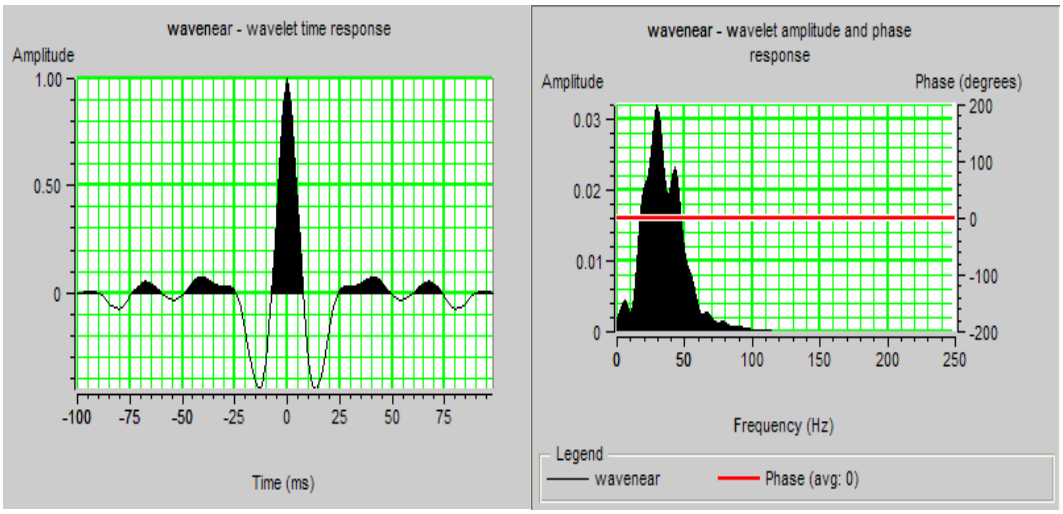

Figure 6.6 The waveform and the spectrum for the extracted wavelet for the near offset at the location of well 08-08.

Once the wavelets were extracted (Figure 6.6), well log correlation was performed. For both 08-08 and 04-16 wells, the synthetics and the extracted seismic traces around the wells were generated for the calibration. Shifting, stretching, and squeezing are applied to align the major events on the synthetic and extracted seismic trace to get the correct time-depth relationship to tie the well data to the seismic data. To remove spikes and noise on the well logs, blocking was applied on the P-wave and S-wave and density logs to get a better match between the synthetic and seismic data. The well calibration result is shown

in figure 6.7 and shows that the seismic character between synthetic and seismic match very well (i.e. the blue CDP stack matches the repeated red trace from Inline 85).

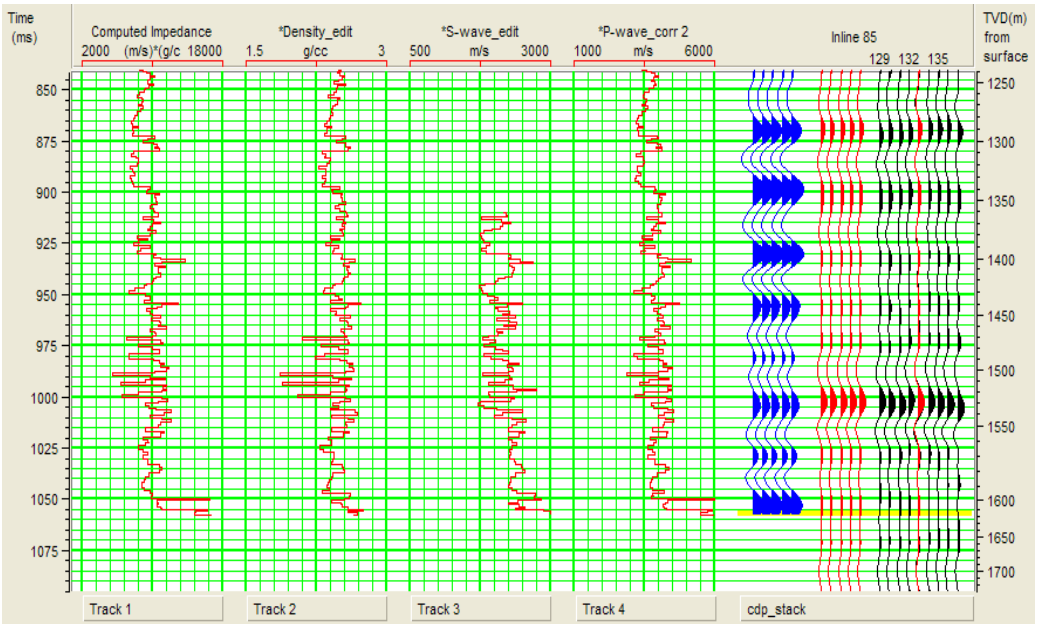

Figure 6.7 Well calibrations for well 08-08. Well logs were blocking processed. Synthetic is displayed in blue and extracted seismic trace is displayed in red.

The next step in the inversion process is to build an initial guess model for P-wave and S-wave impedance and density using an interpolation method. In this process, the picked seismic horizons are used to honour the stratigraphic information and to constrain the interpolation process (Hampson and Russell tutorial). The model was constrained by the smoothed well logs to provide the low frequency information. High frequency information through the later pre-stack inversion will be added to the model to obtain the full bandwidth information about P-wave and S-wave impedance and density.

After building the initial guess model, the inversion parameters are analyzed at well locations (Figure 6.8). Through the inversion analysis process, relationships between P-

wave and S-wave impedance and density for the background were obtained to stabilize the inversion (Hampson and Russell tutorial).

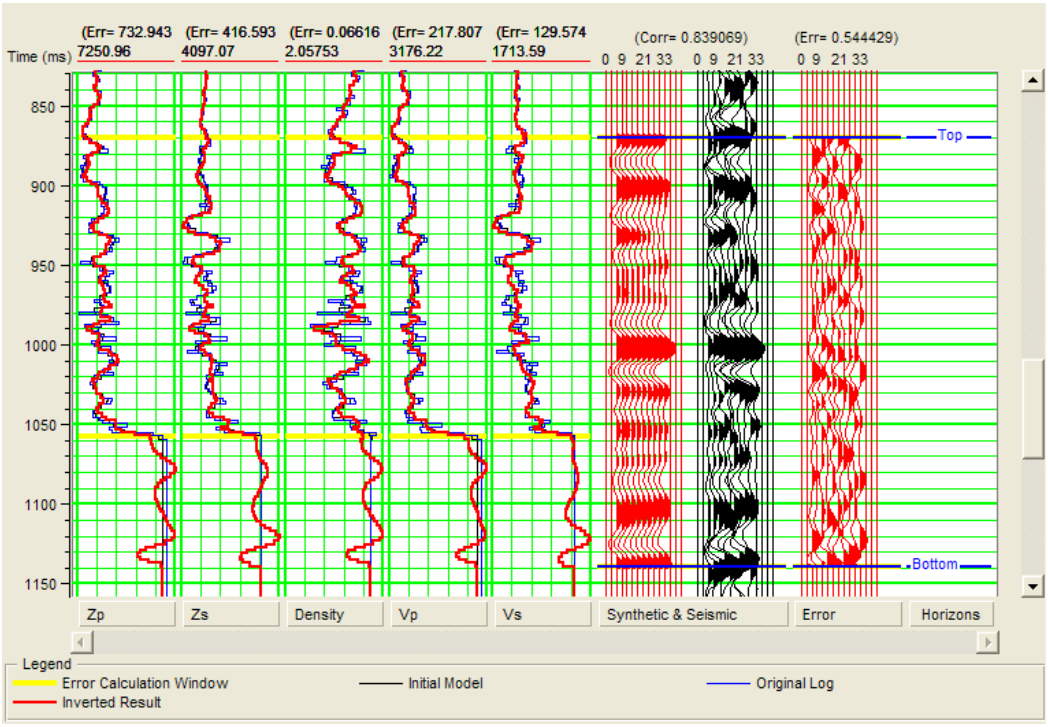

Figure 6.8 Inverted P-wave and S-wave impedance, velocity and density logs (in red) and the original ones (in blue) using pre-stack seismic inversion for well 08-08.

Finally, the optimized inversion parameters were applied to the whole volume to get P-wave impedance (Ip), S-wave impedance (Is), P-wave velocity (V_p), S-wave velocity (V_s), and density (ρ).

Theoretically, density is poorly imaged through AVO inversion when the angle gather range is less than 30 degrees. In this study, the maximum angle is 28 degree and the density was estimated based on the regression between density and P-wave impedance based on the well analysis.

Figure 6.9 and Figure 6.10 show the cross section of the P-wave impedance and S-wave impedance with the resistivity well log from 08-08 well superimposed. The zone of interest is the upper incised valley which is associated with the relative low impedance and high resistivity. It can be observed that the known upper and lower incised valleys correlate with low P-wave impedance values. However, from the cross-section of the S-wave impedance it is hard to discriminate the upper and lower incised valleys from the lithic incised valleys.

Figure 6.11 shows the extracted time slices at 1024 ms from the P-wave and S-wave impedance. The lower impedance anomalies are associated with porous sandstone in the upper incised valley and it is hard to observe the distribution of the porous sandstone from the time slice of the S-wave impedance.

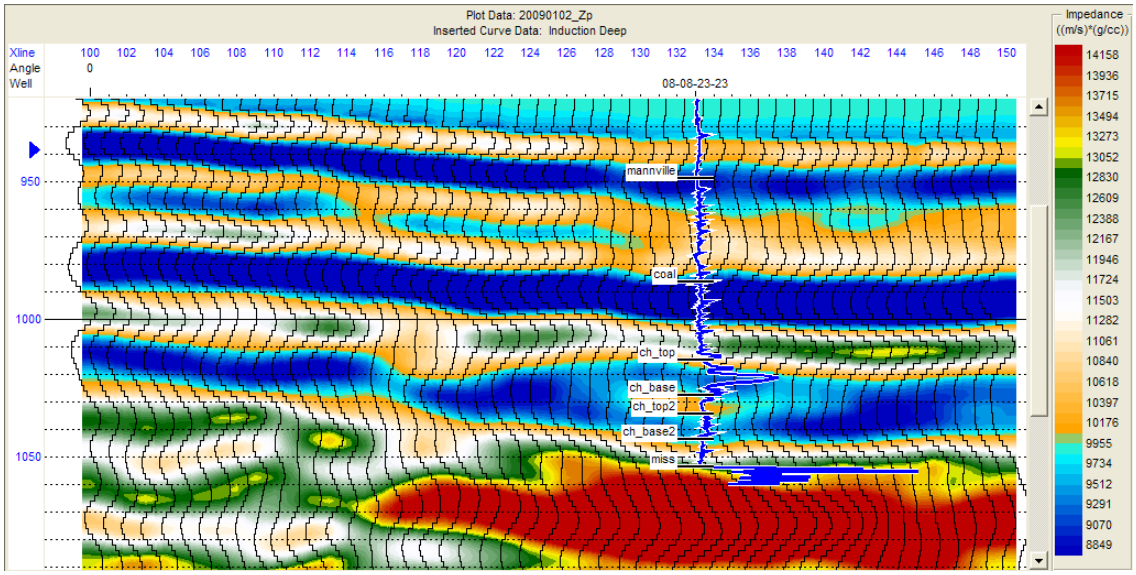

Figure 6.9 In-line 85 cross section of the inverted P-wave impedance (*Ip*) with well tops and resistivity well log superimposed.

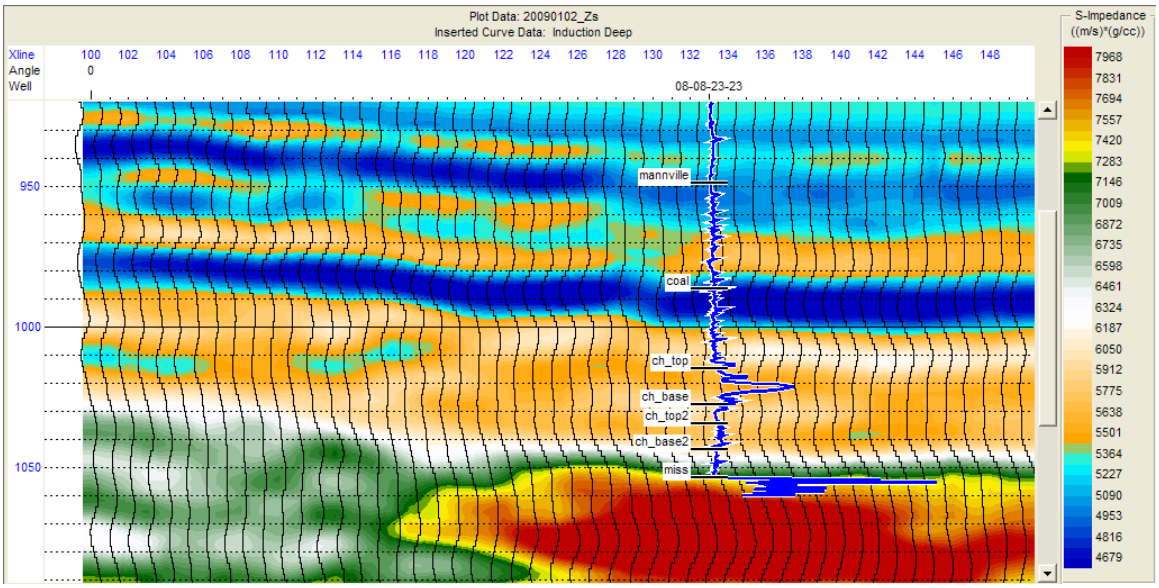

Figure 6.10 In-line 85 cross section of the inverted S-wave impedance (*Is*) with well tops and resistivity well log superimposed.

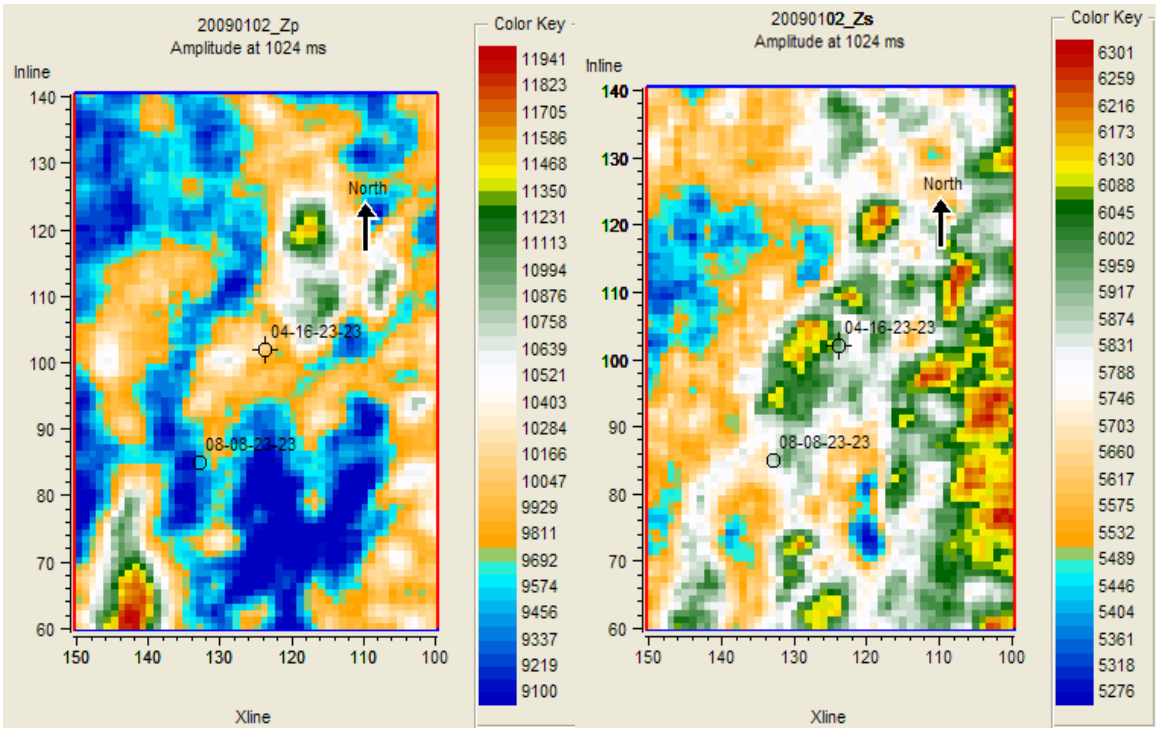

Figure 6.11 Time slices of P-wave impedance (left) and S-wave impedance (right) at the upper valley level with well locations.

6.6 The generalized fluid term extraction

6.6.1 C value extraction

To estimate the value of $(V_p / V_s)^2_{dry}$ at the well location, the dry values for the P-wave and S-wave velocity and density at the well location were inverted using the Gassmann equation. The local bulk modulus and density for the fluid was generated from the Batzle and Wang equations (Kumar, 2006). Figure 6.12 shows the estimated $(V_p / V_s)^2_{dry}$ values for the zone of interest. Figure 6.13 is the crossplot of c value versus porosity for well 08-08 at a depth interval of 1500 m-1750 m. It can be observed that c is approximately 2.3 for the Glauconitic sand and 2.7 for the shale.

The zone of interest is the Glauconitic upper and lower incised valleys and the purpose of this study is to discriminate the Glauconitic upper and lower incised valley from the shale background and to detect the fluid content inside the channel system. Thus, we choose the average c value for Glauconitic sand. From the Figure 6.13, the optimal value for upper and lower incised valley is 2.33.

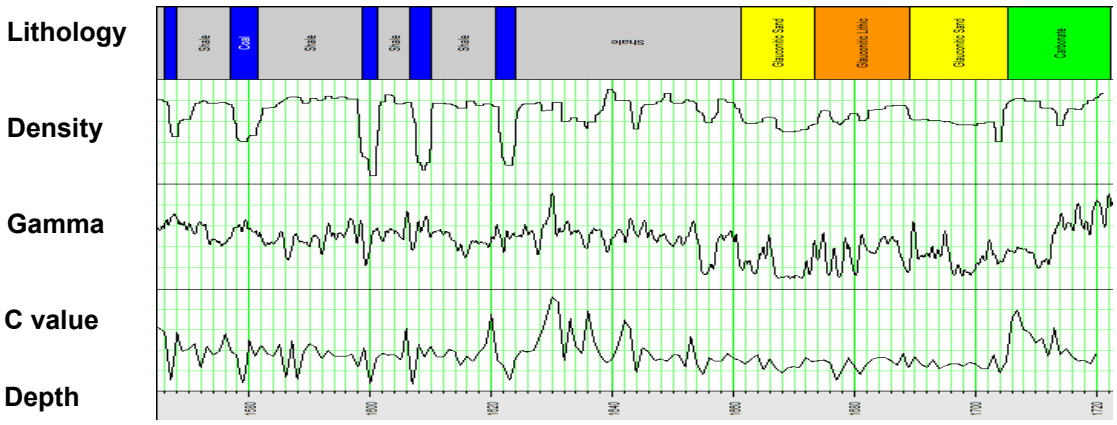

Figure 6.12 The estimated c value and gamma, density and lithology well logs for 08-08 well.

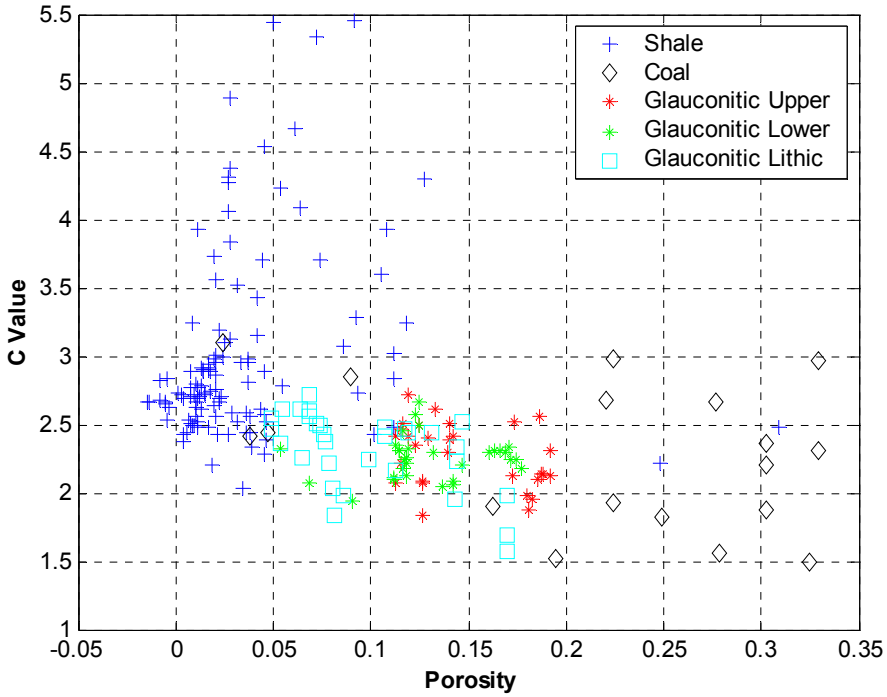

Figure 6.13 Crossplot of c value versus porosity for well 08-08, depth interval:1500 m-1750 m.

If the P-wave and S-wave sonic logs and density log are available, we can study the discrimination power of the logs and their transforms for lithology and fluid identification. Figure 6.14 shows the value of $\lambda\rho$ (track 3), Poisson's ratio (track 4), $K-\mu$ (track 5), V_p / V_s ratio (track 6), and $Ip^2 - c * Is^2$ (track 7) calculated using the P-wave and S-wave velocity and density for the 08-08 well. It can be observed that the fluid terms $Ip^2 - c * Is^2$, $\lambda\rho$, and $K-\mu$ show the same discrimination capability in separating the porous Glauconitic sand (upper and lower incised valley) from the lithic sand and shale, which means these indicators can be used to discriminate the upper and lower valleys from the lithic sandstone and shale background. Based on the well log display, $Ip^2 - c * Is^2$ is the most sensitive indicator for the fluid content.

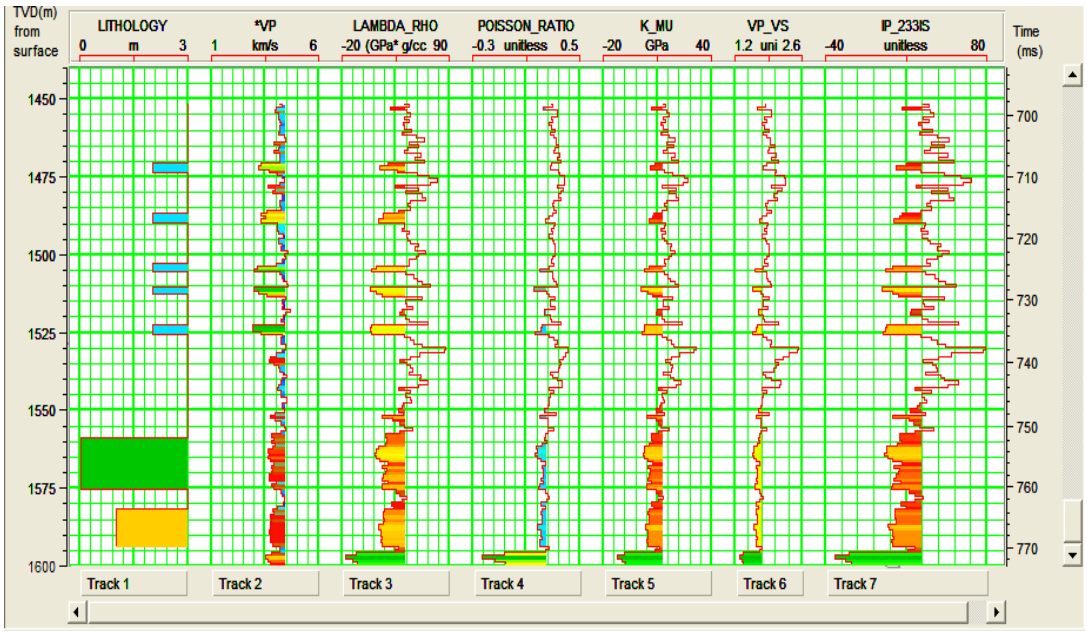

Figure 6.14 Comparison between P-wave velocity (V_p), Lambda*Rho ($\lambda\rho$), Poisson's ratio (σ), $K-\mu$, V_p/V_s and $Ip^2 - c*Is^2$ for well 08-08.

From the well log crossplot of ρf and ρs, the porous sandstone in the upper and lower valleys has distinctive ρf and ρs responses compared to lithic sandstone and shale (Figure 6.15). This is due to the fact that porous sandstones are more compressible than tight sandstones and more rigid than shale.

6.6.2 Fluid term extraction

Once P-wave impedance (Ip) and S-wave impedance (Is) were obtained, the estimated Ip and Is were then used to derive the fluid term (ρf) and skeleton term (ρs) using the following equations:

$$\rho f = I_p^{\,2} - cI_s^{\,2}, \qquad (6.1)$$

$$\rho s = I_s^{\,2}. \tag{6.2}$$

Also, given the inverted density, various elastic parameters can be estimated, such as incompressibility (λ), rigidity (μ), bulk modulus (K), and Poisson's ratio. However, owing to the limited angle range, the density was therefore not constrained by the density and P-wave velocity relationship observed in the well logs. For this reason, density can't be used to derive the separate elastic parameters for the interpretation of the lithology and fluid content.

From the $(V_p / V_s)^2{}_{dry}$ analysis based on the well logs for the target zone, the optimal $(V_p / V_s)^2{}_{dry}$ should be around 2.333. The fluid term (ρf) and skeleton term (ρs) are estimated using c =2.333.

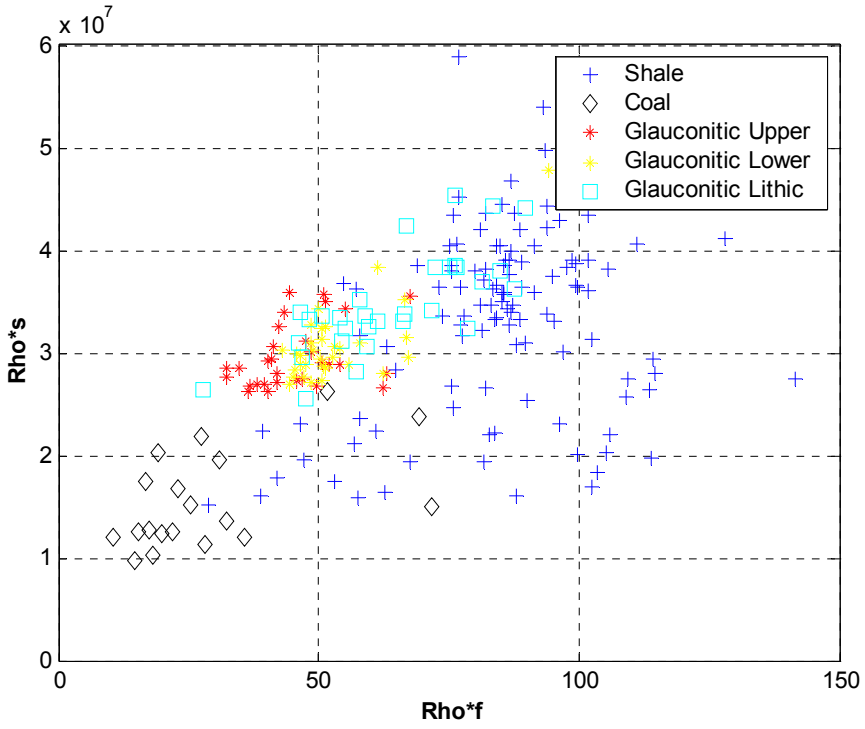

Figure 6.15 Crossplot of fluid term Rho*f (ρf) versus skeleton term Rho*s (ρs) for well 08-08.

Figures 6.16 and Figure 6.17 show the time slices of the fluid term (ρf) and skeleton term (ρs) for the upper valley and lower valley. As we know, there are hydrocarbons in well 08-08 at the upper and lower valley levels but not in well 04-16. The fluid term in Figure 6.16 indicates the presence of hydrocarbons in the porous sandstone within the Glauconitic incised valley system, which agrees with the observation on the well log data. The skeleton term in Figure 6.17 indicates the lithology information in the incised valley system. The relative higher value for the skeleton term time slice agrees with the fact that the valley was filled with the lithic sandstone with lower porosity at the location of the well 04-16.

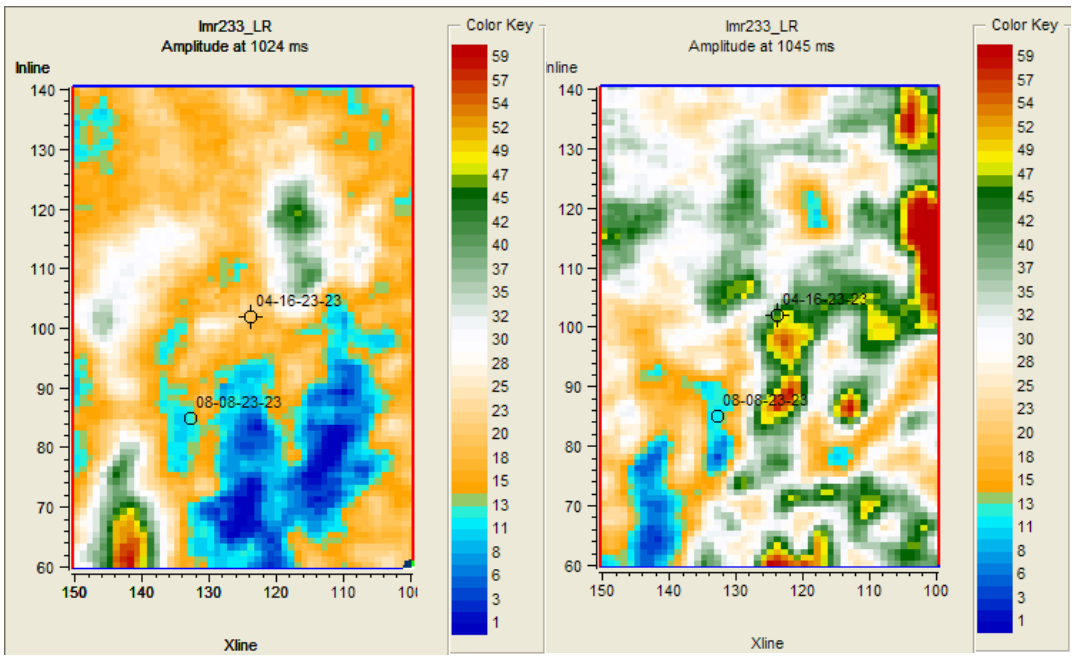

Figure 6.16 Time slices of fluid term (ρf , c =2.333) for the upper valley (left) and lower valley (right) with well locations.

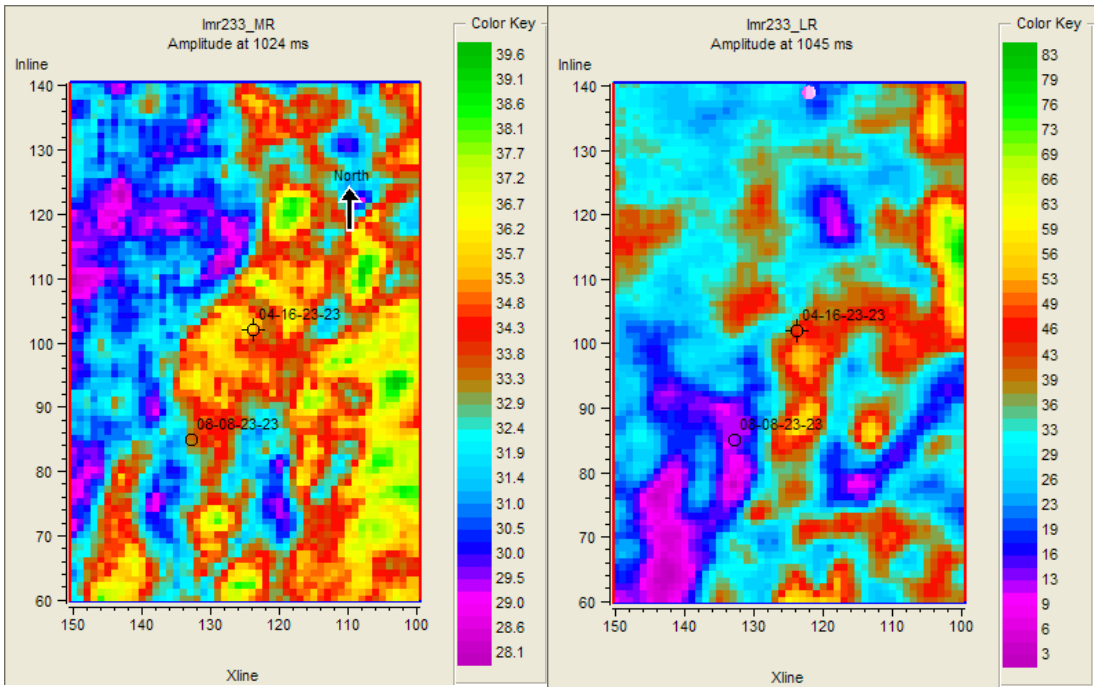

Figure 6.17 Time slices of skeleton term (ρs) for the upper valley (left) and lower valley (right) with well locations.

The crossplot of the fluid term (ρf) and skeleton term (ρs) will enhance the interpretation of the lithology and fluid content by setting up the cut-off values for the high skeleton term (ρs) and low fluid term (ρf) (Figure 6.18).

To investigate the effect of the c value on the fluid term, different c values were applied to extract the fluid terms. Figure 6.19 to figure 6.22 show the fluid term time slices using c equal to 1.0, 2.0, 2.233, and 3.0. The fluid term using c=1.0 is equivalent to the attribute of $Ip^2 - Is^2$ which is often used as a fluid indicator. When c=2.0 is used, the fluid term is equal to Lambda-Rho ($\lambda\rho$), which corresponds to the LMR (lambda-mu-rho) method. A c value of 2.233 corresponds to porous clean sandstones and the value of c=3.0 is for the shale case which consider the shale as background.

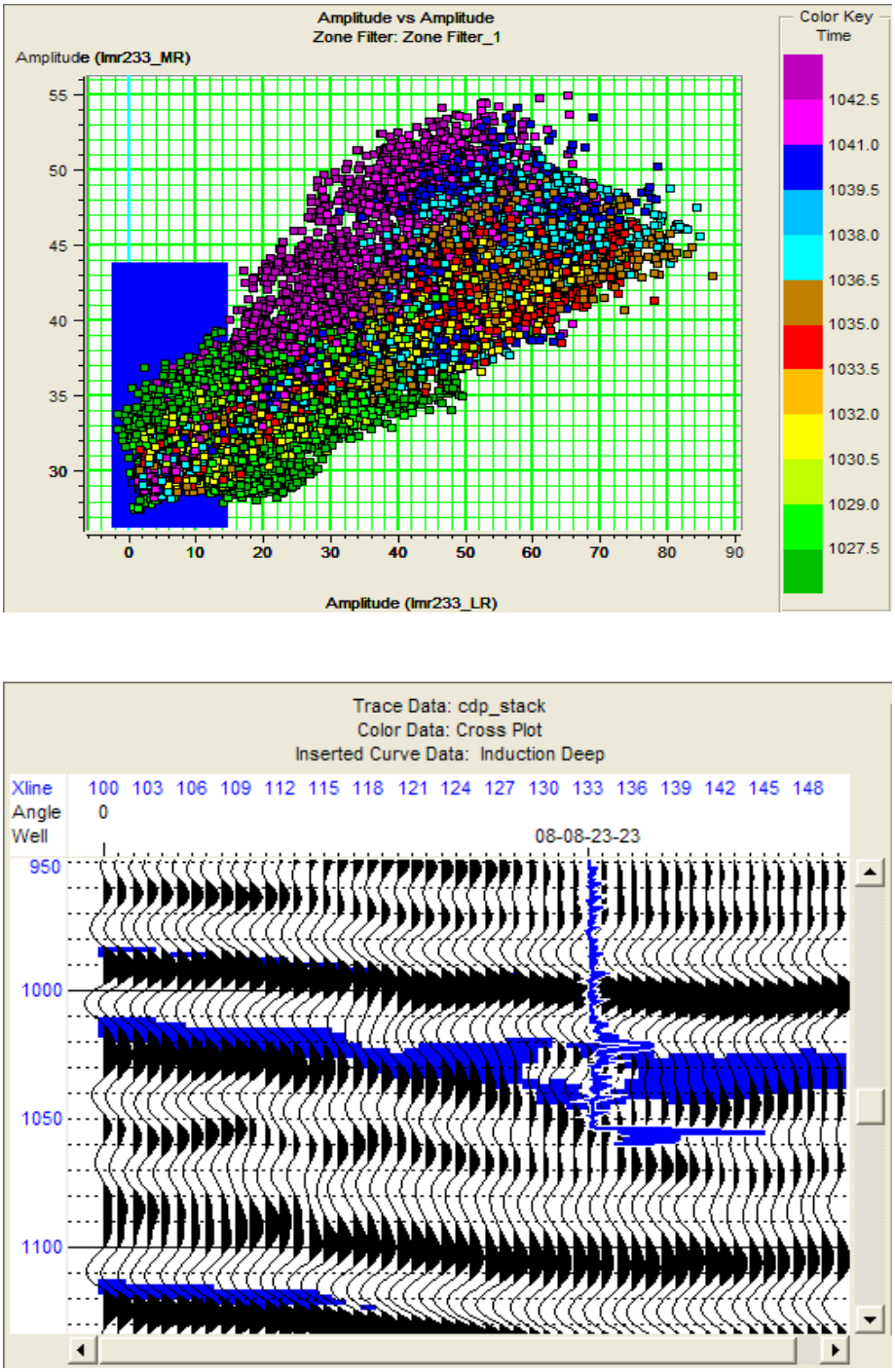

Figure 6.18 The crossplot (above) of the fluid term (ρf) versus the skeleton term (ρs) for the upper valley. Polygon in blue means the low fluid term. The blue color on the seismic cross section (bottom) is correspondent with the blue rectangle in the crossplot.

From the time slices of the fluid term for the upper valley and lower valleys, it is noticed that the trends corresponding to the upper and lower valleys are similar, but they show much more difference inside the channel system. For the time slice from the fluid term (ρf , c =1.0), the trend for the upper incised valleys is clearly demonstrated. However, it provides the poor resolution for the interpretation of the upper valley. Time slices of the fluid terms using c =2.0, 2.233, and 3.0 greatly improve the interpretive resolution and give much more information on the hydrocarbon inside the upper valley system. Time slices of the lower valleys, using the fluid terms, show not much difference, which means the inversion result for the lower valley is not sensitive to the c value selection.

The interesting thing is that although c =3.0 is not a proper value for the fluid term extraction, it provides the better interpretive result. This can be explained by the fact that the fluid term based on the band-limited seismic may have some bias during the inversion process, which makes the extracted fluid term insensitive to the c value.

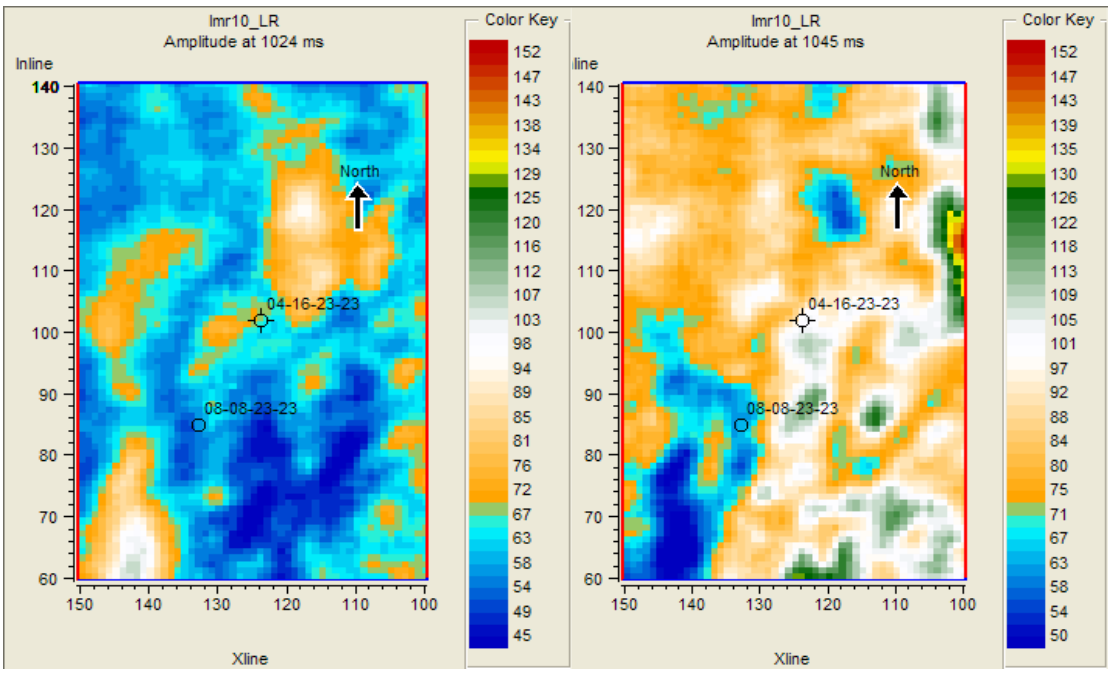

Figure 6.19 Time slices of fluid term (ρf , c =1.0) for the upper valley (left) and lower valley (right) with well locations.

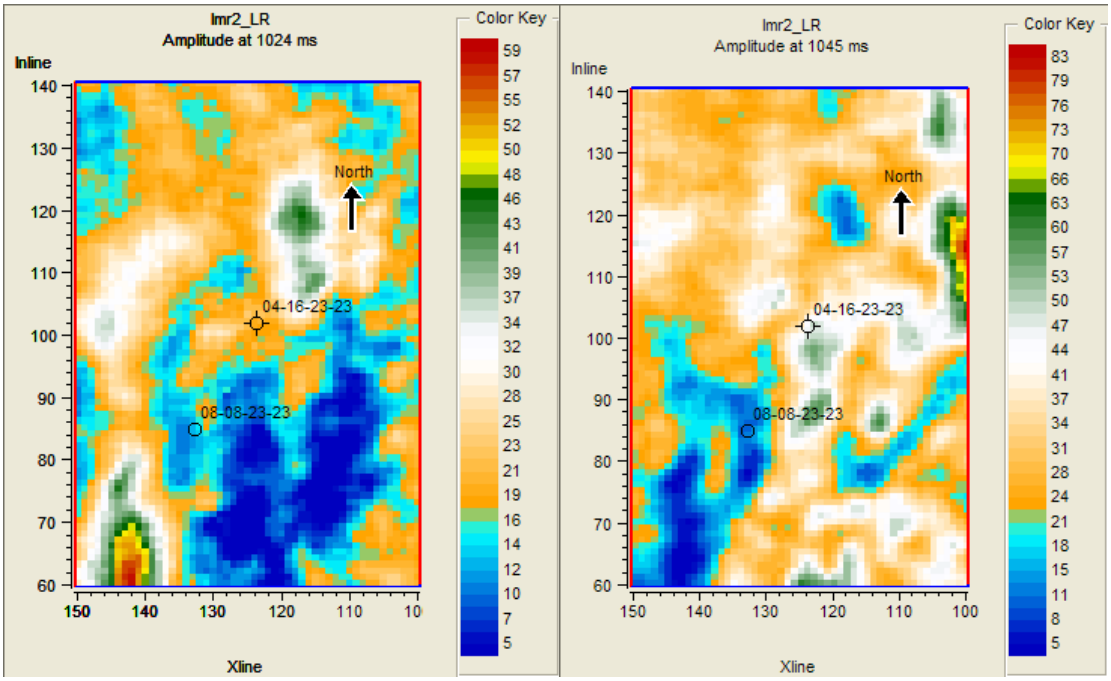

Figure 6.20 Time slices of fluid term (ρf , c =2.0) for the upper valley (left) and lower valley (right) with well locations.

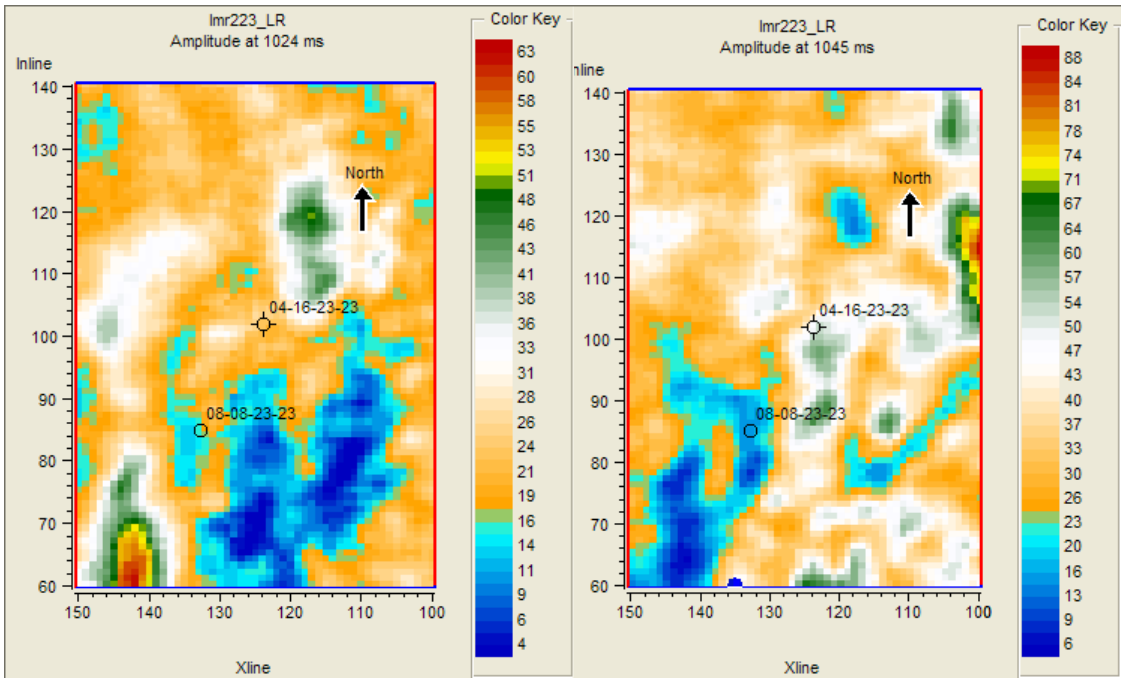

Figure 6.21 Time slices of fluid term (ρf , c =2.233) for the upper valley (left) and lower valley (right) with well locations.

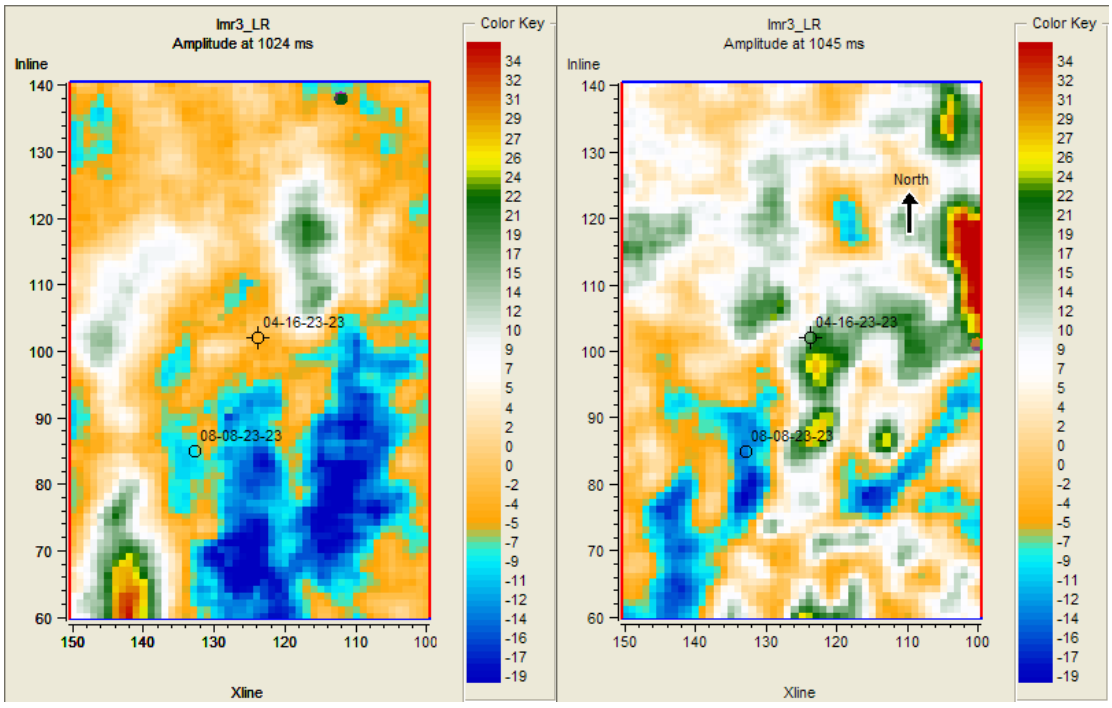

Figure 6.22 Time slices of fluid term (ρf , c =3.0) for the upper valley (left) and lower valley (right) with well locations.

6.7 Conclusions

Although the generalized fluid method provides a flexible way to derive the fluid term to identify the presence of the hydrocarbon in the reservoir, the selection of the c value is a challenge. When core samples are available, it is easy to estimate the c value for the specific reservoir. The c value can also be estimated using the full dipole sonic logs and density log using the Gassmann fluid substitution. Because there are assumptions on the components of the mineral in the rock, fluid constitution, the estimated c value is not always reliable using the Gassmann approach.

Similar discrimination can be observed in $Ip^2 - c * Is^2$, $K - \mu$, $\lambda\rho$ based on the analysis of the well logs and seismic data. Well log analysis shows that the fluid term $Ip^2 - c * Is^2$ may be the most sensitive to the hydrocarbon although there is often not much difference in the term when extracted from noisy seismic data.

The inversion results of the fluid term $Ip^2 - c * Is^2$ can greatly improve our ability to image and interpret porous sandstone and hydrocarbon distribution in the Glauconitic incised valley as long as a proper c value is provided.

CHAPTER SEVEN: CONCLUSIONS AND FUTURE WORK

7.1 Conclusions

In this study various dataset, including laboratory measurements, numerical examples, well logs, and real seismic data, were investigated using the generalized fluid method. It can be concluded that:

1. The laboratory measured data show that the value of $(Vp/Vs)_{dry}$ ratio will be affected by the clay content, porosity, and differential pressure. The value of $(Vp/Vs)_{dry}$ ratio for dry sandstones increases with porosity and decreases with clay content. For dry shaly sandstones, $(Vp/Vs)_{dry}$ ratio increases with increasing differential pressure. However, for clean sandstones, $(Vp/Vs)_{dry}$ ratio remains constant with different differential pressures. The average value of $(Vp/Vs)_{dry}$ ratio s is around 1.52 for dry clean sandstones and 1.55 for dry shaly sandstones. The corresponding c values in the generalized fluid method are 2.31 and 2.40, respectively.

2. To some extent, the fluid indicators: $Ip^2 - c * Is^2$, $K - \mu$, $\lambda\rho$, K , λ, λ/μ, and σ exhibit the same discrimination capability for dry and wet sandstones. The difference among them is that $Ip^2 - c * Is^2$ and $K - \mu$ are sensitive to the pore fluid alone whereas other fluid indicators are sensitive to the pore fluid and rock skeleton combined.

3. Porosity, differential pressure, and clay content will affect all the fluid indicators' discrimination ability between wet and dry sandstones. Laboratory measured data shows that high porosity will make the discrimination between wet and dry sandstones easier. The presence of clay makes it easy to discriminate the fluid content. With increase of

pressure, the sensitivity of the fluid terms to the fluid content is reduced, which implies that the detection of fluid content will be more difficult with increasing compaction and cementation.

4. The c value plays an important role in the generalized fluid method: $Ip^2 - c * Is^2$. It is important to estimate a proper value for c to make the attribute $Ip^2 - c * Is^2$ more diagnostic than other attributes. The generalized fluid method provides a flexible approach to observe the anomalies associated with the fluid content. Usually, core data and well logs from the studied area will help determine the optimal c value.

5. The Blackfoot seismic data demonstrated that the generalized fluid method can significantly improve our ability to identify the presence of hydrocarbons in Glauconitic incised valleys. The result of the fluid term is encouraging because it has proven to be a more sensitive discriminator of pore-fluid content than other methods.

7.2 Future work

It is clear that the generalized fluid method $Ip^2 - c * Is^2$ can provide a more intuitive way to interpret the presence of the hydrocarbons. Different c values provide different fluid attributes to identify hydrocarbons. However, it is a challenge to derive the appropriate c value for specific reservoirs. In this study, the effect of porosity, clay content, and pressure on the c value was investigated for clastic reservoirs based on the Han's laboratory measurements. More research work is needed to be done to study c value change for different type of reservoirs.

REFERENCES

Aki, K., and Richards, P.G., 1980, Quantitative seismology: Theory and methods: W. H. Freeman and Co.

Allen, J.L., and Peddy, C.P., 1993, Amplitude variation with offset Gulf coast case studies: Society of Exploration Geophysicists, Tulsa, OK., 120 pp.

Batzle, M.L., Hafmann, R., Han, D.H., and Castangna, J.P., 2001, Fluids and frequency dependent seismic velocities of rocks: The Leading Edge, February, 168-171.

Batzle,M.L., Han, D.H., and Hofmann, R., 2001, Optimal hydrocarbon indicators: SEG Expanded Abstracts, Vol. 20 (2001), p.1697.

Biot, M.A., 1941, General theory of three-dimensional consolidation: Journal of Applied Physics, **12**,155-164.

Bortfeld, R., 1961, Approximation to the reflection and transmission coefficients of plane longitudinal and transverse waves: Geophys. Prosp., **9**, 485-503.

Broger, K.E.J., Syhlonyk, G.E., and Zaitlin, B.A., 1997, Glauconite sandstone exploration: A case study from the Lake Newell project, southern Alberta: Can. Soc. Petr. Geol. Mem. **18**, 140–168.

Castagna, J. P., Batzle, M. L., and Eastwood, R. L., 1985, Relationship between compressionaland shear-wave velocities in clastic silicate rocks: Geophysics, **50**, 571-581.

Castagna, J.P., and Backus, M.M., 1993, AVO analysis-tutorial and review in Castagna, J. and Backus, M.M., eds, Offset-dependent reflectivity. Theory and practice of AVO analysis: Soc. Expl. Geophys., 3-37.

Castagna, J.P., and Smith, W.S., 1994, Comparison of AVO indicators: A modeling study:Geophysics, 59, 1849-1855.

Castagna, J.P., and Swan, H.W., 1998, Principles of AVO crossplotting: The Leading Edge, **16**, 337-342.

Castagna, J.P., Swan, H.W., and Foster, D.J., 1998, Framework for AVO gradient and intercept interpretation: Geophysics, **63**, 948-956.

Castagna, J.P., Batzle, M.L., and Eastwood, R.L., 1985, Relationships between compressional-wave and shear-wave velocities in clastic silicate rocks: Geophysics, **50**, 571-581.

Connolly, P., 1999, Elastic Impedance: The Leading Edge, April, 438-452.

Dillon, L., Schwedersky, G., Vasquez, G., Velloso, R., and Nunes, C., 2003, A multiscale DHI elastic attributes evaluation: The Leading Edge, **22**, no. 10, 1024-1029.

Dufour, J., Squires, J., Goodway, W., Edmunds, A., and Shook, I., 1999, Integrated geological and geophysical interpretation and Lame rock parameter extractions using AVO analysis on the Blackfoot 3C-3D seismic data, Southern Alberta: Geophysics, **67**, 27-37.

Fatti, J. L., Vail, P. J., Smith, G. C., Strauss, P. J., and Levitt, P. R., 1994, Detection of gas in sandstone reservoirs using AVO analysis: A 3-D seismic case history using the geostack technique: Geophysics, **59**, 1362-1376.

Gassmann, F., 1951, Uber die Elastizitat poroser Medien, Vierteljahrsschrift der Naturforschenden Gesellschaft in Zurich, **96**, 1-23.

Goodway, W., 2001, AVO and Lamé constants for rock parameterization and fluid detection. Recorder, **26**, 39-60.

Goodway, W., Chen, T., and Downton, J., 1997, Improved AVO fluid detection and lithology discrimination using Lamé petrophysical Parameters; “Lambda-Rho”, “Mu-Rho”, & “Lambda/Mu fluid stack”, from P and S inversions.

Gray, D., Goodway, W., and Chen, T., 1999, Bridging the gap: Using AVO to detect changes in fundamental elastic constants: 1999 SEG meeting abstracts, 852-855.

Han, D.H., and Batzle, M., 2002, Constrained and simplified Gassmann's equations: 72nd Annual International Meeting, SEG, Expanded Abstracts, 1837– 1841.

Han, D.H., and Batzle, M., 2003, Gassmann’s equation and fluid-saturation effects on seismic velocities: Geophysics **69**, p.398.

Han, D.H., Nur, A., and Morgan, S., 1986, Effects of porosity and clay content on wave velocities in sandstones: Geophysics, **51**, 2093-2107.

Hedlin, K., 2000, Pore space modulus and extraction using AVO: 70th Ann. Internat. Mtg., Soc. Expl. Geophys., Expanded Abstracts, 170-173.

Hedlin, K., 2000, Pore space Modulus and extraction using AVO: Extended Abstracts, Soc. Expl. Geophys., 70th Annual Meeting, Calgary.

Hill, R., 1952, The elastic behavior of a crystalline aggregate: Proc. Phys. Soc. London Ser. A, **65**, 349-354.

Hill, R., 1965, A self-consistent mechanics of composite materials: J. Mech. Phys. Solids, **13**, 213–222.

Hilterman, F.J., 1987, Seismic lithology: Unpublished course notes: Soc. Expl. Geophys.

Hilterman, F.J., 1989, Is AVO the seismic signature of rock properties? Expanded Abstracts, SEG, 59th Annual Meeting.

Hilterman, F., and Verm, R., 1995, Lithology color-coded seismic sections: The calibration of AVO cross-plotting to rock properties, The Leading Edge, **14**, 847-853.

Hilterman, F.J., 2001, Seismic Amplitude Interpretation: 2001 Distinguished Instructor Short Course, Distinguished Instructor Series, No. 4, Soc. Expl. Geophys..

Knott, C.G., 1899, Reflexion and refraction of elastic waves with seismological applications: Phil. Mag., **48**, 64-97.

Koefoed, O., 1955, On the effect of Poisson's ratios of rock strata on the reflection coefficients of plane waves: Geophys. Prosp., **3**, 381-387.

Krief, M., Garat, J., Stellingwerff, J. and Ventre, J., 1990, A petrophysical interpretation using the velocities of P and S waves: The Log Analyst, Nov-Dec, 355-369.

Kumar, D., 2006, A Tutorial on Gassmann Fluid Substitution: Formulation, Algorithm and Matlab Code: GEOHORIZONS, January, 2006

Larsen, J.A., Margrave, G.F., and Lu, H., 1999, AVO analysis by simultaneous P-P and P-S weighted stacking applied to 3C-3D seismic data: 69th Ann. Internat. Mtg., Soc. Expl. Geophys., Expanded Abstracts, 721-723.

Layer, D.B., and Members of Staff, Imperial Oil Ltd., 1949, Leduc oil field, Alberta, a Devonian coral reef discovery: Bulletin of the American Association of Petroleum Geologists, **33**, 575-602.

Lu, H., and Margrave, G., 1998, Reprocessing the Blackfoot 3C-3D seismic data: The CREWES Project Research Report, Vol. **10**.

Margrave, G.F., and Stewart R.R, 2001, Joint P-P and P-S seismic inversion, CREWES Research Report, Vol. **13.**

Margrave, G.F., Lawton, D.C., and Stewart, R.R., 1998, Interpreting channel sands with 3C-3D seismic data: The Leading Edge, **17**, 509–513.

Mavko, G. and Mukerji, T., 1998, Comparison of the Krief and critical porosity models for prediction of porosity and Vp/Vs: Geophysics **63**, 925-927.

Mavko, G., Mukerji, T., and Dvorkin, J., 1998, The rock physics handbook – Tools for seismic analysis in porous media: Cambridge University Press.

Miller, S., 1996, Multicomponent seismic data interpretation: M.Sc. thesis, University of Calgary.

Minear, J.W., 1982, Clay models and acoustic velocities: Soc. Petr. Eng. of AIME 57th Annual Tech. Conf. & Exhib.

Murphy, W., Reischer, A., and Hsu, K., 1992. Taking advantage of Shear waves: Oilfield Review.

Murphy, W., Reischer, A., and Hsu, K., 1993. Modulus Decomposition of Compressional and Shear Velocities in Sand Bodies: Geophysics **58**, 227-239.

Nur, A.M., 1969, Effect of stress and fluid inclusions on wave propagation in rock, Ph.D. Thesis, MIT.

Ostrander, W.J., 1982, Plane-wave reflection coefficients for gas sands at nonnormal angles of incidence: Geophysics, **49**, 1637-1648.

Richards, P.G., and Frasier, C.W., 1976, Scattering of elastic waves from depth-dependent inhomogeneties: Geophysics, **41**, 441-458.

Rojas, M., 2005, Elastic rock properties of tight gas sandstones for reservoir characterization at Rulison field, Colorado: MS thesis, Colorado School of Mines.

Rojas, M., Han, D.H., and Cobos, C., 2006, Constraining C for fluid properties inversion: SEG/New Orleans 2006 Annual Meeting

Russell, B.H., and Hampson, D., 1991, Comparison of poststack seismic inversions inversion methods: 61th Ann. Internat. Mtg., Soc. Expl. Geophys., Expanded Abstracts, 876–878.

Russell, B.H., Gray. D., Hampson D.P., and Lines, L.R., 2006, Linearized AVO and poroelasticity: CREWES Research Report, Volume 18 (2006)

Russell, B.H., Hedlin, K., Hilterman, F.J., and Lines, L.R., 2001, Fluid-property discrimination with AVO: A Biot-Gassmann Perspective: CREWES Research Report, Volume 13 (2001)

Russell, B.H., Hedlin, K., Hilterman, F.J., and Lines, L.R., 2003, Fluid-property discrimination with AVO: A Biot-Gassmann perspective: Geophysics, **68**, 29-39.

Rutherford, S. R., 1993, Noise discriminating, statistical-amplitude compensation for AVO analysis: Geophysics, **58**, 1831-1839

Rutherford, S.R., and Williams, R.H., 1989, Amplitude versus-offset variations in gas sands: Geophysics, **54**, 680688.

Sheriff, R.E., and Geldart, L.P., 1995, Exploration Seismology, Cambridge University Press, New York, NY

Sheriff, R.E., 1991, Encyclopedic Dictionary of Exploration: Geophysics, Third Ed., SEG.

Shuey, R.T., 1985, A simplification of the Zoeppritz equations: Geophysics, **50**, 609-614.

Simmons, J.L. and Backus, M.M., 1996, Waveform-based AVO inversion and AVO prediction-error: Geophysics, **61**, 1575-1588.

Smith, G.C., and Gidlow, P.M., 1987, Weighted stacking for rock property estimation and detection of gas: Geophys. Prosp., 35, 993-1014.

Stewart, R.R., 1990, Joint P and P-SV inversion: CREWES Research Report, Vol. 2, 1990.

Stewart, R.R., Zhang, Q., and Guthoff, F., 1995, Relationships among elastic-wave values (Rpp, Rps, Rss, Vp, Vs, ρ, σ, κ) CREWES Research Report Vol. 7.

Swan, H. W., 1993, Properties of direct AVO hydrocarbon indicators in Castagna, J. P., and Backus, M. M., Eds., Offset dependent reflectivity--Theory and practice of AVO analysis: Society of Exploration Geophysics, 78-92.

Tatham R.H., McCormack, M.D., 1991. Multicomponent seismology in petroleum exploration: Investigation in Geophysics Series Volume 6, SEG.

Toksoz, M.N., Cheng, C.H., and Timur, A., 1976, Velocities of seismic waves in porous rocks, Geophysics, **41**, 621-645.

Tosaya, C.A., Nur, A.M., and Daprat, G., 1984, Monitoring of thermal EOR fronts by seismic methods: Proceedings, 1984.

Vanorio, T., and Mavko, 2006, Vp/Vs ratio in gas-pressured saturated sandstones, G.SEG Expanded Abstracts **25**, 1545

Wang, Z., 2001, Fundamentals of seismic rock physics: Geophysics, **66**, 398–412.

Wang, Z., Cates, M.E., and Langan, R.T., 1997, Seismic monitoring of a CO2 flood in a carbonate reservoir: A rock physics study: Geophysics, **63**, 1604– 1617.

Wiggins, R. Kenny, G.S., and McClure, C.D., 1983, A method for determining and displaying the shear velocity reflectivities of a geologic formation: European patent Application 0113944.

Yilmaz, O., 2001, Seismic data analysis: Society of Exploration Geophysicists.

Zaitlin, B., Dalrymple, R.W., Boyd, R., Leckie, D., and MacEachern, J., 1995, The sratigraphic organization of incised valley systems: Implications to hydrocarbon exploration and production: Can. Soc. Petr. Geol. Short Course.

Zhu, X., and McMechan, G. A., 1990, Direct estimation of the bulk modulus of the frame in fluid saturated elastic medium by Biot theory: 60th Ann. Internat. Mtg., Soc. Expl. Geophys., Expanded Abstract, 787-790.

Zoeppritz, K., 1919, Erdbebenwellen VIIIB, On the reflection and propagation of seismic waves: Göttinger Nachrichten, I, 66-84.